Enhanced Depth Imaging OCT and OCT Angiography for Quantifying Optic Disc Drusen and Related Complications

Lindberg, Anne-Sofie Wessel

Publication date:
2020

Document Version
Publisher's PDF, also known as Version of record

PhD Thesis

DTU Compute
Department of Applied Mathematics and Computer Science

Enhanced Depth Imaging OCT and OCT Angiography for Quantifying Optic Disc Drusen and Related Complications

Anne-Sofie Wessel Lindberg

Kongens Lyngby 2020

DTU

DTU Compute
Department of Applied Mathematics and Computer Science
Technical University of Denmark

Richard Petersens Plads
Building 324
2800 Kongens Lyngby, Denmark
www.compute.dtu.dk

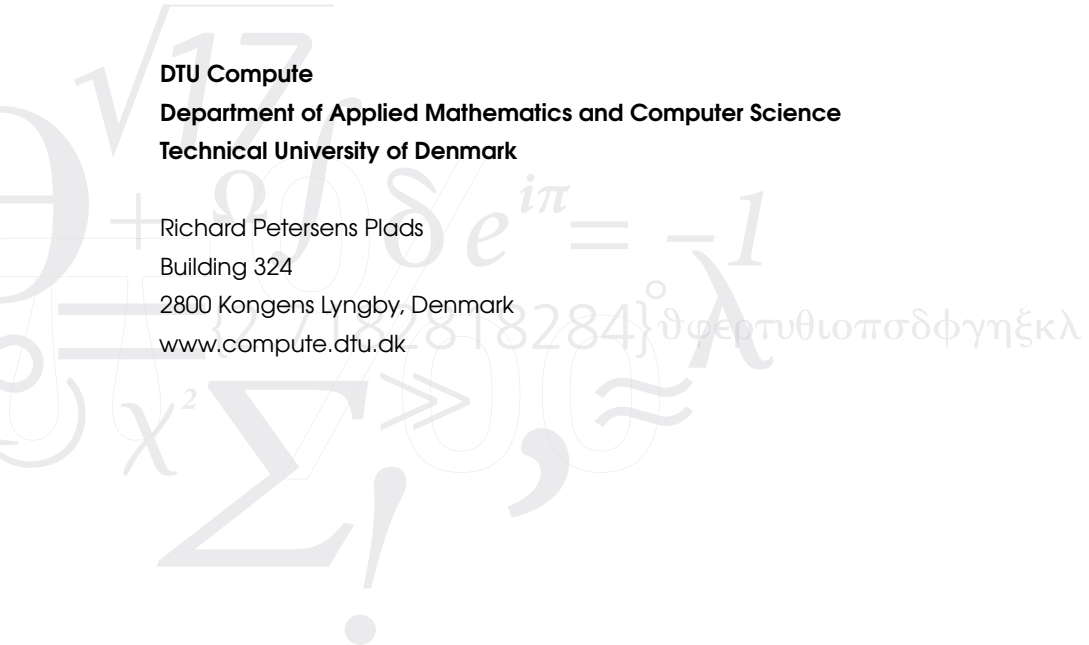

Summary (English)

Enhanced Depth Imaging Optical Coherence Tomography (EDI-OCT) is a modification of Spectral Domain Optical Coherence Tomography (SD-OCT). EDI-OCT enables imaging of deep located structures more clearly than standard SD-OCT.

In this thesis, we investigate the use of EDI-OCT for 3D quantification of spherical calcified objects in the optic nerve head known as the disease Optic Disc Drusen (ODD). With the use of image analysis, we quantify the ODD volume and anatomical location.

Next, we investigate how to optimize the visual appearance of anatomical structures such as ODD in EDI-OCT. We address the problem of combining two orthogonal EDI-OCT to improve the en face view of the EDI-OCT scan volume. The combination of two orthogonal scans is solved as an interpolation problem of interpolation from grid lines. We suggest three interpolation methods for solving the problem and we evaluate the performance of each method. We apply the best interpolation method to EDI-OCT data and evaluate the optimized appearance of anatomic structures and reduction of artefacts.

At last, we investigate how the 3D quantification of ODD can be used for investigations of ODD complications. We use the new technique OCT Angiography (OCTA), which enables to image the retinal blood flow. We develop a method for quantifying the local vessel density in specific areas around the optic nerve head. We apply the method to EDI-OCT scans of ODD patients and healthy subjects in order to investigate the impact of ODD volume and location on the local vessel density.

Summary (Danish)

Optisk kohærens tomografi med forbedret dybde afbildning (Enhanced Depth Imaging Optical Coherence Tomography, forkortet EDI-OCT) er en modificering af teknikken spektral domæne optisk kohærens tomografi (Spectral Domain Optical Coherence Tomography, forkortet SD-OCT). EDI-OCT muliggør en bedre afbildning af dybtliggende strukturer sammenlignet med SD-OCT.

I denne afhandling undersøger vi brugen af EDI-OCT til 3D kvantificering af kalcificerede kugleformede objekter i synsnervehovedet, bedre kendt som papil druser (Optic Disc Drusen, forkortet ODD). Ved brug af billedanalyse forsøger vi at kvantificere drusernes volumen og anatomiske placering i synsnervehovedet.

Vi undersøger om visualiseringen af druser i EDI-OCT billeder kan optimeres ved at kombinere to vinkelrette EDI-OCT skanninger. Målet med at kombinere de to vinkelrette skanninger er, at forbedre kvaliteten af en face billeder fra EDI-OCT volumenet. Kombinationen af de to vinkelrette skanninger løses som et interpolation problem, hvor der interpoleres ved brug af informationen langs de vinkelrette skanningslinjerne. Vi afprøver tre forskellige interpolationsmetoder til løsning af problemet og evaluere præstationen af hver metode. Efterfølgende anvender vi den bedste metode på EDI-OCT data og undersøger om anatomiske strukturers udseende er forbedret og om artefakter er reduceret i forskellige en face billeder.

Til sidst undersøger vi om kendskabet til ODD volumen og deres anatomiske placering kan anvendes til at undersøge af de komplikationer som ODD forårsager. Vi gør brug af den nye teknik optisk kohærens tomografi angiografi (OCTA), som muliggør afbildning af det retinale blod flow. Vi udvikler en metode til at kvantificere den lokale kardensitet i specifikke lokalområder omkring synsnervehovedet. Metoden anvendes på OCTA skanninger af ODD patienter og raske kontroller. Resultaterne heraf viser hvordan ODD volumenet samt deres anatomiske placering påvirker den lokale kardensitet.

Preface

This thesis was prepared at the department of Applied Mathematics and Computer Science at the Technical University of Denmark (DTU Compute) in fulfillment of the requirements for acquiring a *doctor of philosophy degree* (PhD) within medical image analysis.

The PhD project presented in this thesis was financed by DTU Compute and Rigshospitalet, Glostrup.

The aim of the project was to use image analysis for addressing research areas in ophthalmology. Image analysis was used for quantification of the disease optic disc drusen imaged with Optical Coherence Tomography (OCT) and OCT Angiography (OCTA).

The research presented in this thesis was conducted in close collaboration with medical doctor and PhD Lasse Malmqvist, medical doctor Lea Lybek Rueløkke and medical doctor Isabelle Karlesand from the Department of Ophthalmology at Rigshospitalet, Glostrup. The research was conducted from December 2014 to September 2020 including two maternity leaves.

The project was supervised by Associate Professor Vedrana Andersen Dahl from DTU Compute and Associate Professor of Ophthalmology Steffen Hamann from Department of Ophthalmology, Rigshospitalet, Glostrup. Furthermore, co-supervised by Researcher Thomas Martini Jørgensen from DTU Compute.

Kongens Lyngby, September 15, 2020

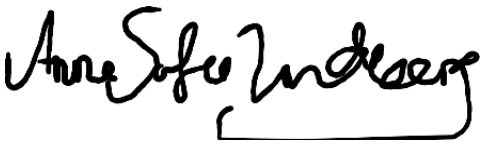

Anne-Sofie Wessel Lindberg

Acknowledgements

First of all, I would like to thank my main supervisor Vedrana Andersen Dahl. Thanks for always being supportive, motivating and a perfectionist when editing my written work. Thanks to my co-supervisor Steffen Hamann for involving me in interesting clinical projects, motivating me and for believing in my abilities. Thanks to my co-supervisor Thomas Martini Jørgensen.

A special thanks to one of my collaborators at Rigshospitalet Glostrup, Lasse Malmqvist. Thanks for always giving constructive feed back, coming up with great ideas for new and interesting projects and for being easy to talk with and helpful. Thanks to my other collaborators at Rigshospitalet Glostrup; Lea Lybek Rueløkke, Frederik Loft, Julie Vahlgren, Isabelle Karlesand, Mathias Heiberg and Tara Radaa.

Thanks to all my former and current colleagues at the Image Analysis and Computer Graphics section at DTU Compute.

Last, but not least I would like to thank my family and friends. A special thanks to my boyfriend Simon for being supportive and understanding. Thanks for motivating me and for travelling along to conferences around the world, making it possible to bring our kids, Josephine and Villum.

Contributions

List of papers and other contributions produced during the PhD study.

Journal papers included in this thesis and can be found as appendix

- **Paper A**

  Lasse Malmqvist, Anne-Sofie Wessel Lindberg, Vedrana Andersen Dahl, Thomas Martini Jørgensen and Steffen Hamann. Quantitatively Measured Anatomic Location and Volume of Optic Disc Drusen: An Enhanced Depth Imaging Optical Coherence Tomography Study. *Investigative Ophthalmology & Visual Science*. 58, 5, p. 2491-2497, 2017.

- **Paper B**

  Anne-Sofie Wessel Lindberg, Thomas Martini Jørgensen and Vedrana Andersen Dahl. Linear, Transfinite and Weighted Method for Interpolation from Grid Lines Applied to OCT Images. *Applied Soft Computing*. 68, p. 293-302, 2018.

- **Paper C**

  Anne-Sofie Wessel Lindberg, Vedrana Andersen Dahl, Isabelle Karlesand, Lea Lybek Rueløkke, Lasse Malmqvist and Steffen Hamann. Determination of peripapillary vessel density and the influence of optic disc drusen from EDI-OCT and OCT angiography. *Experimental Eye Research*. Vol 197, August 2020.

Peer-reviewed paper not included in this thesis

- **Paper was later extended into paper B and therefore relevant but not added as appendix**

  Anne-Sofie Wessel Lindberg, Thomas Martini Jørgensen and Vedrana Andersen Dahl. Interpolation from Grid Lines: Linear, Transfinite and Weighted Method. *Image Analysis. Springer*, p. 338–349 (Lecture Notes in Computer Science, Vol. 10270), 2017.

Journal papers not included in this thesis

- Anne-Sofie Wessel Lindberg, Knut Conradsen and Rasmus Larsen. Quantitative tumor heterogeneity assessment on a nuclear population basis. *Cytometry, part A*. 91, 6. p. 574-584, 2016.

- Frederik Cornelius Loft, Lasse Malmqvist, Anne-Sofie Wessel Lindberg and Steffen Hamann. The Influence of Volume and Anatomic Location of Optic Disc Drusen on the Sensitivity of Autofluorescence. *Journal of Neuro-Ophthalmology*. 39, 1, p. 23-27, 2018. **My contributions: Data processing, teach segmentation and calculation of anatomic location of ODD and volume**

- Julie Vahlgren, Lasse Malmqvist, Lea Rueløkke, Anna Karlesand, Anne-Sofie Wessel Lindberg, and Steffen Hamann. The angioarchitecture of the optic nerve head in patients with optic disc drusen. *Investigative Ophthalmology & Visual Science*. 44, 1, p. 1-6, 2019. **My contribution: Data processing.**

- Mathias Heiberg, Lea Lybek Rueløkke, Isabelle Karlesand, Anne-Sofie Wessel Lindberg, Lasse Malmqvist and Steffen Hamann. Clinical paper on peripapillary vessel density for ODD patients. *In progress for submission*. **My contributions: Teach segmentation, calculation of ODD volume and location, registration between OCT and OCT and calculation of vessel densities using the method developed in paper C.**

- Tara Therese Radaa, Anne-Sofie Wessel Lindberg and Steffen Hamann. Optic nerve head drusen in children. An OCT-based analysis of the anatomical basis for the terms optic disc edema and pseudopapilledema. *In progress for submission*. **My contributions: Calculation of vessel densities using the method developed in paper C.**

Conference abstracts, presentations and other publications

- Anne-Sofie Wessel Lindberg, Lasse Malmqvist, Vedrana Andersen Dahl, Thomas Martini Jørgensen and Steffen Hamann. Quantitative Measure of Optic Disc Drusen Location in Enhanced Depth Imaging Optical Coherence Tomography (EDI-OCT) Scans. Abstract and poster presented at annual meeting for *The Association for Research in Vision and Ophthalmology (ARVO)*, 2017.

- Anne-Sofie Wessel Lindberg, Vedrana Andersen Dahl, Lasse Malmqvist and Steffen Hamann. Development of a computational method for comparison of information from EDI-OCT and OCTA scans. Abstract and oral presentation given at conference *International Swept Source OCT (ISSOCT)*, 2018.

- Isabelle Karlesand, Anne-Sofie Lindberg, Lea Lybek Rueløkke, Lasse Malmqvist and Steffen Hamann. Multiplexed optical coherence tomography imaging of optic disc drusen. Picture case published in *Indian Journal of Ophthalmology*. August 2020.

Abbreviations

2D	Two dimensional
3D	Three dimensional
AMD	Age-related Macula Degeneration
BM	Bruchs Membrane
EDI-OCT	Enhanced Depth Imaging Optic Coherence Tomography
ILM	Inner Limiting Membrane
NAION	Nonarteritic Anterior Ischemic Optic Neuropathy
OCT	Optic Coherence Tomography
OCTA	Optic Coherence Tomography Angiography
ODD	Optic Disc Drusen
ONH	Optic Nerve Head
PHOMS	Peripapillary Hyperreflective Ovoid Mass-like Structures
PSNR	Peak Signal to Noise Ratio
RMSE	Root Mean Square Error
RNFL	Retinal Nerve Fiber Layers
RPE	Retinal Pigment Epithelium
SD-OCT	Spectral Domain Optical Coherence Tomography
SLO	Scanning Laser Ophthalmoscope
SS-OCT	Swept Source Optical Coherence Tomography
TD-OCT	Time Domain Optical Coherence Tomography

Contents

CHAPTER 1

Introduction to the project

The vision is one of the five senses. It gives the ability to interpret the surrounding environment by detecting reflected light from objects and thereby see visible elements. Decrease or loss of the vision is often connected with a deterioration in life quality.

The eye is the sensory organ of the visual system, and many eye disorders affect the vision. Ophthalmology is a branc of medicine dealing with diagnosis, treatment and prevention of eye disorders. There exits a variety of eye examination techniques used in ophthalmology such as ultrasound, ophthalmoscope and **Optical Coherence Tomography (OCT)**.

This thesis deals with optical coherence tomography (OCT), a modality which has undergone a large development in the last three decades. OCT enables non-invasive imaging of the retina. Today, OCT is the most important tool in the investigation of eye diseases and their pathology. The technique is in constant development, with a speed of which has also influenced this PhD project.

Within the duration of this PhD project, a new OCT technique has become available. This technique, OCT Angiography (OCTA), enables imaging of blood flow in the retina. Images from the technique OCTA are used in the last contribution of this PhD project.

The following section describes the original ideas for the PhD project. Further, we sketch the chronology of the project. This is done in order to explain the connection between the research conducted in the project and its contributions.

1.1 The original project description

As part of the strategic framework agreement between Technical University of Denmark (DTU) and Rigshospitalet Glostrup, funding was provided for two PhD projects. This project received funding to support and strengthen an already existing collaboration between the Department of Applied Mathematics and Computer Science at DTU and the Department of Ophthalmology at Rigshospitalet, Glostrup.

The overall idea of the project was to use advanced image analysis methods to support research in ophthalmology. The plan was to develop methods for analysis of OCT scans in both 2D and 3D to support investigation of pathology of various ophthalmic diseases.

It was decided, that the project should focus on the deeper layers of retina and the optic nerve head and the intention was to get more insight to deep located structures. The reason for focusing on deep located structures was that these are challenging to analyse in standard OCT. Shadowing artefacts and the fact that the light intensity de-

creases exponentially with depth, combined with a low signal to noise ratio, complicated the visibility of deep located structures.

The availability of a new technique known as Enhanced Depth Imaging OCT (EDI-OCT) created the possibility to acquire OCT images with more visibility in depth. The main interest areas for the research group at the department of ophthalmology at Rigshospitalet Glostrup in respect to deep located structures were quantification of deformations of lamina cribrosa and the disease Optic Disc Drusen (ODD).

Another idea for project content was creation of a 3D model of optic nerve head. The 3D model should be build from OCT scans of healthy subjects and the model should be build with the use of statistical methods.

Another idea was monitoring of the vision for diabetic eyes also known as diabetic retinopathy. In the clinic, the eyes were imaged with fundoscopy imaging. Here, the aim was to investigate how OCT imaging could help get more information about the progression and status of the disease. Last idea for a project was quantification of blood flow using OCT imaging and its use for diagnosis of leukaemia.

1.2 Project process and decisions made

At the beginning of any project, investigations into which problems should be worked on, is largely dependent on availability of data. EDI-OCT was a new technique and therefore not included in the examinations at the hospital.

I started working on OCT images of a few healthy subjects to get to understand the modality, its possibilities and limitations. A regular OCT scan only contained around 30 B-scans scanned with a large distance between them. This type of scan is fine for analysis of individual B-scans, which is the normal procedure in the clinic. However, combining the individual B-scans into a volume for 3D analysis was not optimal. Furthermore, a need for EDI-OCT data to study the deep located structures existed.

EDI-OCT data was acquired by a medical doctor and PhD student Lasse Malmqvist. Lasse worked with ODD in his PhD project and together we planned an EDI-OCT scan protocol for a large clinical study with ODD patients. For me, it was important that the number of B-scans was set to maximum possible. We ended up with acquisition of 97 horizontal B-scans scanned as dense as possible. Furthermore, acquisition of an extra scan in the vertical scan direction was added to the protocol. The idea behind was to combine two orthogonal scans to obtain more information of deep located structures. Last, but important, thing in the scan protocol was the use of EDI mode.

Within a period of three months, Lasse did a great job scanning 40 ODD patients. Based on these data and within the first year of my PhD, we published the study presented in Paper A. My contribution was a method for measuring the ODD volume and anatomical location of ODD with the use of EDI-OCT scans. The method for measure the anatomical location of ODD was presented as a poster in 2017 at the annual meeting for the world's largest eye and vision research organization, the Association for Research in Vision and Ophthalmology (ARVO).

Next project became the combination of orthogonal EDI-OCT scans to improve visibility of anatomical structures. Before this could be carried out, an investigation of the best suitable interpolation method for solving the problem had to be performed. This study was published as a peer review paper and presented as a poster at the conference Scandinavian Conference of Image Analysis (SCIA) in 2017. The paper was chosen as one of the best written papers and an extended version of the paper was invited for submission to the journal Applied Soft Computing. The extended paper was published in the journal Applied Soft Computing and is contribution paper B. In paper B, we applied the interpolation methods to EDI-OCT scans and evaluated them in regard to minimization of artefacts and improved visibility of anatomical structures.

Meanwhile, the new technique OCTA had become available in the clinic at the department of ophthalmology, which motivated the project behind the last paper, paper C. Together with medical student Lea Rueløkke, I planned a large clinical study with the use of OCTA scans of ODD patients. We wanted to combine the ODD anatomical location and volume from the EDI-OCT scans, as described in paper A, with information about blood flow from OCTA. Over a long period of time, Lea recruited and acquired EDI-OCT and OCTA scans of more than 30 ODD patients. The first attempt to combine the information from the two modalities was presented as an oral presentation at the conference International Swept Source OCT (ISSOCT) in 2018.

The complete method of combining the two scan types and expression of the local vessel density was applied to a subset of the data acquired by Lea. The method and results are presented in paper C, which is published in the journal Experimental Eye Research.

Later on, the method for expressing local vessel density was applied to OCTA scans of children with ODD together with medical student Tara Radaa. The results from this study is planned to be presented in a journal paper and will soon be submitted to a suitable journal. Furthermore, the method has been applied to the entire data set acquired by Lea and to around 50 healthy subjects acquired by Isabelle Karlesand. The results of this large clinical study will be presented in a paper planned for submission in the near future.

1.3 Objectives

The main objective of this thesis was to investigate the applicability of image analysis methods for investigation of 3D structures in OCT scans related to ophthalmic diseases, primarily optic disc drusen.

1.4 Thesis overview

This thesis consists of three parts. The first part contains theory about the eye and the modalities OCT and OCTA. (chapter 2 and 3). This part gives some background

knowledge in order to understand the challenges and problems dealt with in the work behind the thesis. The second part of the thesis contains our research, description of methods, discussions, solutions and conclusion (chapter 4 and 5). Last part is appendices with our contributions in form of paper A, B and C in their published layout.

CHAPTER 2

The eye and optic disc drusen

This chapter contains background information about the ophthalmic disease that motivated the project. First, a description of the anatomy of the eye and the optic nerve head is given. Second, a description of the disease optic disc drusen and its pathogenesis is given.

2.1 Anatomy of the eye

The human eye is the organ of the visual system. Together with the optic pathways and the brain, the two eyes create the vision. Figure 2.1 illustrates the anatomy of the human eye and the location of the different major components.

The input light signal first hits the cornea, then enters through the pupil with the iris regulating the amount of light. It passes the lens and moves through the vitreous body and hits the retina. The retina is the inner layer of the eyeball and consists of an inner neural layer and an outer pigmented layer. The neural layer consists of three different types of neurons; photoreceptor cells, bipolar cells and ganglion cells which,

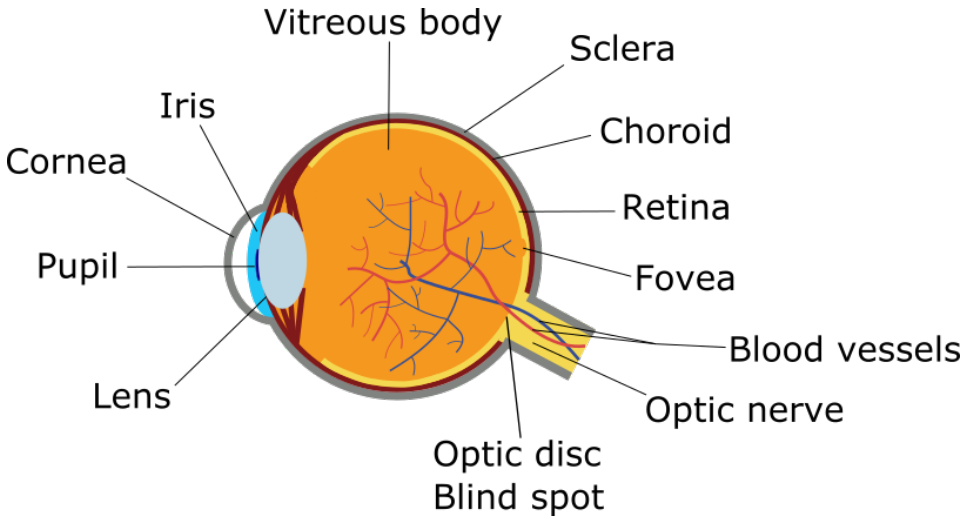

Figure 2.1: Illustration of anatomy of the eye.

together with other cells, form the ten different layers of the retina [1,2]. The ten layers of the retina are listed in Table 2.1.

Besides the ten retinal layers, a membrane named Bruch's membrane is located in the retina. Bruch's membrane is a multilayered structure located between the retinal pigment epithelium (RPE) and the choroid. It consists of five layers including the RPE base membrane. The choroid is located below the retinal layers and is the vascular layer of the eye.

Layer number	Name	Abbreviation
1	Inner Limiting Membrane	INL
2	Nerve Fiber Layer	NFL
3	Ganglion Cell Layer	GCL
4	Inner Plexiform Layer	IPL
5	Inner Nuclear Layer	INL
6	Outer Plexiform Layer	OPL
7	Outer Nuclear Layer	ONL
8	Outer Limiting Membrane	OLM
9	Photoreceptor Layer	PL
10	Retinal Pigment Epithelium	RPE

Table 2.1: The ten retinal layers and their abbreviation listed from inner to outer part of the retina.

2.1.1 Optic nerve head

The optic nerve head (ONH) or optic disc is located at the back of the eye and is the point where ganglion cells leave the eye. The optic disc has no photoreceptors and is therefore a blind spot in the visual field (Figure 2.1).

At a fundus photograph (fundoscopy) acquired with an ophthalmoscope, the optic disc and the optic cup can be seen. The optic disc is round or slightly oval in shape. The shape is the result of Bruch's membrane opening. On an OCT image of the ONH, the size of the optic disc can be measured from the termination of Bruch's membrane on opposing side. This is also called the scleral canal. Figure 2.2 shows the measurement of the scleral canal (red) and the optic cup (green) on an OCT image of the ONH for a healthy subject. The size of the scleral canal varies significantly between individuals [3]. This size is important in the investigation of diseases located in the optic nerve head.

In the retina, photoreceptor cells transmit the visual input to ganglion cells. Ganglion cells form the retinal nerve fiber layer (RNFL) and exit from the eye through the scleral canal. Ganglion cells are the retinal neurons. After passing through the scleral canal, their axons form the optic nerve. The optic nerve consists of bundles of axons incorporated in a myelin sheath. It transports the signal from the eye to the brain. This makes the optic nerve head the place for existing of the neural signal. Furthermore, the blood supply of the eye enters at the optic nerve head.

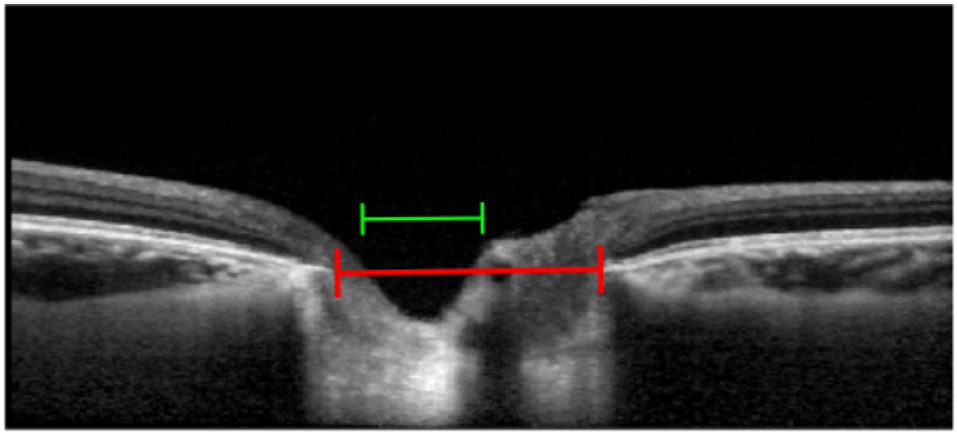

Figure 2.2: Measurement of the optic disc and the optic cup on an OCT image of the ONH (optic nerve head) for a healthy subject. The size of optic disc is the distance at the opening of Bruch's membrane marked with red. This is also known as the scleral canal. The diameter of optic cup is marked with green.

2.2 Optic Disc Drusen

Optic Disc Drusen (ODD) was first described in 1858 by Heinrich Müller [4]. The name drusen originates from the german word for geodes, which are spherical rock structures with internal cavities lined with quartz crystals. Drusen are acellular calcium concretions (compact mass) and occur in about 2% of the population [5, 6] and at all ages. Drusen are often asymptomatic, but visual field defects are seen in most cases [7,8]. The possibility of getting visual field defects caused by drusen increases with age [9–11] while visual acuity and color vision usually remain unaffected throughout life. There have been reported rare cases with severe visual field loss and even blindness due to ODD [12, 13]. Sudden vision loss associated with ODD is most commonly due to the disease nonarteritic anterior ischemic optic neuropathy (NAION) [14] .

ODD can be classified into two groups, visible and burried, based on their visibility on ophthalmoscopy. The visibility depends on the anatomical location of drusen within the ONH, on size of the drusen and the degree of calcification. Furthermore, it is seen that the visibility of the deeper layers is better due to thinning of the retinal nerve fiber layers (RNFL) in older patients. The size and number of ODD in a given ONH varies greatly. The general number of ODD is two to three per eye and they are most often present in both eyes (bilateral). ODD can occur as a solitary drusen or in a group of many smaller ODD known as conglomerates.

ODD almost always leads to elevation of the optic disc, but how much the optic disc is elevated depends on the number of ODD, their volume and how superficial they are located. Figure 2.3 shows an OCT image of ODD in the ONH, where the disc is elevated.

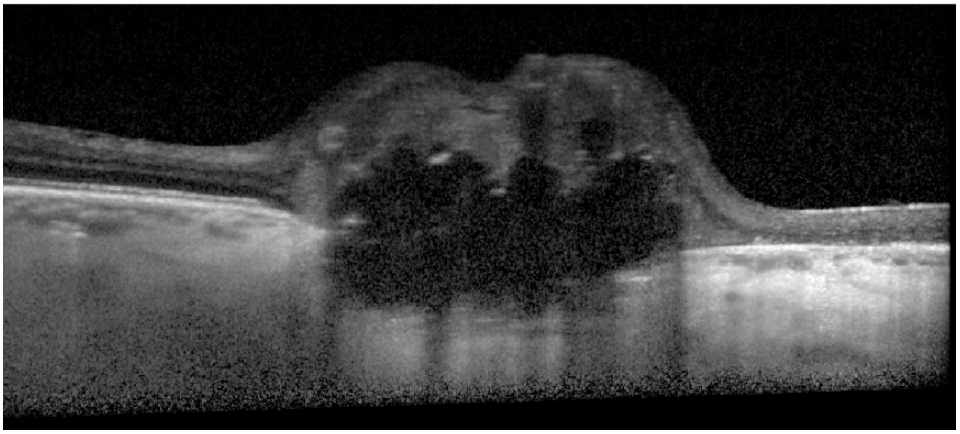

Figure 2.3: EDI-OCT image of the ONH (optic nerve head) with presence of ODD. ODD causes disc elevation.

2.2.1 Pathogenesis of ODD

The pathogenesis of ODD is unknown, but two theories exist.

The first theory relates to the size of the scleral canal [15]. A small scleral canal may lead to axonal damage and ganglion cell death due to compression of axons. The compression blocks the axonal flow, which is the cellular process of transporting proteins, lipids and mitochondrias among other along the axon. A blockage of the axonal flow leads to intracellular (inside the axon) calcification of mitochondrias. The calcification of mitochondrias forms the drusen.

The second theory for the pathogenesis of ODD is abnormal axonal metabolism. A disturbance in the axonal metabolism leads to axonal rupture and extrusion of mitochondrias. In the same way as in the first theory, ODD forms by calcification of mitochondrias, but here the calcification of the mitochondrias happen in the extracellular space (outside the axon).

CHAPTER 3

Optical Coherence Tomography and angiography

This chapter contains background information about OCT and OCT angiography. First, a description of the technical principles behind OCT, the acquisition set-up and well-known artefacts in OCT are given. Second, a short description of OCT angiography, its possibilities and limitations and well-known artefacts are given.

3.1 Optical Coherence Tomography

Optical Coherence Tomography (OCT) is a non-invasive imaging technique primarily used for imaging of the retina. Apart from its use in ophthalmology, OCT is also used in dermatology for imaging skin layers. The technique can produce real-time cross sectional images with a high resolution.

OCT was invented in 1991 and the first device entered the market in 1996. Since then, the technique has undergone a great development and has become the standard tool for diagnosing a range of ophthalmic diseases including glaucoma, diabetic retinopathy and age-related macula degeneration (AMD) [16]. Many of these deceases causes a change in the thickness of the retinal layers and OCT is very suitable for imaging the retinal layers.

To understand the possibilities and limitations of the technique, it is necessary to understand the general principles behind OCT, the acquisition set-up and to know some of the well-known artefacts for OCT.

3.1.1 Principles of OCT

The principle behind OCT is comparable with the principle behind ultrasound, but with the use of light instead of sound. In ultrasound, the depth measure is obtained directly by measuring the sound echo times while in OCT, the depth measure is based on the reflected light. OCT uses near-infrared light and the beam of the backreflected waves cannot be measured directly as in ultrasound. Therefore a reference measure is used.

With the use of an interferometer, a beam splitter splits the light into a part directed to the sample and the another part to the reference located at a well-known distance. The interferometer is the underlying principle behind all OCT implementations [16].

Figure 3.1 illustrates the principles behind the three types of OCT. The first generation of OCT was the Time Domain (TD) OCT where the backscattered light was detected in the time domain. The light source emits low coherence light and at the beam splitter, the beam is split into a sample beam and reference beam. The sample beam penetrates the sample and backscatters, while the reference beam travels to the reference mirror and backscatters. The interference between the backscattered light from the reference and the sample is measured at the detector. A high interference signal is obtained when the optical path lengths are equal, which makes the two waves interfere constructively. To obtain high interference, the optical path length shall be less than the coherence length of the light source. The coherence length of the light source is defined as the distance the light propagates while maintaining a degree of coherence.

To get the complete depth profile at that one point of the sample, the distance to the reference mirror is varied. The complete depth profile at the one point of the sample is called **A-scan**. To obtain a cross section image, named **B-scan**, the sample beam is scanned laterally across the sample. TD OCT was the first generation of OCT and the fact that the distance to the reference mirror is varied to obtain each A-scan makes the imaging speed slow. As result, the imaging quality is limited by the slow imaging speed.

The second generation of OCT is the frequency domain OCT, where spectral information is used to generate A-scans. For this type of OCT, there exist two types of OCT; the spectral domain (SD) OCT and the swept source (SS) OCT.

For the SD-OCT, the light source is a broad band light source and the detector is replaced by a spectrometer. At the spectrometer, the different wavelengths of the backreflected light are seperated into a line image which is recorded by a high speed line scan camera [16]. The depth profile is determined as the Fourier transform of the interference frequency spectrum, for which the higher the frequency, the greater depth of origin. The reference mirror is kept fixed and compared with TD OCT, the scan time is shorter and the image quality higher.

In the work behind this thesis, I have used the SD-OCT primarily SPECTRALIS from Heidelberg. It was invented in 2006 and is a SD-OCT combined with a scanning laser ophthalmoscope (SLO). The SLO enables motion tracking and the ability to scan the same area at a later time by combining the fundoscopy image with the OCT image.

Swept source (SS) OCT as the name indicates uses a sweeping light source to seperate the wavelength in a similar way as the spectrometer in SD-OCT.

For the work behind this thesis, an important development in OCT is the invention of **Enhanced Depth Imaging (EDI) OCT** [18]. EDI-OCT enables imaging of deep located structures, the deeper layers of the retina and the choroid (vascular layer under retina) more clearly than standard SD-OCT.

There are several reasons why the resolution of deep located structures is poor in standard SD-OCT, below are some of them [18–20].

- **Scattering and absorption**. The scattering and absorption in the sample cause

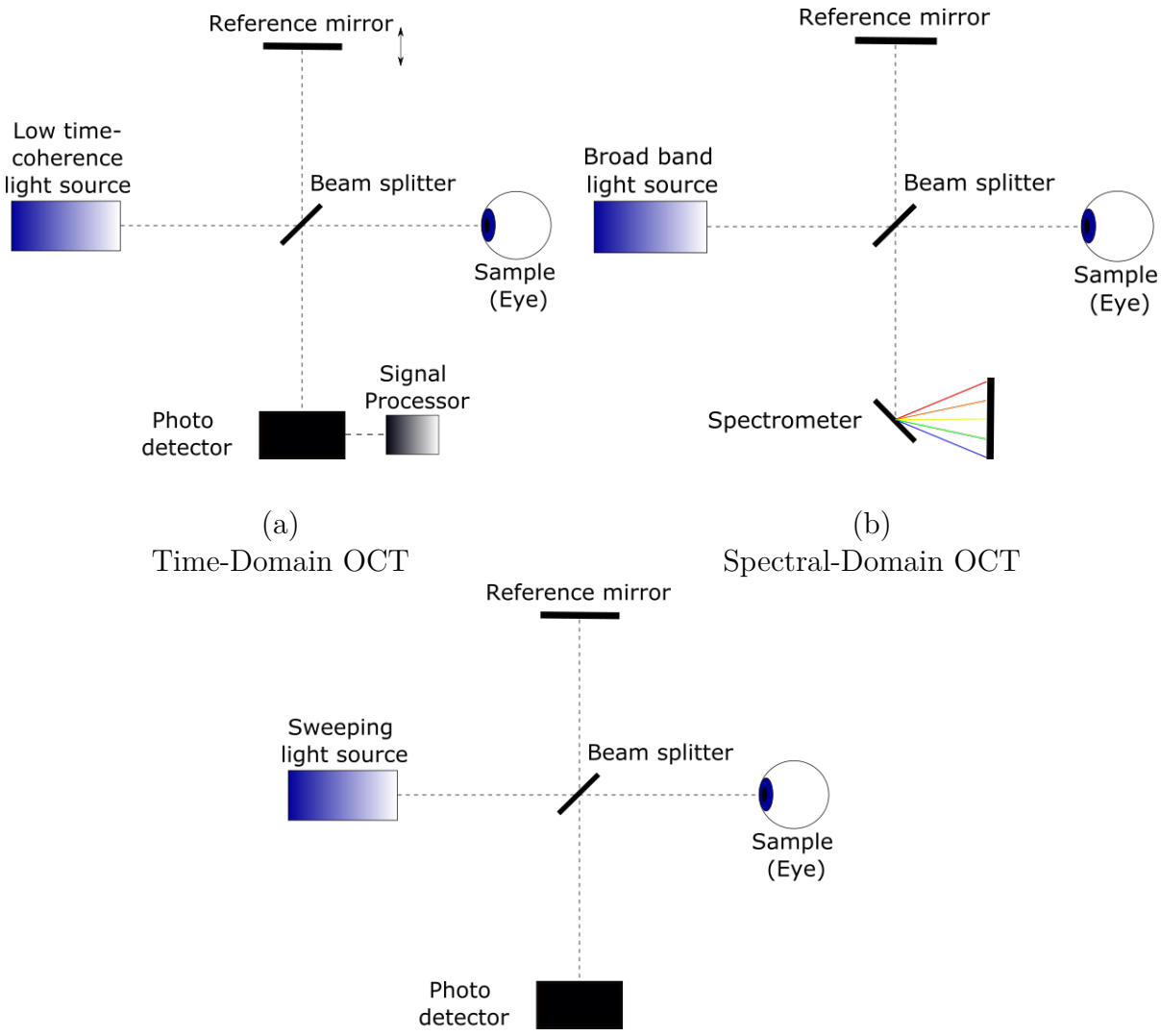

(a) Time-Domain OCT

(b) Spectral-Domain OCT

(c) Swept-Source OCT

Figure 3.1: Illustration of the three types of OCT. The set-up is similar for all three types starting with a light source emitting light (input beam). The input beam is afterwards divided by a beam splitter into two beams - a reference beam and a sample beam. The reference beam travels to a reference mirror and the sample beam to the sample (the eye). A detector measures the interference between the back-scattered light from the reference and the sample. (a) shows Time-Domain OCT, where the reference mirror is moving and the light source is a low coherence light. The light is detected in the time domain. (b) shows Spectral Domain (SD) OCT, where the backreflected light is detected at a spectrometer and the light is broad band light. Depth profile is found in Fourier domain. (c) shows Swept Source (SS) OCT, where the light comes from a sweeping light source and the depth profile is found in the Fourier domain. Figure inspired by [16] and [17].

the light intensity to decrease exponentially with depth [20]. Deeper penetration is furthermore limited because of scattering by the RPE (retinal pigment epithelium) layer and choroid vasculature [18].

- **Detector type**. Deep located structures result in higher frequencies in the interference spectrum, while near located structures give low frequencies. The frequency response of the used detector limits the obtainable penetration depth.
- **Type of light source**. The center wavelength and bandwidth of the broad band light source control both resolution and tissue penetration. Short center wavelength results in high resolution, but decreased tissue penetration, while large bandwidths provide higher resolution at any frequency. The use of infrared light has a penetration depth of a few hundred microns which matches the depth of the retina, but not the choroid.

EDI-OCT is a modification of SD-OCT and incorporated in Heidelberg SPECTRALIS. In standard SD-OCT, two images are obtained: the real image and the inverted image. Normally, only the real image is shown on the screen such that the inner part of the retina is facing up and the choroid is at the bottom of the screen. If the instrument is moved closer to the eye, the inverted image is shown on the screen. In the inverted image the choroid is placed at the top of the image, closest to zero-delay. In this case, the choroid is imaged with a higher sensitivity. In practise to obtain EDI-OCT, the patient keeps it position and focus of the eye on the screen, while the instrument is moved closer to the eye. To get the highest image quality, the imaged structures need to be as close to the top of the screen. Furthermore, averaging with around 100 frames or more should be used.

3.1.2 Acquisition and resolution

The acquisition of an OCT volume can be described as a set of line scans. Each B-scan, the cross-section image, is obtained by recording A-scans, the depth profiles, at several points along a scan line. With acquisition of multiple parallel line scans, B-scans, 3D volume can be generated. Fig. 3.2 illustrates the scan setup and the directions (axial, lateral and transversal).

The resolution in each direction is limited by various factors. Resolution in the axial direction is around 3.9 μm and is mainly determined by the coherence properties of the light source. Resolution in the lateral direction is around 5.7 μm and is limited by the quality of the optical system. Resolution in the transversal direction is about 15 μm and is limited by the scan speed [17].

3.1.3 Artefacts

The most common artefacts in OCT are shadowing and artefacts caused by patient movement. During acquisition, the distance to the eye needs to be fixed. Therefore the

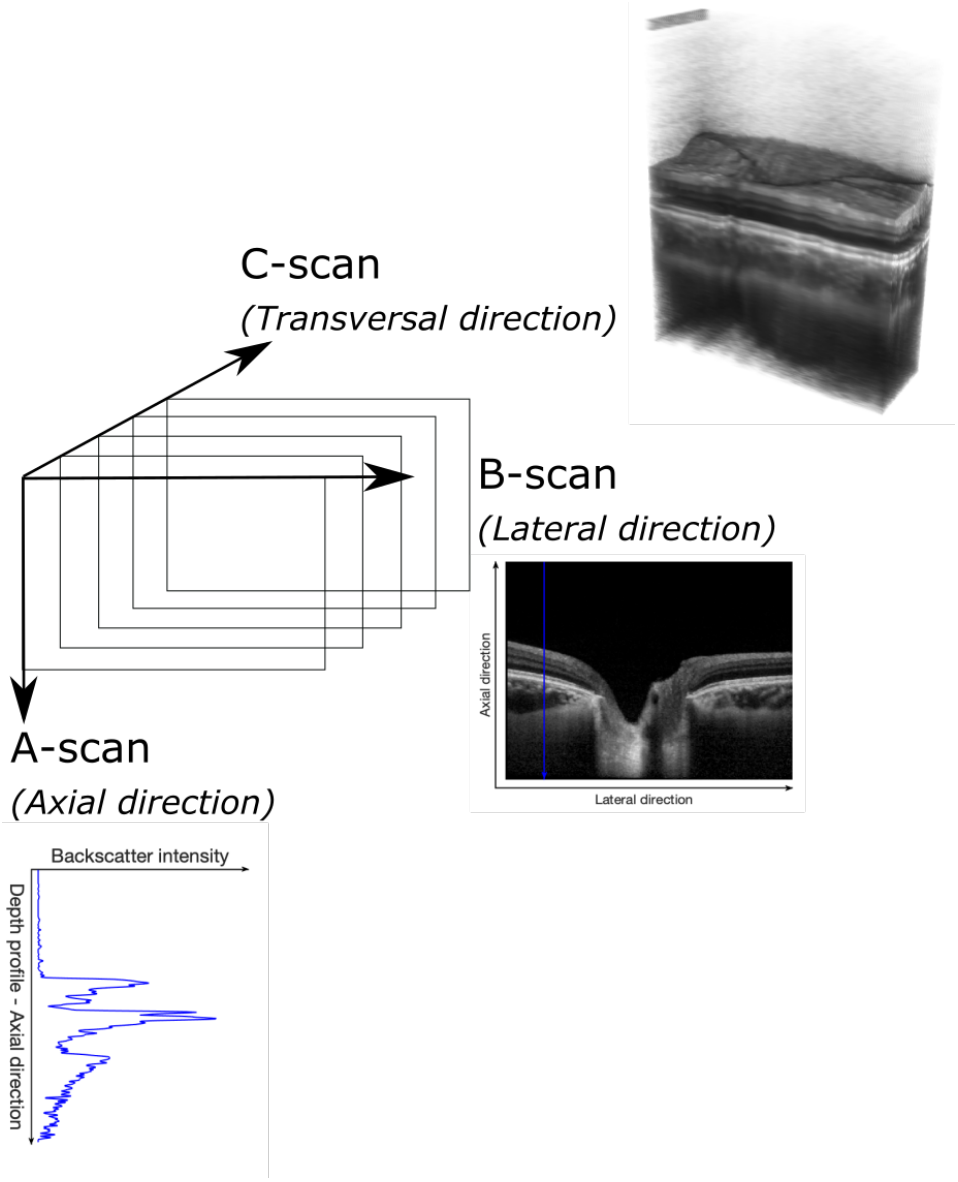

Figure 3.2: OCT scan setup. A-scans are depth profiles obtained from the backscattered light in the axial direction. B-scans are cross-sectional images consisting of several A-scans acquired along the lateral direction. The shown A-scan (depth profile) is marked as a blue line in the B-scan. C-scans or the 3D scan volume consists of multiple B-scans acquired along scan lines the transversal direction.

patient's chin rest on a holder and the forehead is leaned against the forehead support.

Motion artefacts are common and can be seen in different ways. A small movement in the lateral direction will cause missing information in the B-scan, typically in the edges of the B-scan. Larger movements in the transversal direction will, as described above, replace the real image with the inverted image where the order of the retinal layers is reversed. Furthermore, eye blinking will cause lack of information and is seen as a black line in the cross sectional image in the lateral-transversal direction, called the **en face image**. The black line is an empty B-scan, acquired at the time of blinking.

Shadowing comes from signal loss primarily due to large structures that reflect or absorb most of the light and thereby no signal from below exists. In an OCT scan of the optic nerve, shadow artefacts are seen below the large vessels located in the upper layers of the retina. The shadow artefact complicates a segmentation of ODD.

Figure 3.3 shows two of the common artefacts. Figure 3.3(a) shows the shadow artefact from large vessels in the top layer of the retina and Figure 3.3(b) shows the artefact from a small movement in the lateral direction, where information in one side of the B-scan is missing.

3.2 Optical Coherence Tomography Angiography

Optical Coherence Tomography Angiography (OCTA) is an extension of OCT that makes it possible to image flow of blood without use of dye injections. The technique was first described in 2006, but the first clinical study was published in 2014 and the technique has become available in the clinic during this PhD project.

Before OCTA, the flow of blood was imaged using flourescein angiography and indocyanine green angiography, but these modalities need intravenous injections of contrast agents and can only produce 2D images of vessels [21]. OCTA produces 3D volumes in the same tomographic way as structural OCT. This means that investigation of vessels at different depths is possible, e.g. changes in the retinal or choroidal vascular structure. Structural OCT cannot image these vascular changes due to low contrast between capillaries and retinal tissue. Moreover, for some diseases, imaging of only those capillaries which have blood flow is needed to monitor degeneration or occlusion of capillaries.

OCTA B-scans are generated from multiple structural OCT B-scans acquired rapidly after each other at the same position. Afterwards, the difference between the B-scans is computed. Since the retinal layers and other structures in the retina are still, the differences are assumed to come from moving blood elements.

To provide a simple overview of the vascular structures, the information is projected into 2D images. This is normally done by dividing the scan volume into sub volumes with the use of slabs. Slabs are defined as the sub volume between two surfaces, typically two of the retinal layers. The information in the slab is then projected to get a 2D overview image, an **en face angiogram**.

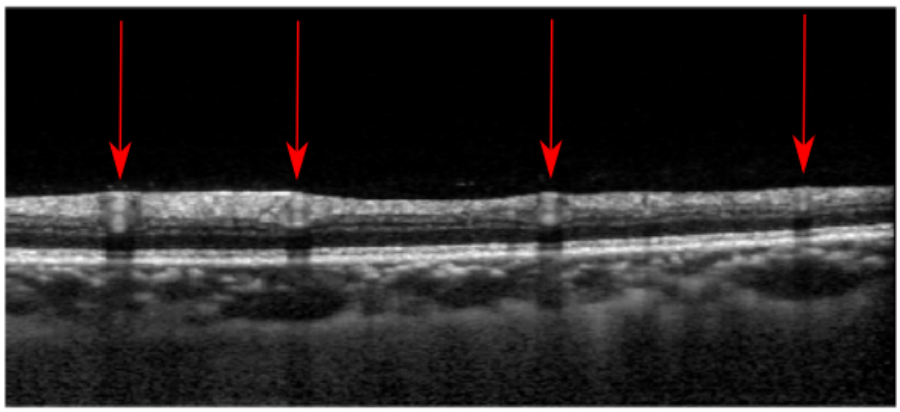

(a)

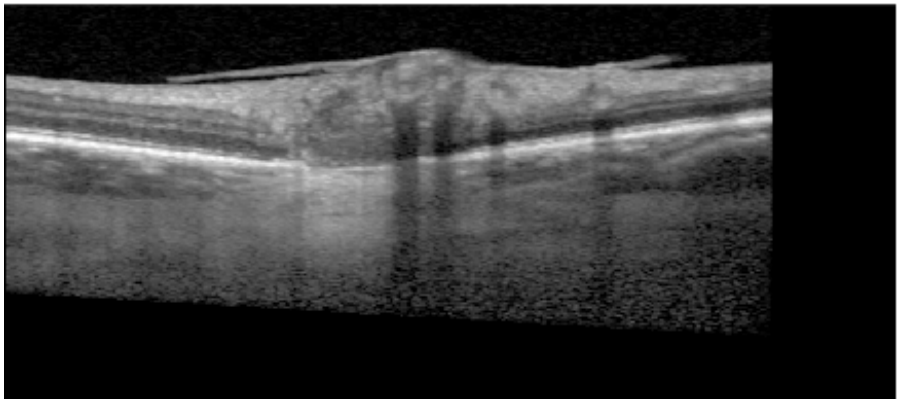

(b)

Figure 3.3: Illustration of two common artefacts in OCT. (a) shows shadow artefact caused by absorption or reflection of the signal by the large vessels in the top layer of the retina. Large vessels are marked by red arrows and the missing signal below them is clearly seen as a shadow. (b) shows movement artefact from small movement, causing missing information in one of the sides of the B-scan.

Figure 3.4(a) shows the defined slab, here defined between the ILM (inner limiting membrane) and 150 μm below. Figure 3.4(b) shows the OCTA B-scan for the same B-scan shown on (a). Figure 3.4(c) shows the computed en face angiogram for the sub volume defined by the slab in each B-scan.

It is not possible to measure the blood flow as a numeric value with OCTA. A high intensity in the OCTA volume is related to a large change in time e.g. flowing red blood cells, but the relationship between flow speed and large changes in time is not linear and depends on OCT beam size and the size of the blood vessel (speckle size). This is important to know since the blood flow would be an extremely useful measurement for several diseases. In this thesis, the OCTA scan is used to measure the vessel density to express degeneration or occlusion of capillaries in the ONH.

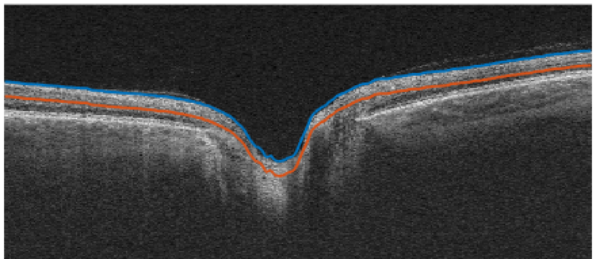

(a)

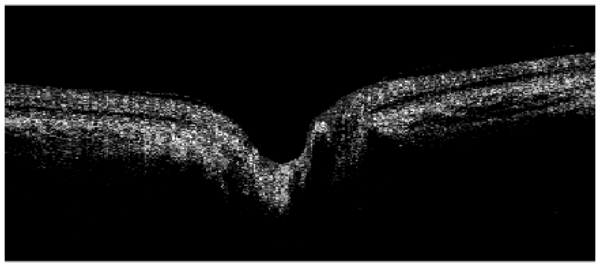

(b)

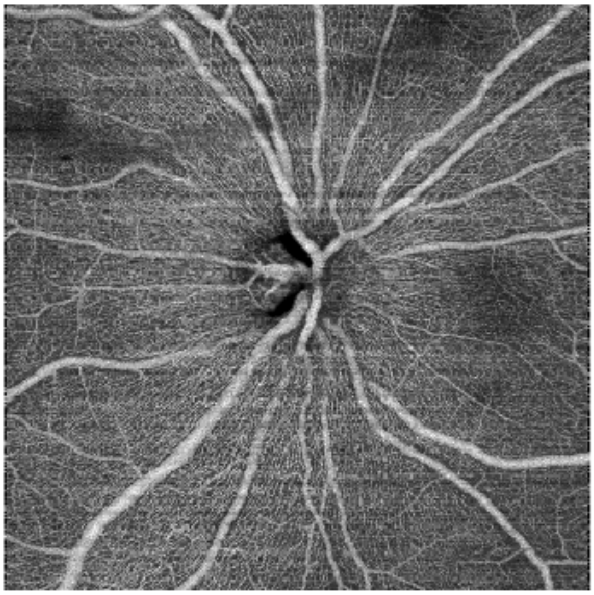

(c)

Figure 3.4: Generation of en face angiogram from 3D OCTA volume. (a) Structural OCT B-scan used to define slab. Blue curve is the ILM (Inner Limiting Membrane, see table 2.1) and red curve is 150 μm below. (b) OCTA B-scan and (c) the en face angiogram.

3.2.1 Artefacts

Artefacts in OCTA arise from several reasons such as image acquisition, intrinsic characteristics of the eye, projection artefacts, eye motion or image processing [22]. At acquisition of OCTA, the same artefacts as for structural OCT can occur e.g. due to lack of signal caused by eye blinking or patient movement. Moreover, it is important to repeat the B-scans multiple times and to use a high scan speed compared to structural OCT.

Artefacts can be caused by clinical factors as the intrinsic properties of the eye and the ocular pathology being imaged. Some diseases may cause large attenuation which leads to signal loss. This results in a artefact of missing information which makes it is hard to determine if flow is present or not in the affected area.

Projection artefacts are always present for OCTA. This is because OCTA builds on the reflected light from moving blood cells, but the light can also be refracted or absorbed as it passes through a blood vessel. Some of light also passes the blood vessel and is reflected as it hits the RPE. This light changes over time which causes the appearance of pattern of overlying vessels in the RPE. The artefact is known as the OCTA projection artefact [22]. Any reflecting surface will appear to change over time and this artefact may be present in all deeper layers of the retina, the choroid or the sclera. It is possible to partly compensate for the projection artefact by subtracting the en face angiogram of the overlying layers. The artefact can easily be identified by examining the en face angiogram at different depths.

OCTA builds on the motion of blood elements but any other motion may also affect the images. Patient movements or eye movements will create changes between the repeated B-scans and the appearance of such artefact depends on the motion. Movement in the axial direction always occurs as it relates to the cardiac cycle and breathing. This movement causes a displacement of the entire retina, which may show false positives of flow movements in the image if no registration between B-scans is used.

Movement of the eye e.g. microsaccade leads to acquisition of B-scans at different positions. There is a large difference (no correlation) between these B-scans and artefacts show as a white line and a small shift in the vessel structure in the en face angiogram.

To correct for this artefact, registration between scan volumes is acquired. In [23] they perform horizontal and vertical scan to be used for this registration. Registration is performed based on individual A-scans and is computationally heavy. It may also induce some artefacts itself e.g. vessel doubling, stretch artefacts and quilting defects.

Finally, image processing may cause artefacts as well. The en face angiograms are highly dependent on the correctness of the segmentation of the retinal layers. Errors in the location of the slab will create areas with missing information or wrong information. This is more likely to happen when working with non healthy eye since the segmentation of the layers is more likely to fail.

3.3 Used scanners

The following scanners have been used in the work behind the thesis.

OCT scans were acquired with SD EDI-OCT Heidelberg Spectralis (HRA+OCT, Heidelberg Engineering) performed with high resolution, eye-tracking and averaging of B-scans. The resolution was 5.7 μm (axial) $\times$ 3.9 μm (lateral) $\times$ 30μm (transversal) for data set used in paper A, B and C.

OCTA scans were acquired with SS OCTA Topcon DRI OCT Triton. The scan was a 6 $\times$ 6 mm giving a approximately resolution of 8 μm (axial) $\times$ 19 μm (lateral) $\times$ 19 μm (transversal) for the data set used in paper C.

CHAPTER 4

Quantification of Optic Disc Drusen

In this chapter the research behind this thesis is addressed. First, it contains a presentation of the research questions and how they relate to the three journal paper (paper A, B and C) listed in contributions. In the following sections, the research questions are addressed. The used methods are described together with a discussion of challenges and considerations made.

4.1 Research questions

In this PhD project, we wanted to quantify ODD. The motivation was the still unknown pathogenesis of ODD and with the availability of the new imaging technique EDI-OCT, new possibilities arised.

Before the start of the PhD project, imaging of ODD with OCT was not very thoroughly described or used. The standard tool in the clinic for diagnosing ODD was ultrasound combined with fundoscopy, which only could be used to determine whether or not ODD was present.

OCT was able to image ODD, but the technique of standard SD-OCT (Spectral Domain OCT) had difficulties in imaging the deeper layers of the retina clearly enough to image deep located ODD. The lower boundary of ODD for deep located ODD could not be imaged with standard SD-OCT.

We started by study the use of new OCT technique, EDI-OCT, for quantification of ODD as a 3D structure. The aim was to produce a quantitative measure of ODD location and volume. These measures were of interest to investigate the influence of ODD on the optic nerve function.

It was of interest to investigate whether more information about ODD could be obtained with the use of en face images. To improve the appearance of the en face images, we combined two orthogonal EDI-OCT scans and quantified the best interpolation method for solving the problem of interpolation.

At last it was of interest to combine the found ODD location and ODD volume with vascular information. OCTA was a new technique to image blood flow. A compression of the vascular system by ODD may lead to development of visual field defects [24]. By combining ODD anatomical information from EDI-OCT with blood flow information

from OCTA, we tried to quantify the influence of ODD volume on the local vessel density.

The main research questions were

1. Can EDI-OCT be used to quantify ODD as a 3D structure and how can the anatomical location of ODD be measured? *(Paper A - Quantitatively Measured Anatomic Location and Volume of Optic Disc Drusen: An Enhanced Depth Imaging Optical Coherence Tomography Study)*

2. How can information from two orthogonal EDI-OCT be combined to improve the visual appearance of the an en face image? Which interpolation method should be used for solving the problem of interpolation from grid lines? *(Paper B - Linear, Transfinite and Weighted Method for Interpolation from Grid Lines Applied to OCT Images)*

3. How can the local vessel density be expressed from OCTA scans? Is it possible to quantify compression of the vascular system from large ODD? *(Paper C - Determination of peripapillary vessel density and the influence of optic disc drusen from EDI-OCT and OCT angiography)*

4.2 Quantification of ODD as a 3D structures - related to paper A

A quantification of ODD as a 3D structure gives the opportunity to quantitively measure ODD volume and ODD location in the optic nerve head. This is of interest in the investigation of the impact of ODD volume and location on the optic nerve function and the vascular system. In paper A *(Paper A - Quantitatively Measured Anatomic Location and Volume of Optic Disc Drusen: An Enhanced Depth Imaging Optical Coherence Tomography Study)*, we address the problem of quantifying ODD in 3D and use it for investigation of its impact on the optic nerve function.

4.2.1 ODD segmentation - assumptions and challenges

At the time we published paper A (2017), a quantitative measure of ODD volume had only been described once before in a study by Yi et al [25]. The study by Yi et al [25] was published in 2009 and they manually segmented ODD in SD-OCT scans from 9 patients. The problem with SD-OCT for imaging of ODD, as described in chapter 3, is the poor imaging of deep located structures. Deep located ODD and lower boundary of ODD are not visible or poorly imaged in SD-OCT B-scans.

In our study, EDI-OCT scans of 37 ODD patients were acquired and the new imaging technique EDI-OCT improved remarkably the visibility of the lower boundary of ODD. Figure 4.1 shows the same ODD imaged with (a) SD-OCT and (b) EDI-OCT.

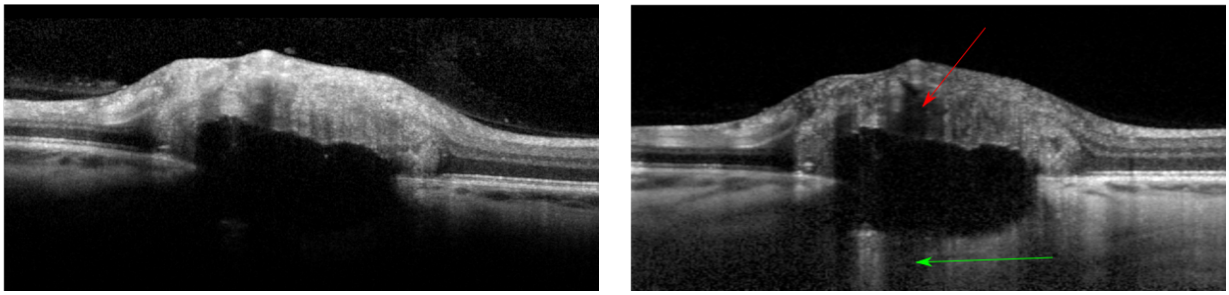

(a) (b)

Figure 4.1: Visualization of ODD. (a) SD-OCT (b) EDI-OCT. On (b) a large blood vessel (red arrow) and the shadow artefact (green arrow) are marked.

In order to quantify ODD, we performed a manual segmentation of each individual ODD in the EDI-OCT volume. The segmentation was performed with the software ITK snap [26], where each ODD was segmented in 2D in each B-scan with a polygon tool. The polygons in all B-scans were connected to form a 3D structure. All segmentations were performed by same medical doctor, Lasse Malmqvist.

The first challenge in the segmentation process was that, to the best of our knowledge, ODD in EDI-OCT images were not well described in literature. However, their appearance and characteristics in EDI-OCT images were comparable with those in SD-OCT images. ODD appear as hyporeflective structures with a full or partial hyperreflective margin. The segmentations were based on experiences from earlier studies [27–30]. Later the same year as Paper A was published, a description of ODD in EDI-OCT was published by Lasse Malmqvist [31].

The decision of performing a manual segmentation was made based on the following considerations. First of all, the focus of the paper was not on automation of the segmentation. Furthermore, in order to evaluate an automatic segmentation, a ground truth was needed. The closest we could get to a ground truth was a manual segmentation.

Other challenges for the segmentation were the unknown variation in ODD volume and shape. The only study published about measurement of ODD volume was the study by Yi et al [25]. The shape of ODD had not been quantified before. In literature, ODD was described as a spherical structure.

The results of our segmentation revealed different shapes of ODD. In 2D, in each B-scan, most ODD appeared fairly circular. When combined into 3D, not all ODD were spherical structures. Figure 4.2 shows six manual segmented ODD in the same EDI-OCT scan volume. Many of them are spherical structures, but some are elongated or maybe a group of many small ODD close together.

A group of many small ODD is known as a conglomerate. In the case of ODD conglomerate, we made the assumption of belonging to one ODD in the manual segmentation. Figure 4.3a shows a B-scan with a conglomerate of ODD and Figure 4.3b shows the ODD segmentation marked with green.

Lastly, the attenuation and reflection of light by ODD were unknown. A large at-

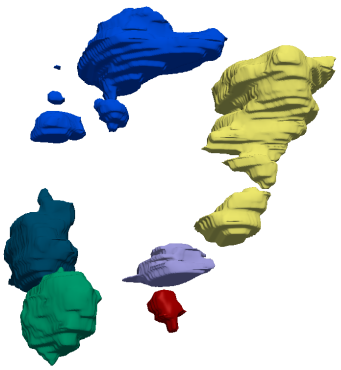

Figure 4.2: 3D representation of six ODD manual segmented from an EDI-OCT scan. Each color represent an ODD.

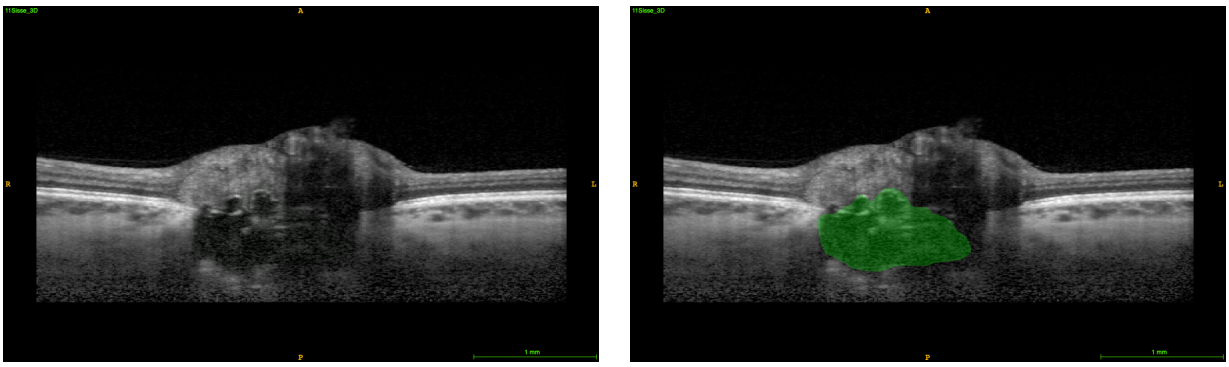

(a) (b)

Figure 4.3: Conglomerate of ODD. (a) shows an EDI-OCT B-scan of a conglomerate of ODD. (b) shows the conglomerate segmented as one ODD marked with green.

tenuation or reflection would challenge the segmentation because of missing signal as seen with shadow artefact. Shadow artefacts are seen for the large blood vessels in top layers of the retina. The signal is attenuated and reflected by the blood vessel and signal below the vessel is missing. Figure 4.1(b) illustrates the shadow artefact, where the blood vessel is marked with a red arrow and the shadow below the ODD is marked with a green arrow.

ODD had only been imaged with SD-OCT where the lower boundary was missing for deep located ODD due to limitations of imaging in depth. The lower boundary of small superficial ODD could be seen on SD-OCT. In EDI-OCT images, the lower boundary was more clearly imaged for some ODD compared to others. The amount of light attenuation may depend on the ODD volume and the composition of content of the ODD.

4.2.2 Measurement of ODD anatomic location

As a part of quantifying ODD as a 3D structure, we wanted to measure its anatomical location in the optic nerve head. The anatomical location of ODD is of interest both in the investigation of the pathogenesis of ODD, but especially in the investigations of complications caused by ODD.

ODD can be classified into two groups, burried and superficial, based on their visibility on ophthalmoscopy. An ODD is classified as superficial if it is visible on ophthalmoscopy, while burried ODD only can be confirmed by ultrasound or OCT. The classifications relate to how deep the ODD is located in the retina. Deep located ODD can often not be seen on the ophthalmoscopy and are classified as burried ODD. However, the visibility on ophthalmoscopy also depends on ODD size, thinning of RNFL (retinal nerve fiber layers) [32], the degree of calcification of the ODD, age and optic nerve head anatomy. Over time some ODD migrate to the upper layers of the retina and change from being deep burried ODD to superficial ODD. This may cause elevation of the optic disc [33, 34].

To the best of our knowledge, measurement of the anatomical location of ODD in 2D or 3D has not been described before in literature. To describe the vertical anatomic location of ODD, the obvious measure is the distance from top layer of the retina, the inner limiting membrane (ILM), to the ODD.

However, ODD causes changes of the ILM e.g. when elevation of the optic disc is present. How much the disc is elevated depends on the ODD size, and how deep the ODD is located. Several ODD may cause changes of the ILM and the ILM is therefore not a good choice of a reference surface for measuring how deep the ODD is located. Figure 4.4 shows on (a) a B-scan of the ONH for a healthy subject and on (b) a B-scan of the ONH for an ODD patient with optic disc elevation.

The main challenge for measuring how deep the ODD is located in the retina, is the choice of a reference point. In a study by Lee et al [35], the height of the ODD is measured perpendicular to the RPE (retinal pigment epithelium) layer in the retina.

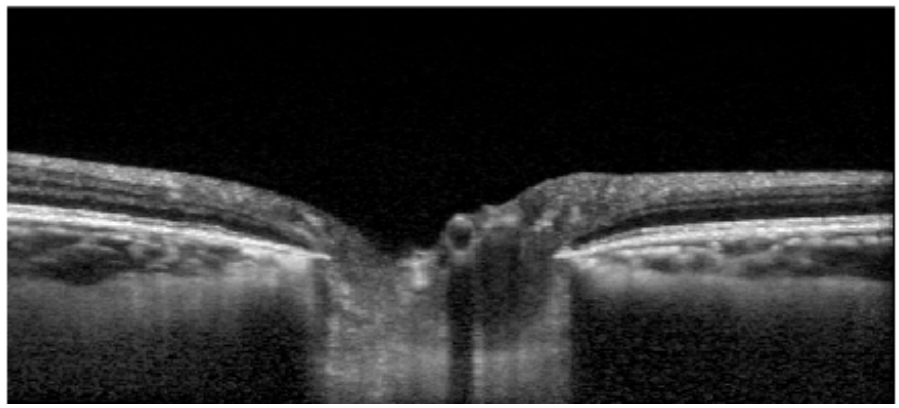

(a)

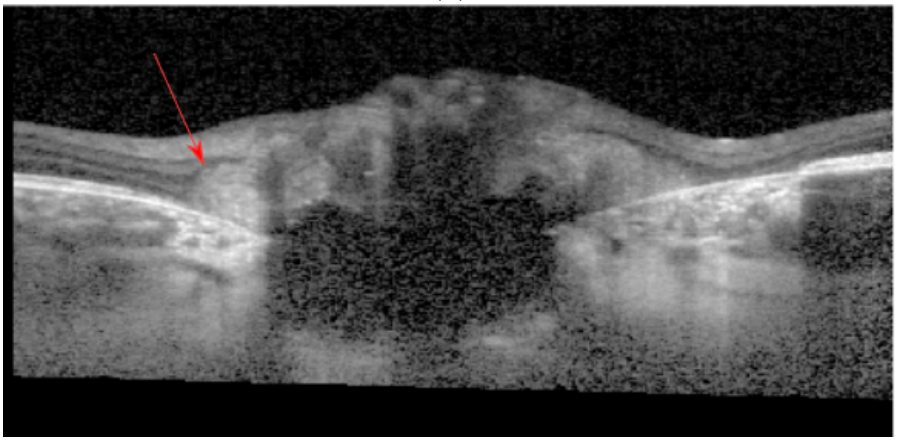

(b)

Figure 4.4: EDI-OCT B-scan of the ONH (optic nerve head) for (a) a healthy subject and (b) an ODD patient. On (b) the presence of a peripapillary hyperreflective ovoid mass-like structures (PHOM) is marked by a red arrow.

The RPE layer is the bottom layer of the retinal layers and is always clearly imaged in an OCT image because of its hyperreflective nature. The problem with using the RPE layer as reference surface is that the RPE layer ends in each side of the ONH. This opening is known as the opening of Bruchs membrane (BM) or the scleral canal as described in section 2.1.1 and shown in Figure 2.2. The RPE layer is therefore not present at in the middle of the ONH where ODD are located.

A reference surface could be based on the RPE layer with an estimated closure of the opening in the middle. However, the RPE layer in each side of the opening is often inclined instead of horizontal for ODD patients. The reason for this is the presence of peripapillary hyperreflective ovoid mass-like structures (PHOMS) (Figure 4.4).

Based on these considerations, we decided to measure the vertical anatomic location of ODD in the following way. The RPE layer in the margin of the B-scan was detected with a graph-based layered surface detection method [36], which is described in the following section. A reference surface was fitted to the detected part of RPE layer.

The vertical distance from the ODD center of mass to the reference surface served as a measurement for the vertical anatomical location of the ODD. A negative sign indicated that ODD was located above the reference surface and positive sign below the reference surface.

Figure 4.5(a) shows the detected part of the RPE layer (blue line) together with the reference surface (green line) and the vertical distance (red dotted line) to the center of mass (magenta star) of the ODD. Figure 4.5(b) shows a 3D representation of the segmented ODD together with the ILM (marked with red arrow) and reference surface (marked with green arrow). The ILM was detected with the graph-based layered surface detection method too.

4.2.3 Layered Surface Detection

Layered surface detection is a graph-based method for segmentation of layered structures or surfaces in 2D or 3D [36]. The method is widely used for segmentation of the retinal layers in OCT images [37–39].

The method is based on optimal net surface detection via graph search originally described in [40] and is used for segmentation of layers divided by terrain-like surfaces or lines.

The terrain-like surface or line to be found should have a minimum cost and should satisfy the smoothness constraints Δx and Δy. The smoothness constraints Δx and Δy define how much the height of the surface is allowed to change between the columns when moving along the x- and y-direction. The columns here correspond to columns of the volume.

Furthermore, as input to the method, a volumetric cost function is given. The volumetric cost function may be an on-surface cost that defines the optimal placement of the surface to be found. The volumetric cost function needs to be defined such that voxel values, at the wanted place for the surface, are low, while remaining voxel values are high. The construction of the volumetric cost function is important for the performance of the method. How to construct the volumetric cost function depends on the data. Often the surface needs to be placed where voxel intensities change in intensity, and this information can be used when defining the volumetric cost function.

When detecting two or more surfaces, the expected thickness between the two layers may be given as an additional input.

The method can be extended to use a second cost function, based on the appearance of the for regions between layers. The cost for regions are defined in a similar same way as the on-surface cost function, but here the voxel values between the layers are low while remaining voxel values are high.

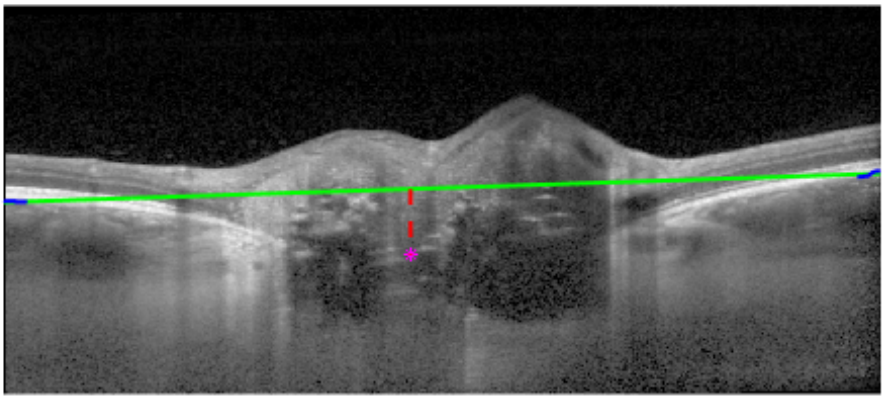

(a)

(b)

Figure 4.5: Reference surface based on Bruch's membrane. On (a) vertical distance (red dotted line) from reference surface (green line) to ODD center of mass (magenta star) in B-scan. On (b) 3D visualization of ODD with ILM (red arrow) and reference surface (green arrow).

4.3 Interpolation from grid lines - related to paper B

Optical coherence tomography is a tomography technique, which means that multiple cross sectional images are acquired and combined into a volume. The cross sectional image is the so-called B-scan, which is acquired along a scan line. The acquisition of multiple B-scans are performed as a set of parallel scan lines. The depth profiles, the A-scans, are acquired at sample points along each scan line. The distance between the scan lines (B-scans) is much larger than the distance between sample points (A-scans) along the scan line.

It is of interest to visualize the information in transverse plane of the retina, known as the en face image. Because the resolution is much coarser between the scan lines than along them, pixels become non-square and elongated in the en face image. Figure 3.2 illustrates the sample points for an OCT scan with resolution of 5.7 μm (axial) $\times$ 3.9 μm (lateral) $\times$ 30 μm (transversal). This is the resolution of the OCT scans used in the work behind this thesis. Figure 3.2(a) shows the sample points in the plane of the en face image and Figure 3.2(b) shows the sample points in the plane of the B-scan.

The elongated pixels in the en face image affect the visual appearance of structures in the image. An example of this is small blood vessels that run in the direction parallel to scan direction. These small blood vessels are not visible on the en face image. Another example is some anatomical structures that are hard to distinguish from background. Furthermore, the en face image has a striped look with stripes running in the same direction as the scan direction.

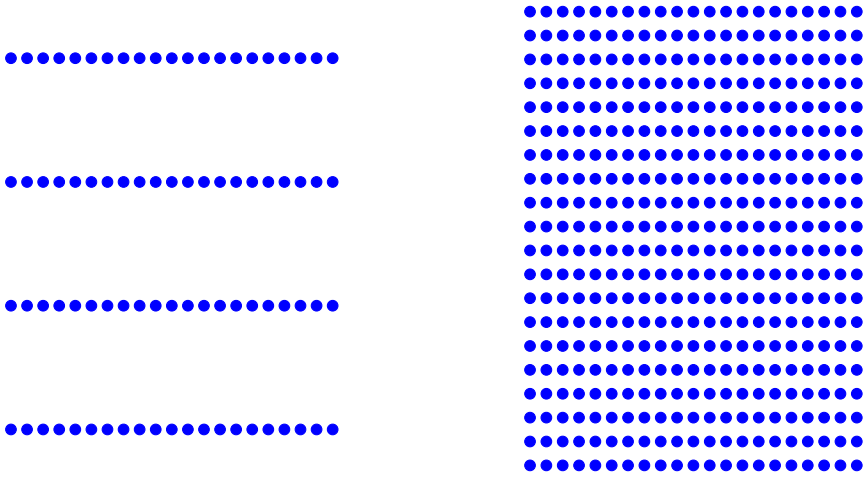

(a) (b)

Figure 4.6: Illustration of sample points for an OCT scan with resolution 5.7 μm (axial) $\times$ 3.9 μm (lateral) $\times$ 30 μm (transversal). On (a) the sample points in the en face view (lateral-transversal plane). On (b) the sample points in the B-scan (axial-lateral plane).

To improve the en face image, we address the problem of combining two orthogonal OCT scans in paper B (*Linear, Transfinite and Weighted Method for Interpolation from Grid Lines Applied to OCT Images*). The combining of two images with orthogonal scan direction was not straight forward, since pixels were sparsely sampled in one direction in first image and in the other direction in the second image. We wanted to preserve the information along each scan line, while interpolating at regularly spaced pixel position inside each square formed by the orthogonal scan lines. To the best of our knowledge, the problem of interpolation from grid lines while preserving boundary values had not been addressed for image interpolation before.

Figure 4.7 shows the set up for the interpolation. Before the interpolation was performed, the two scans were registered to each other and points were resampled along the scan lines. This is described more detailed in section 4.5, as we addressed a similar problem in the work behind Paper C. It is a recurring problem when working with OCT data because of the data structure.

In paper B, we tested and evaluated three interpolation methods for solving the interpolation problem. The methods were tested on two sets of images; a data set consisting of photos of various scenes and a data set consisting of fundoscopy images. The images were downsampled to construct a ground truth for the interpolation result. At the downsampling, we kept image rows and columns at a certain distance, which corresponds to the upsampling rate. Afterwards, the images were upsampled using one of the three interpolation methods. The three interpolation methods; linear, transfinite and weighted interpolation are described very detailed in paper B (Appendix B) and will therefore not be described here.

4.3.1 Statistical test for evaluation of interpolation method

The performance of the three interpolation methods was evaluated to determine which method performed best at a given upsampling rate.

The quality of the interpolation was measured by the peak-signal-to-noise (PSNR) defined as [41]

$$\mathrm{PSNR} = 20 \log_{10} \left(\frac{\mathrm{MAX_I}}{\mathrm{RMSE}} \right) \tag{4.1}$$

where $\mathrm{MAX_I}$ is the maximum pixel intensity value (1 in our case) and RMSE is root mean square error defined as

$$\mathrm{RMSE} = \sqrt{\frac{1}{N} \sum_{i=1}^{N} (\hat{I}(i) - I(i))^2} \tag{4.2}$$

where summation runs over all pixels i from the original image I and the interpolated image $\hat{I}$ [42].

To investigate the correlation between the PSNR value and the categorical variables for image and for method, a regression model for each upsampling rate was used.

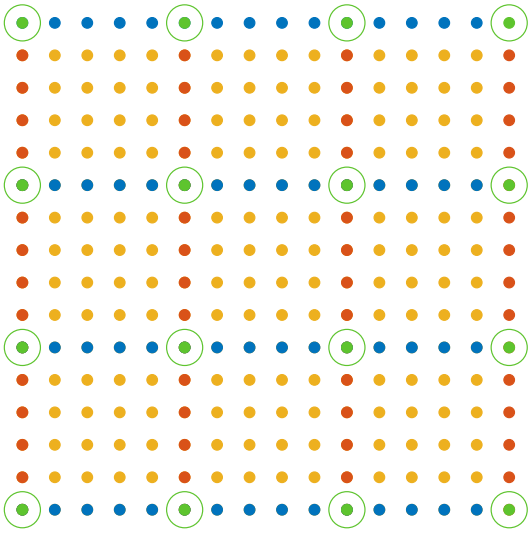

Figure 4.7: Set up for interpolation from grid lines. Sample points resampled along the scan lines for the horizontal scan are blue and red for sample points resampled along scan lines for the vertical scan. Green points are crossing points between the two scans and orange points are points in the fine grid for interpolation.

F-values from test of the model showed that the method was the main descriptor. Furthermore, significant difference between the methods was found. In order to test which methods performed best at a given upsampling rate, we performed pairwise tests of methods' performance.

The results are listed in table 4.1. The weighted method gave superior results for a broad range of upsampling rates.

4.3.2 Minimisation of artefacts

The idea behind combining the two orthogonal scans was to optimize the visual appearance of the en face image and to minimize artefacts. Common artefacts in OCT scans are shadowing and artefacts from patient movement (more detailed description in section 3.1.3). Artefacts and the acquisition technique may create a striped look of the en face image.

In paper B, we experienced that the striped look of the en face image was clearly minimized when combining two orthogonal scans. Figure 4.8 shows three interpolated en face images with the interpolation method called weighted (illustration from paper B). The interpolation method weighted performed best for broad range of upsampling rates including upsampling rate 5, which was the upsampling rate that matched the resolution of our EDI-OCT data. The first column shows the en face image from the horizontal scan,

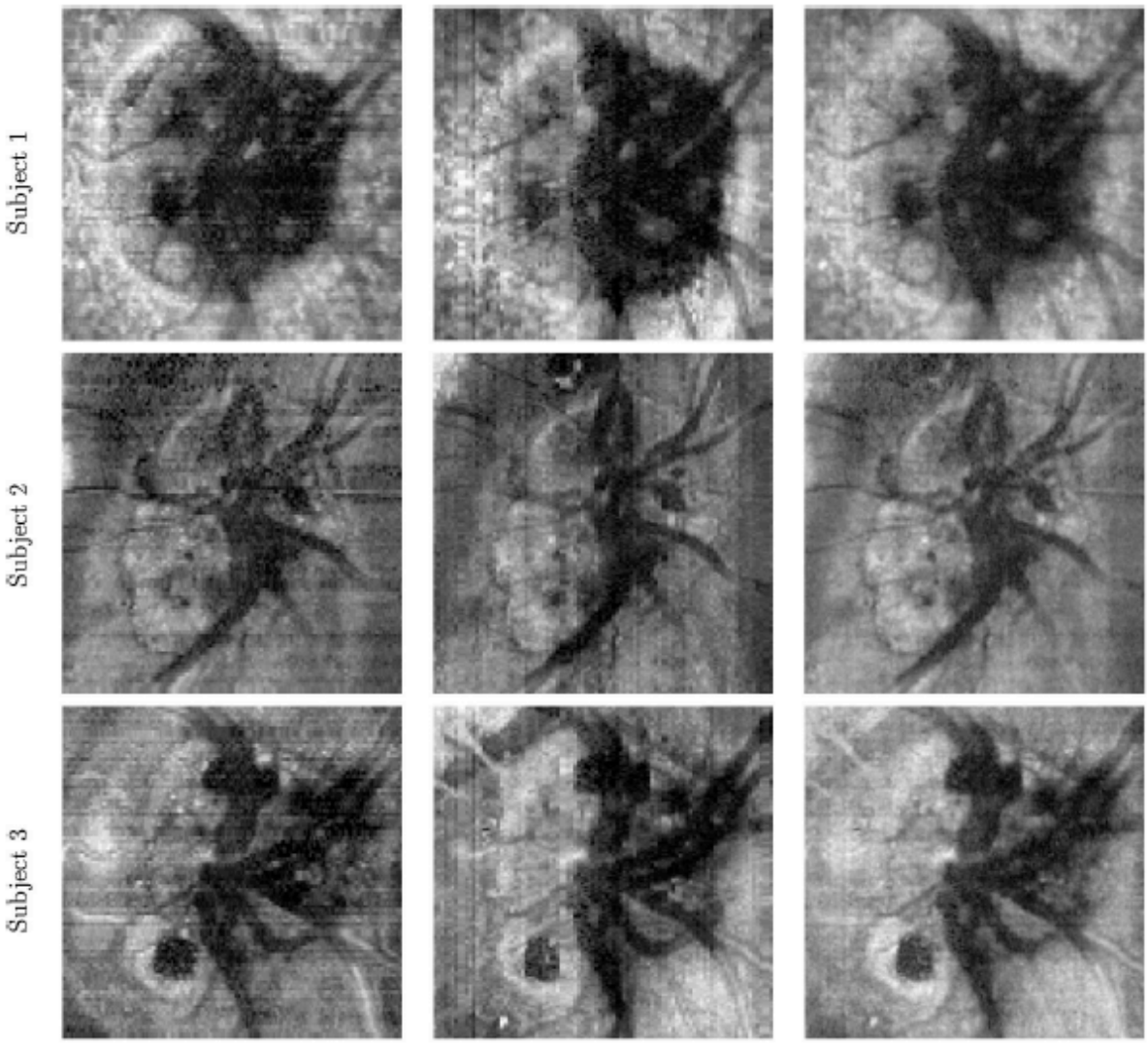

Figure 4.8: Interpolation of two orthogonal OCT en face images of the ONH (optic nerve head). The interpolation is performed on en face images of different places in depth in the ONH (optic nerve head). First column shows the en face images from the horizontal OCT scan. Second column shows the en face images from the vertical OCT scan and third column shows the en face images obtained from interpolation with the weighted interpolation method.

Table 4.1: Results from statistical analysis of interpolation performance for three methods at different upsampling rates for two types of data sets. The methods are linear (L), weighted (W) and transfinite (T), and upsampling rates are shown in intervals between 2 and 30. Number 1 indicates the method that performs best for a given upsampling rate, while 3 indicates the method that performs worst. The star indicates that no significant difference was found between the two methods for the given upsampling rate.

(a) Berkley data set

	2	3	4-5	6	7-14	15-20	21-30
L	3	3	3	2*	2	**1***	**1**
W	2	**1***	**1**	**1**	**1**	**1***	2
T	**1**	**1***	2	2*	3	3	3

(b) Fundoscopy data set

	2-3	4	5-6	7-8	9-19	20-22	23-30
L	3	3	3	2*	2	**1***	**1**
W	2	**1***	**1**	**1**	**1**	**1***	2
T	**1**	**1***	2	2*	3	3	3

the second column shows the en face image from the vertical scan and the third column shows the en face image obtained by interpolation from grid lines with the weighted interpolation method. In the interpolated images, anatomical structures are more well defined and the striped look is reduced. Furthermore, small blood vessels only visible in the image from one of the scan directions, became visible in the interpolated en face image.

The idea of minimising artefacts by combining two orthogonal OCT scans, arised from the problem concerning the missing lower boundary of ODD when imaged with SD-OCT. EDI-OCT imaged the lower boundary and deep located ODD more clearly, but artefacts were still present. Some artefacts are depended on scan direction.

The idea of minimizing artefact by merging two images is illustrated on Figure 4.9. A shadow artefact appears at a vessel marked by black lines. The artefact is present at the A-scans inside the red boxes. The A-scans for the horizontal scan shown as blue dots. The artefact is not present at any A-scans from the vertical scan shown as red dots. Information at the orange dots is interpolated. The information at the orange dots inside the blue box will both contain information from the surrounding A-scans from the vertical (e.g. point inside green box) and the horizontal scan. The shadow artefact is less present at the interpolated points inside the blue box compared to the A-scans inside the red boxes.

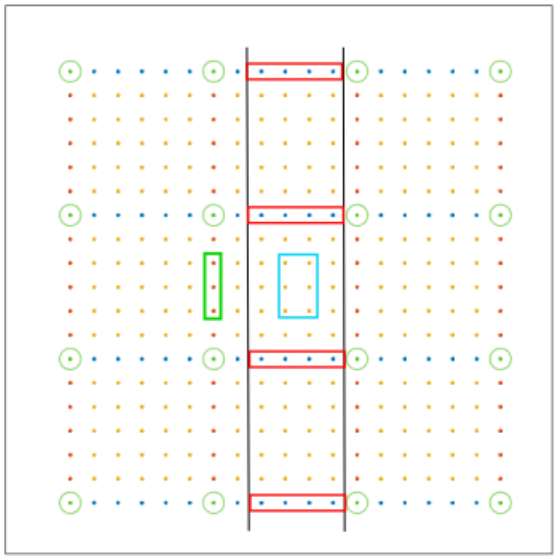

Figure 4.9: Minimisation of shadow artefact by combining two orthogonal scans. The blue dots are A-scans from a horizontal OCT scan and the red dots are A-scans from a vertical OCT scan. Green dots indicates crossing points between the two scans. A blood vessel illustrated by the black lines runs in the vertical direction causing shadow artefacts for the A-scans within the red boxes. The orange points are added by interpolation from the surrounding blue, red and green points. The orange points inside the light blue box will have less shadow artefact from the blood vessel.

4.4 Quantification of local vessel density - related to paper C

OCTA (OCT angiography) makes it possible to image the retinal and choroidal blood flow. To the best of our knowledge, a quantification of the ONH (optic nerve head) blood flow has only been sparsely described in literature. In the few published studies [43–45], a quantification of the blood flow is described by the vessel density, which is determined with build-in software e.g. AngioVue.

The local vessel density is of interest to investigate ODD complications and especially development of visual field defects. One major complication caused by ODD is compression. The compression may cause occlusion of blood vessels and lead to visual field defects. To quantify any compression, it is of interest to correlate the ODD volume in a local area with local vessel density and visual field defects.

In paper C *(Paper C - Determination of peripapillary vessel density and the influence of optic disc drusen from EDI-OCT and OCT angiography)*, we addressed the problem

of quantifying the local vessel density in OCTA scans of the ONH.

4.4.1 Vessel density heatmap

The vessel density is calculated from the en face angiogram. An en face angiogram is a 2D representation of the vessels imaged with OCTA. The en face angiogram is generated from a sub volume of the OCTA volume, containing the the vessels to be depict.

For the study behind paper C, the retinal vessel structure was of interest and the sub volume was defined by a slab from the ILM (inner limiting membrane) and 150 μm below. For the detection of the retinal layer, we used layered surface detection. Figure 3.4 illustrates the slab in an OCT B-scan, the corresponding OCTA B-scan and the en face angiogram.

The vessel structure in the en face angiogram was segmented with an adaptive thresholding algorithm [46]. The result of the segmentation is depended on the quality of the OCTA scan. Other published studies containing segmentation of vessel structure in the ONH use build-in tools in e.g. ImageJ [47] and Photoshop.

After segmentation, the segmented en face angiogram was skeletonized in order to express the vessels as one vessel disregarding of its size. From this, the vessel density was calculated within small areas to express the local vessel density. The resulting image was the vessel density heatmap. The method for calculating the vessel density heatmap was adapted from previous work published in [48].

4.4.2 Peripapillary area of the eye

It was of interest to calculate the vessel density within the peripapillary area of the eye. The peripapillary area is the area around the optic disc, also named the papil. The optic disc is round or slightly oval in shape, as described in section 2.1.1. The diameter of the optic disc can be measured in a B-scan as the opening of Bruch's membrane as illustrated on Figure 2.2. The optic disc can also be seen on a fundoscopy image.

In paper C, the optic disc was segmented in order to define the peripapillary area. We use a projection image, which is similar to a fundoscopy image. The projection image is generated by summing each column in the axial direction (depth) of the OCT volume. To generate an image for segmentation, we perform a radial sampling of part of the projection image. The optic disc is segmented with layered surface detection (section 4.2.3). The segmentation is described in more details in paper C.

The peripapillary area is limited by a outer circle with a diameter of 3.46 mm placed in the center of the optic disc. The peripapillary area is subdivided into six sections, which are nasal (N), nasal inferior (NI), temporal inferior (TI), temporal (T), temporal superior (TS) and nasal superior (NS). These sections relate to areas of the visual field and the division of the peripapillary area is known as a Garway-Heath map [49].

Figure 4.10 illustrates the peripapillary area. On Figure 4.10(a) shows the segmented optic disc (papil) on the projection image. Figure 4.10(b) shows the Garway-Heath map

on an en face angiogram. The peripapillary area is the area between the outer circle with diameter of 3.46 mm and the circle fitted to the optic disc.

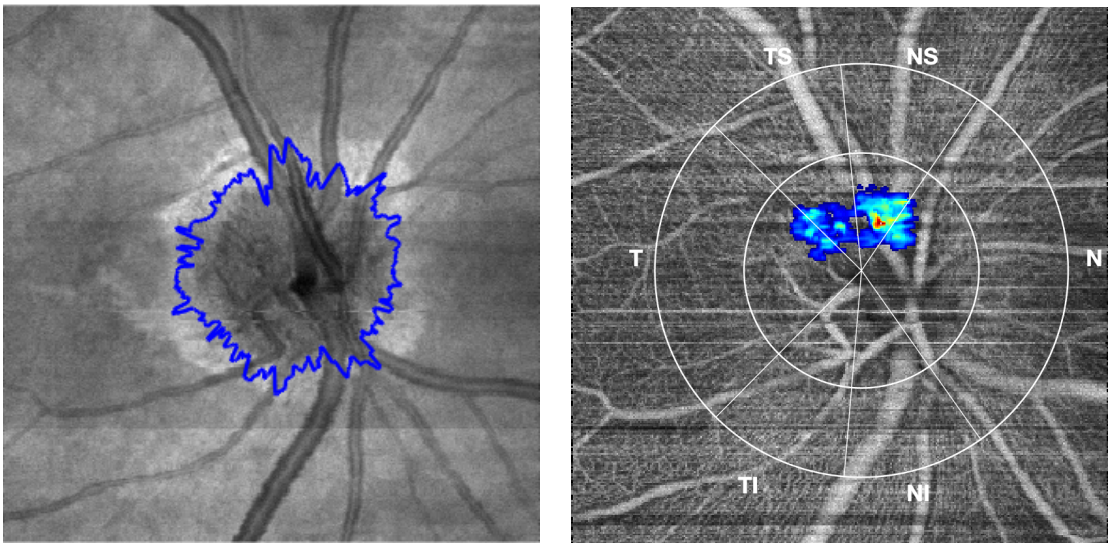

(a) (b)

Figure 4.10: Illustration of the peripapillary area divided into six sections known as a Garway-Heath map. On (a) projection image with the segmented optic disc marked with a blue line. On (b) the en face angiogram with a Garway-Heath map fitted to the segmented optic disc. The peripapillary area is the area between the inner circle fitted to the segmented optic disc and the outer circle with a diameter of 3.46 mm. The six sections of the peripapillary area are named nasal (N), nasal inferior (NI), temporal inferior (TI), temporal (T), temporal superior (TS) and nasal superior (NS) and are marked with capital letters. Colored structures are ODD, here color coded as a height map to express their volume in 2D.

4.5 Image registration - related to paper C

Image registration is the process of geometrically align two images of the same object. The two images being registered are named the source image and the reference image. Imagine an anatomical structure placed at the coordinate (x, y) in the source image and at coordinate (x', y') in the reference image. The aim of the registration is to transform the source image such that the transformed source image has the anatomical structure at coordinate (x', y').

Image registration is widely used in medical image analysis. It can be used for detecting changes over time by registering a scan and a follow up scan acquired with the same modality. Registration of images of the same object acquired with different modalities can be used to combine different type of information e.g. anatomical and functional information.

For finding the best transformation, different registration methods exist. In paper C (*Determination of peripapillary vessel density and the influence of optic disc drusen from EDI-OCT and OCT angiography*), we used translation based on a manual placed landmarks for pre alignment and afterwards an intensity-based affine registration.

4.5.1 Registration between OCT and OCTA

A registration between OCT and OCTA images enables to combine the anatomic location of ODD from the OCT scan with the functional information about blood flow from the OCTA scan. In principle, this registration is of images from two different modalities. However, the information in OCTA images comes from acquisition of multiple OCT B-scans. With access to the structural B-scans behind the OCTA scan, the registration was performed between two OCT scans. The found transformation was then applied to the OCTA scan.

The registration was performed between 2D projection images generated from the scan volumes by summing all voxels in depth (axial direction).

Before the registration, we needed to resample the two images on the same grid to make pixels square. We addressed this problem both in paper B *(Paper B - Linear, Transfinite and Weighted Method for Interpolation from Grid Lines Applied to OCT Images)* and paper C.

In paper B, the OCT scans were acquired orthogonal to each other, while in paper C, the scans were acquired in the same scan direction. Figure 4.11 shows the two set-ups. The first row shows the grid for the registration between two orthogonal scans addressed in paper B and the grid used for resampling before registration. The second row shows the grid for the registration between OCT and OCTA scans addressed in paper C and the grid used for resampling before registration.

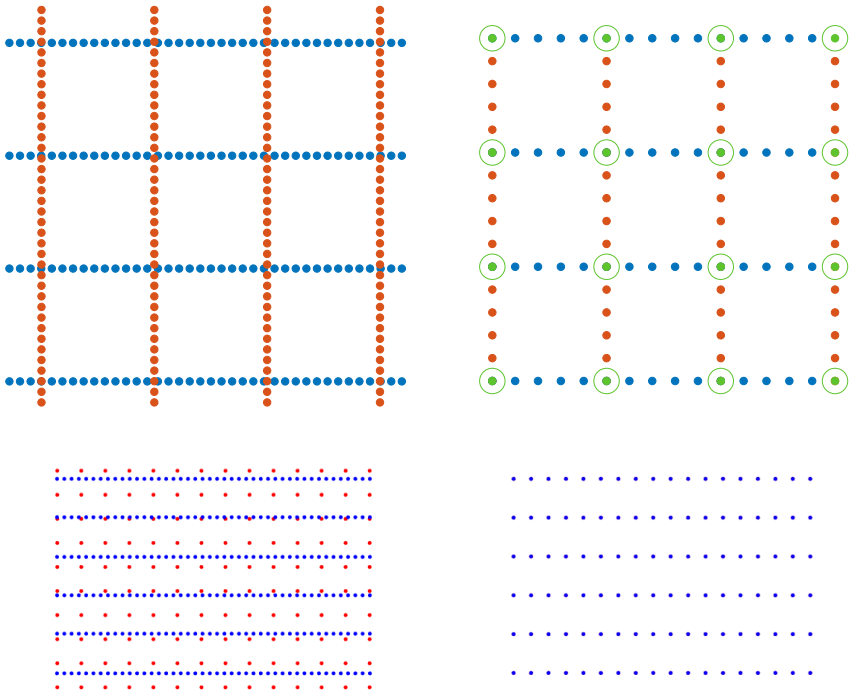

Figure 4.11: Resampling before registration. Illustrations in first row show set up for registration of orthogonal scan. Blue dots are sample points in the horizontal scan, while red dots are sample pints in the vertical scan. Grid in upper left corner is the original grid. Grid in the upper right corner is the grid used for resampling before registration. Illustrations in second row show set up for registration between scans acquired in same scan direction, but with different scan protocols. The grid at the lower left corner is the orignal grid before registration. Here, blue dots are sample points from OCT scan, while red dots are sample points in OCTA scan. The grid for resampling before registration is shown in the lower right corner. Here blue dots are point for resampling for both OCT and OCTA scan.

4.5.2 Translation for pre alignment

A landmark is a (x, y) point in the image that is manually placed in both the reference and the source image. Landmarks can be used to guide registration or for pre alignment of the images before registration. They should be placed with pairwise correspondence in the two images. The placement is based on an anatomical location, geometry or some feature in the image. Having a set of landmarks, a translation of the point in the source image to match the point in the reference image can be calculated as

$$\begin{aligned} \Delta_x &= x_{reference} - x_{source} \\ \Delta_y &= y_{reference} - y_{source} \end{aligned} \tag{4.3}$$

The translation works as a pre alignment of the images before registration. Pre alignment is a good idea before performing a registration to make sure that points assumed to match are close to each other. For OCT images, it is necessary to pre align when only a part of the image is overlapping with a region in the other image. This is often the case for OCT images because of different scan protocols and scan areas of different size.

4.5.3 Intensity based affine registration

Intensity based registration estimates the transformation of the source image to match the reference image based on intensity values. We use an affine transformation that includes rotation, translation and scaling. For quantification of the alignment between the source and the reference image, the mean square difference is used as similarity measure. The transformation is optimized using a optimization algorithm based on the similarity measure.

4.6 Research questions sum up

Can EDI-OCT be used to quantify ODD as a 3D structure and how can the anatomical location of ODD be measured?

(Paper A - Quantitatively Measured Anatomic Location and Volume of Optic Disc Drusen: An Enhanced Depth Imaging Optical Coherence Tomography Study)

In Paper A, we addressed the problem of quantifying ODD (Optic Disc Drusen) as a 3D structure. The lower boundary of ODD was imaged more clearly with the new technique of EDI-OCT. Manual segmentation of 37 ODD patients created a unique data set for visualising of ODD in 3D and measure ODD volume. The vertical anatomical location of each individual ODD was measured as the vertical distance from ODD center of mass to a reference surface. The reference surface was defined from Bruch's membrane, found with layered surface detection. The technique EDI-OCT was found to be a turning point for visualising and diagnosing ODD. The study and results presented in Paper A have contributed to new knowledge about ODD and imaging of them. The paper has been cited 16 times in other journal papers regarding optic disc drusen.

How can information from two orthogonal EDI-OCT be combined to improve the visual appearance of the an en face image? Which interpolation method should be used for solving the problem of interpolation from grid lines?

(Paper B - Linear, Transfinite and Weighted Method for Interpolation from Grid Lines Applied to OCT Images)

In Paper B, we addressed the problem of combining two orthogonal EDI-OCT scans with the aim of improving visual appearance of the en face image. A combination of orthogonal scans was simplified to a 2D problem of interpolation from grid lines. We aimed at preserving information along grid lines (scan lines) and this interpolation problem in context of image interpolation had not been addressed in literature. We applied three different interpolation methods, linear, transfinite and weighted method, to two data sets. The data sets had been resampled to create a ground truth for evaluation of the interpolation methods. Statistical tests of the performance score revealed which interpolation method, that performed best at a given upsampling rate. The best performing method for a broad range of upsampling rates was the weighted method. We applied the method to EDI-OCT scans to evaluate the improvement of the visual appearance of the en face image. We saw that stripes were reduced in the en face image

and anatomical structures appeared more clearly. The combining of two orthogonal EDI-OCT scans improved the visual appearance, but a need for evaluating the result quantitatively exists.

How can the local vessel density be expressed from OCTA scans? Is it possible to quantify compression of the vascular system from large ODD?

(Paper C - Determination of peripapillary vessel density and the influence of optic disc drusen from EDI-OCT and OCT angiography)

In Paper C, we addressed the problem of expressing the local vessel density from OCTA scans. The aim of the study was to develop a method for determine the local vessel density in the peripapillary sections of a Garway-Heath map. The method contains a calculation of en face angiogram and an image (heatmap) expressing the local density from the en face angiogram. The heatmap contains information about local vessel density in all areas of the scan area. We found the peripapillary sections of the optic nerve with an segmentation of optic disc and defining the Garway-Heath map.

Furthermore, our aim was to quantify a possible compression of the vascular system. This was expressed as a decrease in the local vessel density. With the unique data set containing ODD in 3D from Paper A, we combined information about ODD volume with the found local vessel density in the peripapillary sections.

The combination of information was obtained with image registration between the EDI-OCT and the OCTA scan. The results showed a clear tendency of lower vessel density in sections with large ODD area (en face view) and volume. The results indicated that the method can be used for quantifying compression of the vascular system from large ODD. However, the results were obtained from five ODD patients and five healthy subjects. A larger study including more patients and healthy subjects is needed to quantify the results statistically. This large clinical study, using the developed method, is in progress for submission.

CHAPTER 5

Conclusion

In this thesis we contributed with new insight about optic disc drusen, that would not have been possible to achieve without the use of 3D image analysis.

We addressed the problem of quantifying optic disc drusen in 3D with the new technique EDI-OCT. We were the first to publish a study containing new knowledge of optic disc drusen volumen and anatomical location and how to obtain these measurements with the use of image analysis.

We addressed the problem of optimizing the visual appearance of en face images by combining orthogonal OCT scans. We proposed a novel interpolation method, the weighted method, for solving interpolation from grid lines. The weighted method was able to preserve the information along grid lines and use the stability of linear interpolation further away from the grid lines in order to prevent overshooting. Our interpolation method was thoroughly evaluated on different type of image data and compared with two other interpolation methods. The weighted method performed superior for a broad range of upsampling rates including the upsampling rate that matched the resolution of OCT scans. We applied the method to OCT data and achieved visually good results including minimisation of artefacts and more clear visual appearance of anatomic structures.

Furthermore, we tried to quantify complications caused by ODD with the use of OCTA scans. We used our 3D quantification of ODD to investigate the impact of ODD volume in regard to compression of the vascular system. We developed a method for expressing the local vessel density in the optic nerve head. The local vessel density was correlated with the anatomical location and volume of ODD. The results showed a clear tendency that large ODD causes a decrease in the local vessel density in the corresponding section of the peripapillary area of which the ODD was located.

APPENDIX A

Paper A

Title

Quantitatively Measured Anatomic Location and Volume of Optic Disc Drusen: An Enhanced Depth Imaging Optical Coherence Tomography Study

Authors

Lasse Malmqvist, Anne-Sofie Wessel Lindberg, Vedrana Andersen Dahl, Thomas Martini Jørgensen and Steffen Hamann.

Year

2017

Proceedings

Investigative Ophthalmology & Visual Science, 2017, Vol. 58.

Publication history

Submitted February 2, 2017. Accepted March 29, 2017.

Quantitatively Measured Anatomic Location and Volume of Optic Disc Drusen: An Enhanced Depth Imaging Optical Coherence Tomography Study

Lasse Malmqvist,[1] Anne-Sofie Wessel Lindberg,[2] Vedrana Andersen Dahl,[2] Thomas Martini Jørgensen,[2] and Steffen Hamann[1]

[1]Department of Ophthalmology, Rigshospitalet, University of Copenhagen, Glostrup, Denmark
[2]Department of Applied Mathematics and Computer Science, Technical University of Denmark, Lyngby, Denmark

Correspondence: Lasse Malmqvist, Department of Ophthalmology, Rigshospitalet, Nordre Ringvej 57, 2600 Glostrup, Denmark; lasse.malmqvist.larsen.01@regionh.dk.

Submitted: February 2, 2017
Accepted: March 29, 2017

Citation: Malmqvist L, Lindberg A-SW, Dahl VA, Jørgensen TM, Hamann S. Quantitatively measured anatomic location and volume of optic disc drusen: an enhanced depth imaging optical coherence tomography study. *Invest Ophthalmol Vis Sci*. 2017;58:2491–2497. DOI:10.1167/iovs.17-21608

Purpose. Optic disc drusen (ODD) are found in up to 2.4% of the population and are known to cause visual field defects. The purpose of the current study was to investigate how quantitatively estimated volume and anatomic location of ODD influence optic nerve function.

Methods. Anatomic location, volume of ODD, and peripapillary retinal nerve fiber layer and macular ganglion cell layer thickness were assessed in 37 ODD patients using enhanced depth imaging optical coherence tomography. Volume of ODD was calculated by manual segmentation of ODD in 97 B-scans per eye. Anatomic characteristics were compared with optic nerve function using automated perimetric mean deviation (MD) and multifocal visual evoked potentials.

Results. Increased age ($P = 0.015$); larger ODD volume ($P = 0.002$); and more superficial anatomic ODD location ($P = 0.007$) were found in patients with ODD visible by ophthalmoscopy compared to patients with buried ODD. In a multivariate analysis, a worsening of MD was significantly associated with larger ODD volume ($P < 0.0001$). No association was found between MD and weighted anatomic location, age, and visibility by ophthalmoscopy. Decreased ganglion cell layer thickness was significantly associated with worse MD ($P = 0.025$) and had a higher effect on MD when compared to retinal nerve fiber layer thickness.

Conclusions. Large ODD volume is associated with optic nerve dysfunction. The worse visual field defects associated with visible ODD should only be ascribed to larger ODD volume and not to a more superficial anatomic ODD location.

Keywords: optic disc drusen, optic nerve head drusen, 3D segmentation, visual field defects

Optic disc drusen (ODD) are bodies of extruded axonal material located in the optic nerve head.[1] They are found in up to 2.4% of the population[2] and are known to cause visual field defects,[3,4] and even complete vision loss due to complications.[5,6]

Diagnosis and classification of ODD has historically been based mainly on ophthalmoscopy. With the development of new imaging techniques, the diagnosis by ophthalmoscopy is today normally confirmed by B-scan ultrasound or optical coherence tomography (OCT).[7] However, the most frequently used classification of ODD is still based on ophthalmoscopy using none of the emerging imaging techniques. In the classification, ODD that are visible on ophthalmoscopy are termed superficial while ODD only visible by B-scan ultrasound or OCT are termed buried. Several studies have found significantly larger decreases in retinal nerve fiber layer (RNFL) thickness and automated perimetric mean deviation (MD) in patients with visible ODD when compared to patients with buried ODD.[8–11] The morphologic causes for these findings are unclear, as the ODD visibility on ophthalmoscopy might be dependent on several factors such as age, ODD volume, anatomic location of ODD, and optic nerve head anatomy.

The introduction of enhanced depth imaging OCT (EDI-OCT) has made it possible to quantify ODD anatomically.[12,13] The technique thereby enables us to decide to which degree ODD volume and anatomic location influence optic nerve function, which could be of importance for the pathophysiologic understanding of the condition.

A quantitative measure of ODD volume has only been described in a single case series,[12] while a quantitative measure of ODD location in the optic nerve head, to the best of our knowledge, never has been described. In this study, we developed a new method based on a three-dimensional (3D) analysis of the optic nerve head and semiautomatic graph-based detection of Bruch's membrane to calculate the height difference from the center of ODD mass to the defined reference surface.

The aim of this study was to investigate how volume and anatomic location of ODD influence optic nerve function using automated perimetry and multifocal visual evoked potentials (mfVEP). By including ODD visibility by ophthalmoscopy in the analysis, we assessed whether our quantitative measures were better predictors of optic nerve dysfunction than the qualitative often used classification using ODD visibility. Furthermore, we

investigated whether RNFL and macular ganglion cell layer (GCL) thickness work as anatomic correlates to optic nerve dysfunction in ODD patients.

Patients and Methods

The study was a prospective observational study approved by the scientific ethics committee of the Capital Region, Denmark (H-4-2013-040).

Patient Selection

Patients diagnosed with ODD from January 1, 2009, to January 1, 2016, were asked to participate in the study. All patients were seen at the Department of Ophthalmology at Rigshospitalet-Glostrup, Denmark. The patient exclusion criteria were best corrected visual acuity (BCVA) >logMAR 0.2, age <18 years, and presence of systemic disease that could affect optic nerve function. Exclusion criteria for individual eyes were localized eye or optic nerve disease other than ODD (e.g., optic neuritis, glaucoma, etc.) or ODD complications (e.g., drusen-associated anterior ischemic optic neuropathy, central retinal artery, vein occlusion, etc.) that could affect optic nerve function.

Informed consent was obtained from the subjects after explanation of the nature and possible consequences of the study. All procedures adhered to the tenets of Declaration of Helsinki.

Data Acquisition

All examinations were performed by a single examiner (LM). All included participants were asked about medication use as well as ophthalmic and medical history. Best corrected visual acuity was determined using Early Treatment Diabetic Retinopathy Study (ETDRS) charts (4-meter original series; Precision-Vision, La Salle, IL, USA). Patients were examined using slit lamp biomicroscopy and intraocular pressure was measured by applanation tonometry. Spectral domain EDI-OCT (Spectralis HRA+OCT; Heidelberg Engineering, Heidelberg, Germany) was performed using the following protocol: (1) dense optic nerve head scan for identification and quantification of ODD with EDI-OCT in both vertical and horizontal directions with 30 μm between each B-scan (97 scans), averaging 30 B-scans; (2) peripapillary evaluation of RNFL thickness with a 12° circumferential scan; and (3) macula overview in vertical direction with 240 μm between each B-scan for evaluation of macular GCL thickness. All scans were performed in high resolution with averaging of B-scans using the built-in eye tracking feature. Patients were dilated with 2.5% phenylephrine before OCT acquisition.

Recording and analysis of mfVEP data was performed as previously described.[14] Briefly, patients were stimulated in a viewing distance of 30 cm to a screen (22-inch, high-resolution LCD display, 90% brightness and 65% contrast; Hitachi, Ltd., Tokyo, Japan) containing a cortically scaled 56-segment dartboard pattern with 16 checks alternating between black and white in each segment according to a pseudorandom sequence. The test was performed nondilated with optimal refraction. The central 1° of the screen contained an interactive fixation area. We recorded the mfVEP using a commercial system (VisionSearch1; VisionSearch, Sydney, Australia) in a vertical (a positive electrode 2.5 cm above inion and a negative reference electrode 4.5 cm below inion) and horizontal (a positive electrode 4 cm left of inion and a negative reference electrode 4 cm right of the inion) channel. The data sampling rate was 600 Hz with a recording length of 832 ms. We obtained the mfVEP responses by correlating visual stimuli with recorded electrical potentials.

Visual field analysis was obtained using automated perimetry (Octopus, Haag-Streit, Switzerland) with a 30-2 test pattern.

Data Analysis

Specialized software (Heidelberg Eye Explorer, version 1.9.10.0; Heidelberg Engineering) was used to assess all OCT parameters. Integrated automated segmentation software was used in all scans and manually verified and adjusted. Macular GCL was measured in a circular area of 3 to 6 mm from the foveola. Global peripapillary RNFL thickness was measured centering the scan at the optic disc. Scleral canal size was manually measured as the mean of the largest vertical and horizontal opening of Bruch's membrane. The dense optic nerve head scan was exported from the integrated software and was manually analyzed using a medical image segmentation tool (ITK-Snap; ITK-Snap ver. 3.2.0, www.itksnap.org; in the public domain).[15] The volume of ODD was calculated by manual segmentation of ODD in 97 B-scans per eye. Each ODD was localized and individually segmented in each B-scan to calculate ODD volumes. The definition of ODD using OCT was based on previous studies[12,16–19] and defined as hyporeflective structures with a full or partial hyperreflective margin. See Supplementary Movie S1 for a 3D view of a segmented optic nerve head. To quantify the vertical anatomic location of each ODD, an automated graph-based segmentation of Bruch's membrane[20] at the margin in each B-scan was performed with computing software (MATLAB; The MathWorks, Inc., Natick, MA, USA). A reference surface relative to Bruch's membrane was defined from these landmarks (Fig. 1). The height difference from the center of mass of each ODD to the reference surface was thereafter calculated with negative values referring to localization above the reference surface and positive values referring to localization below the reference surface. The anatomic vertical location of each ODD was multiplied by the volume fraction of the same ODD relative to the total ODD volume in each patient to quantify the anatomic vertical center of weighted ODD mass. This means that a large deep ODD would have a greater impact on the vertical anatomic center of weighted ODD mass than a small superficial ODD, and thereby result in a deeper overall localization. On the other hand, if the superficial ODD was larger, the weighted center of mass would move toward a more superficial localization.

The agreement of ODD volume was assessed in 10 randomly selected patients with intraobserver variability using Bland-Altman plots. Intraobserver agreement in ODD volume assessment revealed a mean difference between measurements of 0.027 mm^3 (SD ± 0.035), representing 9% of the mean ODD volume. Bland-Altman plots showed acceptable variability, no trend and limits of agreement between –0.062 and 0.099 mm^3.

Responses of MfVEP were obtained by correlating visual stimuli with recorded electrical potentials using integrated software (Terra, version 1.6; VisionSearch, Sydney, Australia). Peak-to-peak (P2P) amplitude and monocular latency (second peak) was obtained using the integrated software after manual validation of the responses. Signal-to-noise ratio (SNR) amplitude was calculated in a computing environment (The MathWorks, Inc.) as described in previous work.[14]

Statistical Analysis

Statistical analyses were performed using commercial software (SAS, version 9.1; SAS Institute, Cary, NC, USA). To avoid statistical bias, only one eye was included for each patient. The

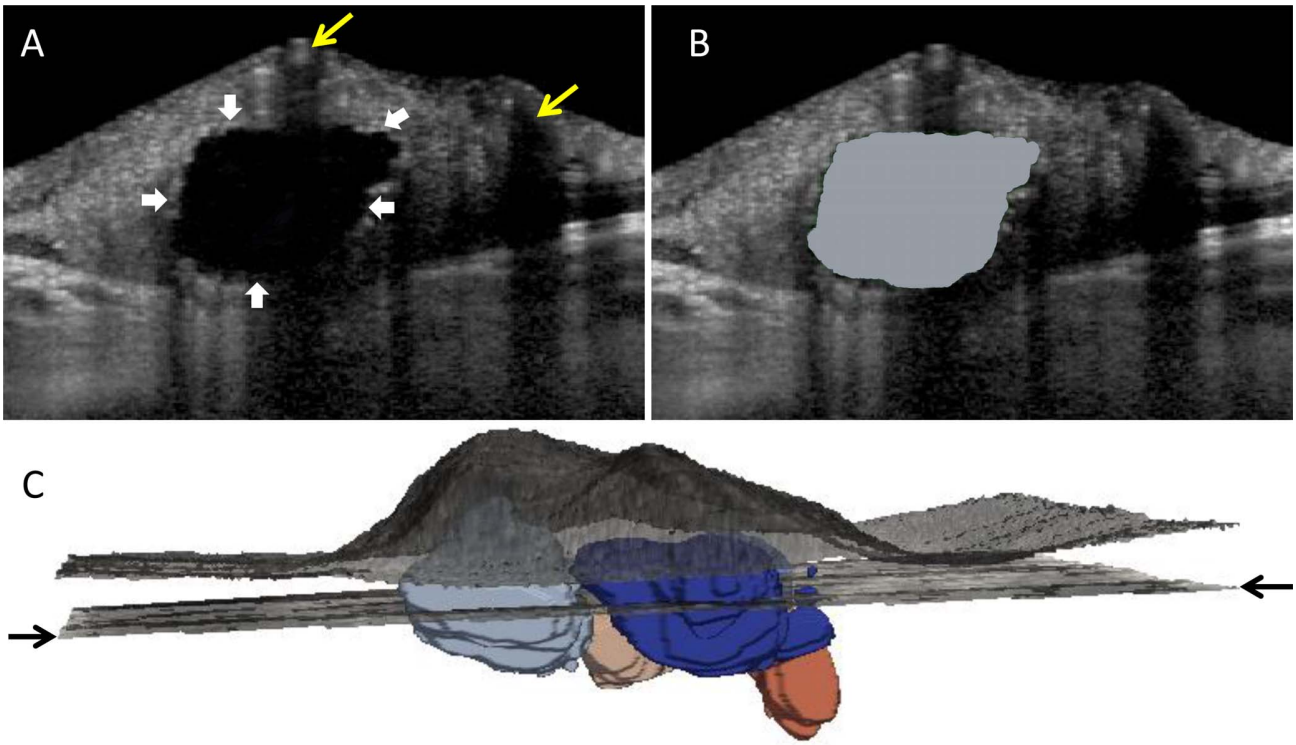

FIGURE 1. Visualization of the process going from EDI-OCT scans to 3D volume of ODD. (**A**) Single EDI-OCT B-scan with a prominent ODD (*white arrowheads*). *Yellow arrows* represent vessels. (**B**) We performed 2D segmentation of ODD (*painted area*) in each B-scan. (**C**) A total of 97 segmented B-scans created the final 3D segmentation. To quantify the vertical anatomic location of each ODD a reference surface relative to Bruch's membrane was defined using an automated graph based segmentation of Bruch's membrane (*black arrow*). Four individual ODD are seen in different colors.

eye with worst MD on automated perimetry was used in patients with bilateral ODD.

Mean and standard deviations or median and interquartile ranges (skewed distributions) were reported for continuous variables. Student's *t*-test or Wilcoxon signed-rank test (skewed distribution) was used to compare patients with visible and buried ODD. We used χ^2 or Fisher's exact tests (expected count <5) for categorical data.

The assumptions of linearity, homoscedasticity, and normal distribution of residuals were tested when performing multiple regressions. The contribution of each predictor in the multiple regression analysis was found by assessing standardized parameter estimates (the change in *Y*, measured in units of its standard deviation, associated with a 1 standard deviation change in *X*). The assumptions of linearity, homoscedasticity, related pairs, and normality of variables were tested when performing correlation analysis. Adjustment for multiple testing in the correlation analyses was performed using the Holm-Bonferroni method. The predetermined level of statistical significance for the comparisons was $P \leq 0.05$.

RESULTS

We included 37 patients (30 women and 7 men) in this study. All included patients were Caucasian. Bilateral ODD were found in 95% of the patients. All eyes with ODD had one or more hyporeflective structures with a full or partial hyperreflective margin using OCT. Differences in clinical, mfVEP, and EDI-OCT findings were compared between patients with visible (visible by ophthalmoscopy) and buried (only visible by EDI-OCT) ODD (Table 1). Patient with buried ODD were significantly younger (median age: 21 years) than patients with visible ODD (median age: 33 years; $P = 0.015$). Significantly thinner peripapillary RNFL thickness and macular GCL thickness (3–6 mm from fovea) were found in patients with visible ODD ($P < 0.001$, $P = 0.002$). A tendency toward larger scleral canal size in patients with visible ODD was found ($P = 0.05$). A worse MD was found in patients with visible ODD (−4.3 dB) when compared to patients with buried ODD (−1.9 dB; $P = 0.025$). The quantitative measure of anatomic location was significantly different between the two groups with the center of weighted ODD mass being 172 µm below the reference level in patients with visible ODD and 306 µm below the reference level in patients with buried ODD ($P = 0.046$). Volume of ODD was larger in patients with visible ODD (0.29 mm^3) than in patients with buried ODD (0.01 mm^3; $P = 0.002$).

A multiple linear regression was calculated to predict MD based on ODD volume, visibility by ophthalmoscopy, anatomic ODD location, and age. A significant regression equation was found ($R^2 = 0.52$, $P < 0.0001$). Larger ODD volume was associated with worse MD ($P < 0.0001$). For every 1 mm^3 increase in ODD volume, the MD decreased by 18.1 dB (CI 95% −25.6 to −10.7 dB). Anatomic ODD location, age, and visibility by ophthalmoscopy were not found significantly associated with MD when adjusted for the other variables. When looking at standardized parameter estimates, ODD volume had a higher effect on MD when compared to weighted ODD location. Figure 2 illustrates the ODD segmentation, en face overview, and corresponding visual field and RNFL thickness map in three selected patients.

Another multiple linear regression was performed to estimate the relative effect of RNFL and macular GCL thickness on MD. A significant regression equation was found ($R^2 = 0.58$,

Table 1. Differences in Clinical, mfVEP, and EDI-OCT Findings in Patients With Visible and Buried ODD

Variable	Visible ODD ($n = 32$)	Buried ODD ($n = 5$)	*P* Values
Female sex, *n*	26	4	1.0*
Age, y	33 (26)	21 (1)	0.015†
Refractive error, D	−0.75 ± 3.1	0.95 ± 2.8	0.28‡
IOP, mm Hg (applanation tonometry)	13 (3)	13 (2)	0.98†
BCVA, (ETDRS, letters)	88 (6)	87 (1)	0.79†
Ishihara	16/16	16/16	0.44†
RAPD	8	0	0.56*
MD, dB	−4.5 (10.3)	-1.9 (2.6)	0.025†
Peak-to-peak mfVEP amplitude, nV	122 ± 55	131 ± 48	0.74‡
Signal-to-noise ratio mfVEP amplitude	3.8 ± 1.1	3.3 ± 0.6	0.29‡
Second peak mfVEP latency, ms	154±9	153 ± 2	0.81‡
Peripapillary RNFL thickness, μm	66.6 ± 20	101.4 ± 6.8	<0.001‡
Retinal macular thickness, μm	277.8 ± 20.7	279.2 ± 10.6	0.83‡
Macular GCL thickness 3–6 mm, μm	29.5 ± 5.8	36.4 ± 3.0	0.002‡
Scleral canal diameter, μm	1631 (230)	1477 (114)	0.05†
ODD volume, mm^3	0.29 (0.41)	0.01 (0.02)	0.002†
Mean anatomic location below reference level, μm	49 (211)	295 (114)	0.007†

D, diopter; IOP, intraocular pressure; RAPD, relative afferent pupillary defect.
* χ^2 test.
† Wilcoxon rank sum test.
‡ Student's *t*-test.

$P < 0.0001$). Worse MD was significantly associated only with GCL thickness ($P = 0.025$) when adjusted for the other variable. Mean deviation increased by 0.65 dB (CI 95% 0.08–1.2 dB) for every 1 μm increase in GCL thickness. When looking at standardized parameter estimates, GCL thickness had a higher effect on MD when compared to RNFL thickness.

Table 2 summarizes the correlation between anatomic and functional markers of optic nerve dysfunction. Macular GCL thickness had the highest degree of correlation when compared to MD ($\rho = 0.76$, $P < 0.0001$), while macular GCL thickness and peripapillary RNFL thickness were comparable when looking at mfVEP parameters. The unadjusted correlation coefficient for the correlation between ODD volume and MD was −0.66 (Fig. 3).

Discussion

Our study is, to the best of our knowledge, the first to quantitatively assess both the ODD volume and anatomic location of ODD. Using visibility by ophthalmoscopy to classify ODD in superficial or buried might be obsolete due to technical advances in imaging techniques. We therefore calculated ODD volume and anatomic location quantitatively and applied it in a multivariate model for a better understanding of their relative contribution to optic nerve dysfunction.

We found that a larger ODD volume resulted in worse MD when adjusted for age, visibility by slit lamp, and anatomic location. Other studies have quantitatively assessed ODD size,[11,12] and similar results were found in a recent case-series including five patients,[12] where an excellent correlation between ODD volume and MD using automated perimetry was found. We suspect the increasing optic nerve dysfunction caused by larger ODD volume might be a result of either direct compression of adjacent ganglion cell axons, leading to ganglion cell death or secondary to compromised vascular flow.[21]

No association between weighted anatomic ODD location and MD was found in the current study. This is interesting as several studies have found worse MD in patients with ophthalmoscopically visible ODD.[8,22,23] Other studies have further found more abnormal visual fields in patients with visible ODD when compared to patients with buried ODD.[24–26] The results from this study suggest that age, ODD volume, and ODD location all contribute to ODD visibility. This means that equating ODD visibility on ophthalmoscopy with superficial anatomic ODD location only, incorrectly leads one to believe that there is an association between superficial anatomic ODD location and worse MD. Our findings suggest that solely larger ODD volume, and not a more superficial ODD location, results in higher degrees of visual field defects.

Based on our finding that visibility by ophthalmoscopy did not have an effect on MD when adjusted for age, ODD volume and ODD location, we argue that the classification using ODD visibility by ophthalmoscopy is not ideal to estimate optic nerve dysfunction. Furthermore, the term "superficial", often used in the classification, is misleading as several factors, such as age and ODD volume, influence the visibility. In this regard, the term "visible" ODD might therefore be more appropriate to use than superficial ODD.

We found differences in age, MD, RNFL, and GCL thickness that are supported by several studies when using the classification of ODD as visible or buried.[8–11,23,27] Our results of the multivariate analysis suggest that GCL thickness is a better anatomic correlate to optic nerve dysfunction in ODD patients than RNFL thickness. While the macular GCL thickness has not been explored extensively in ODD literature, macular ganglion cell–inner plexiform layer thickness has proven to be a predictor of early glaucoma with the same sensitivity as RNFL thickness.[28,29] It has even been suggested that individually segmented GCL thickness could be a better predictor for the presence of preperimetric glaucoma than RNFL thickness.[30]

Conflicting results have been published about the role of scleral canal size in ODD etiology.[31–34] A larger scleral canal in patients with superficial ODD has been previously reported,[33,34] and in this study, the same tendency was found. In unpublished data (Malmqvist L, unpublished poster presentation, 2016), we have found smaller scleral canal in ODD children when compared to healthy children and we therefore suggest the finding of this study is due to a displacement of Bruch's membrane caused by distending ODD. This was originally proposed as an alternative explanation for similar findings in a study by Floyd et al.[34] Our proportion of patients

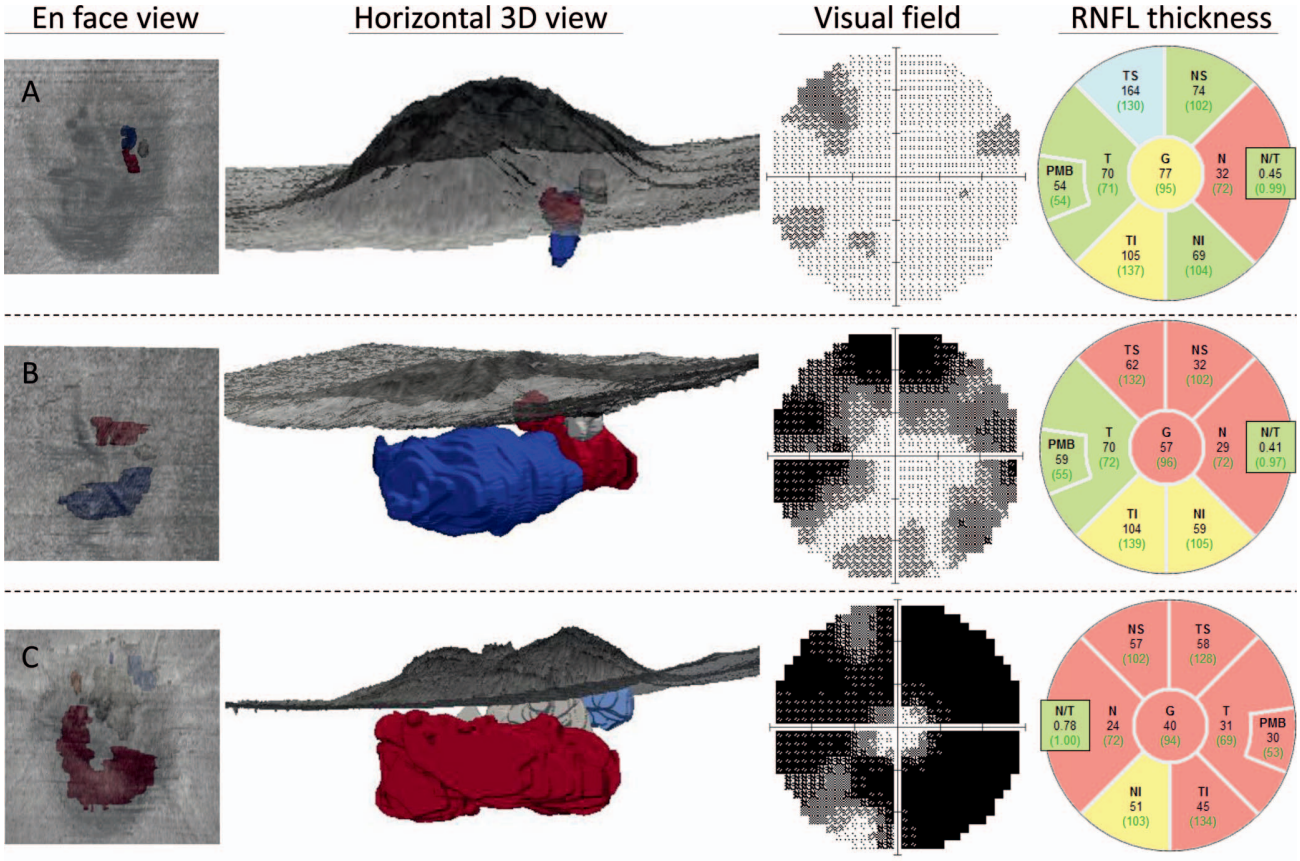

Figure 2. En face view and horizontal 3D view of optic nerve head and segmented ODD, as well as corresponding visual fields and RNFL thickness map in three different patients. Different colors symbolize the individual drusen. Colors in the RNFL thickness map indicate if the thickness in different regions is within or outside the statistical limits of normality: *green*, normal; *yellow*, borderline below normal limits; *red*, below normal limits; *blue*, borderline above normal limits. (**A**) Right eye of a patient with total ODD volume of 0.07 mm^3. Visual field testing revealed a near-normal mean deviation of −2.9 dB and global RNFL thickness was decreased to 77 µm. (**B**) Right eye of a patient with total ODD volume of 0.23 mm^3. Visual field testing revealed a mean deviation of −12.3 dB and global RNFL thickness was decreased to 57 µm. (**C**) Left eye of a patient with total ODD volume of 0.69 mm^3. Visual field testing revealed a mean deviation of −24.3 dB and global RNFL thickness was decreased to 40 µm.

with bilateral ODD (95%) is the highest reported in the literature.

Most studies have reported bilateral ODD in 62% to 76% of patients.[8,11,35,36] By using EDI-OCT in our study, we were able to diagnose eyes with small and deeply buried ODD overlooked by ophthalmoscopy, autofluorescence, B-scan ultrasound, and even conventional spectral-domain OCT. Based on these results, we propose that bilateral ODD are more common than previously believed.

Table 2. Correlation Coefficients for Correlations Between Anatomic and Functional Markers of Optic Nerve Dysfunction

Variable	Automated Perimetry MD	Multifocal Visual Evoked Potentials		
		P2P	SNR	Latency
ODD volume	−0.66*	−0.43	−0.22	0.28
RNFL thickness	0.72*	0.51*	0.43*	−0.48*
GCL thickness	0.76*	0.56*	0.48*	−0.48*

Pearson's correlation coefficient between anatomic and functional markers of optic nerve dysfunction.

* Holm-Bonferroni adjusted significant ($P < 0.05$). Latency was measured as second peak latency. Global RNFL thickness was measured peripapillary. Thickness of GCL was measured as the mean of a 3 to 6 mm ring around the fovea.

In this study, we included mfVEP amplitude and latency as an objective measure of optic nerve function as previous studies have found significantly decreased amplitude and latency delays in patients with optic disc drusen when compared to control subjects.[37,38] Hence an association between ODD volume and mfVEP parameters was expected. Parameters of mfVEP were significantly correlated with RNFL and GCL thickness, but not with ODD volume. That mfVEP amplitude was not correlated with ODD volume is likely a result of the high intersubject variability[14] and in this case, we assume that the variability was too high to describe the more subtle changes in optic nerve dysfunction when only comparing ODD patients.

The major limitation of the study was the use of multiple regression analysis with the limited amount of patients. By using the covariate "visibility by ophthalmoscopy," including only five eyes with buried ODD, the estimation was not strong. The fact that we, in multiple regression analyses, did not find an association between RNFL thickness and MD, can be ascribed to multicollinearity, as RNFL and GCL thickness were correlated. In this study, transverse magnification was not measured to account for the effect of optical magnification. However, the mean spherical equivalent refraction was not significantly different between patients with visible and buried ODD. In this study, we exclusively measured the volume of ODD defined as hyporeflective structures with a full or partial

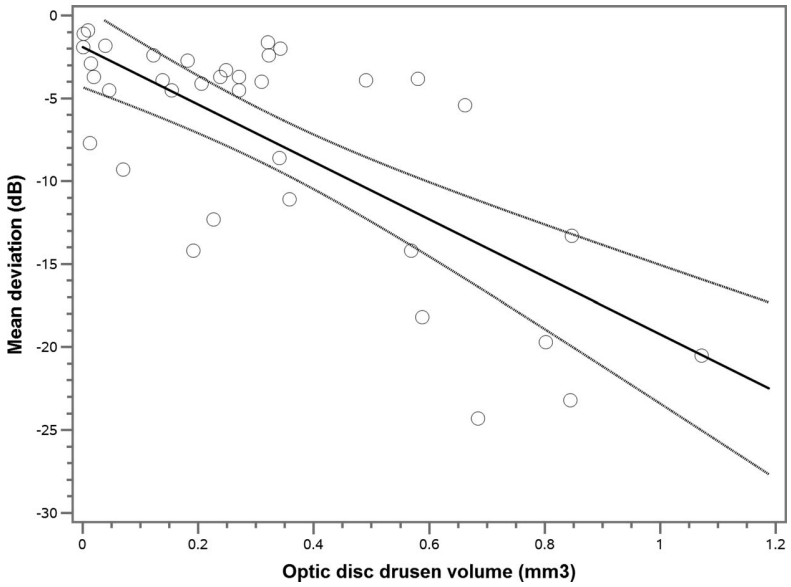

FIGURE 3. Unadjusted total ODD volume as a function of automated perimetric MD; $\rho = -0.66$. *Black line* represents regression line. *Gray line* represents 95% confidence limits.

hyperreflective margin. However, other studies have reported ODD as either hyperreflective, granular, or hyporeflective when using OCT.[11,39] The conflicting descriptions of ODD morphology are a limitation in this as well as other ODD studies, and should be addresses in future research.

In conclusion, this study suggests that ODD volume is significantly associated with optic nerve dysfunction. Even though a worse MD is often found in patients with visible ODD, a more superficial anatomic ODD location is not necessarily associated with worse MD. The current classification using visibility by ophthalmoscopy is an unspecific marker of optic nerve dysfunction compared to quantitative measurements of ODD volume using EDI-OCT.

Acknowledgments

Supported by Fight for Sight, Denmark, and Synoptik-Fonden.

Disclosure: **L. Malmqvist**, None; **A.-S.W. Lindberg**, None; **V.A. Dahl**, None; **T.M. Jørgensen**, None; **S. Hamann**, None

References

1. Spencer WH. Drusen of the optic disk and aberrant axoplasmic transport. The XXXIV Edward Jackson memorial lecture. *Am J Ophthalmol*. 1978;85:1–12.
2. Friedman AH, Gartner S, Modi SS. Drusen of the optic disc. A retrospective study in cadaver eyes. *Br J Ophthalmol*. 1975; 59:413–421.
3. Lee AG, Zimmerman MB. The rate of visual field loss in optic nerve head drusen. *Am J Ophthalmol*. 2005;139:1062–1066.
4. Petersen HP. Colloid bodies with defects in the field of vision. *Acta Ophthalmologica*. 1957;35:243–272.
5. Khan MA, Forman AR. Legal blindness from severe optic nerve head drusen. *JAMA Ophthalmol*. 2016;134:e153660.
6. Knight CL, Hoyt WF. Monocular blindness from drusen of the optic disk. *Am J Ophthalmol*. 1972;73:890–892.
7. Auw-Haedrich C, Staubach F, Witschel H. *Optic disk drusen*. *Surv Ophthalmol*. 2002;47:515–532.
8. Malmqvist L, Wegener M, Sander BA, Hamann S. Peripapillary retinal nerve fiber layer thickness corresponds to drusen location and extent of visual field defects in superficial and buried optic disc drusen. *J Neuroophthalmol*. 2016;36:41–45.
9. Traber GL, Weber KP, Sabah M, Keane PA, Plant GT. Enhanced depth imaging optical coherence tomography of optic nerve head drusen: a comparison of cases with and without visual field loss. *Ophthalmology*. 2017;124:66–73.
10. Mistlberger A, Sitte S, Hommer A, et al. Scanning laser polarimetry (SLP) for optic nerve head drusen. *Int Ophthalmol*. 2001;23:233–237.
11. Lee KM, Woo SJ, Hwang JM. Morphologic characteristics of optic nerve head drusen on spectral-domain optical coherence tomography. *Am J Ophthalmol*. 2013;155:1139–1147.e1131.
12. Yi K, Mujat M, Sun W, et al. Imaging of optic nerve head drusen: improvements with spectral domain optical coherence tomography. *J Glaucoma*. 2009;18:373–378.
13. Lee KM, Woo SJ, Hwang JM. Morphologic characteristics of optic nerve head drusen on spectral-domain optical coherence tomography. *Am J Ophthalmol*. 2013;155:1139–1147.
14. Malmqvist L, De Santiago L, Fraser C, Klistorner A, Hamann S. Exploring the methods of data analysis in multifocal visual evoked potentials. *Doc Ophthalmol*. 2016;133:41–48.
15. Yushkevich PA, Piven J, Hazlett HC, et al. User-guided 3D active contour segmentation of anatomical structures: significantly improved efficiency and reliability. *Neuroimage*. 2006; 31:1116–1128.
16. Merchant KY, Su D, Park SC, et al. Enhanced depth imaging optical coherence tomography of optic nerve head drusen. *Ophthalmology*. 2013;120:1409–1414.
17. Sato T, Mrejen S, Spaide RF. Multimodal imaging of optic disc drusen. *Am J Ophthalmol*. 2013;156:275–282.e1.
18. Ghassibi MP, Chien JL, Abumasmah RK, Liebmann JM, Ritch R, Park SC. Optic nerve head drusen prevalence and associated factors in clinically normal subjects measured using optical coherence tomography. *Ophthalmology*. 2017;124:320–325.
19. Slotnick S, Sherman J. Buried disc drusen have hypo-reflective appearance on SD-OCT. *Optom Vis Sci*. 2012;89:E704–E708.
20. Li K, Wu X, Chen DZ, Sonka M. Optimal surface segmentation in volumetric images–a graph-theoretic approach. *IEEE Trans Pattern Anal Mach Intell*. 2006;28:119–134.

APPENDIX B

Paper B

Title

Linear, transfinite and weighted method for interpolation from grid lines applied to OCT images

Authors

Anne-Sofie Wessel Lindberg, Thomas Martini Jørgensen and Vedrana Andersen Dahl.

Year

2018

Proceedings

Applied Soft Computing vol 68, 2018.

Publication history

Submitted December 28, 2017. Accepted March 18, 2018.

Applied Soft Computing 68 (2018) 293–302

Contents lists available at ScienceDirect

Applied Soft Computing

journal homepage: www.elsevier.com/locate/asoc

Linear, transfinite and weighted method for interpolation from grid lines applied to OCT images

Anne-Sofie Wessel Lindberg*, Thomas Martini Jørgensen, Vedrana Andersen Dahl

Department of Applied Mathematics and Computer Science, Technical University of Denmark, DK-2800 Kgs. Lyngby, Denmark

ARTICLE INFO

Article history:
Received 28 December 2017
Received in revised form 16 March 2018
Accepted 18 March 2018
Available online 30 March 2018

Keywords:
Interpolation
Image processing
Performance analysis
Line scans
Medical image analysis

ABSTRACT

When performing a line scan using optical coherence tomography (OCT), the distance between the successive scan lines is often large compared to the resolution along each scan line. If two sets of such line scans are acquired orthogonal to each other, intensity values are known along the lines of a square grid, but are unknown inside each square. To view these values as an image, intensities need to be interpolated at regularly spaced pixel positions. In this paper we evaluate three methods for interpolation from grid lines: linear, transfinite and weighted. The linear method does not preserve the known values along the grid lines. The transfinite method, known from mesh generation, preserves the known values but might cause artifacts further away from the grid lines. The weighted method, which we propose, is designed to combine the desired properties of the transfinite method close to grid lines and the stability of the linear method further away. An important parameter influencing the performance of the interpolation methods is the upsampling rate. We perform an extensive evaluation of the three interpolation methods across a range of upsampling rates. Our statistical analysis shows significant difference in the performance of the three methods. We find that the transfinite interpolation works well for small upsampling rates and the proposed weighted interpolation method performs very well for all upsampling rates typically used in practice. On the basis of these findings we propose an approach for combining two OCT scans, acquired such that the lines of the second scan are orthogonal to the first.

1. Introduction

Scanning along a set of parallel lines is a common setting in optical coherence tomography (OCT) [8], well established in ophthalmology for obtaining volumetric images of the retina. Using OCT, the retina is scanned in depth (z) and along a line (x) with a high depth and transversal resolution, resulting in a single xz cross-section of the retina (a so-called B-scan). Collecting a number of images by scanning along parallel lines results in a volumetric xyz data set. Since scanning speed of the OCT systems employed in clinic is limited, and prolonged scanning is unpleasant for the patient, the distance between the recorded B-scans is often large compared to the transverse resolution of the B-scans. Therefore, if a xy cross-section (a so-called *en face* image) is of interest, the resolution is much coarser in the y-direction and pixels are non-square. Elongated pixels appear as stripes and influence the visual appearance of the image. The stripes can disturb the interpretation of the image and make it difficult to distinguish the anatomical structures. Furthermore, anatomical structures running in parallel to scan lines, e.g. blood vessels, are not visible.

To reveal additional anatomical structures, another OCT scan may be performed along the lines orthogonal to the first scan. Nevertheless, this leaves us with two volumes which are not straightforwardly combined, as pixels are sparsely sampled along the y-direction in the first image, while the second volume has pixels sparsely sampled along the x-direction. It is our goal to compute a volume which combines the information from those two volumetric scans. Several problems emerge in connection to this. The eye might move during scanning, and this needs to be accounted for. Furthermore, the intensity might vary significantly between the scans and images. And most importantly, the question is how to combine two volumetric scans covering the same area, one with high resolution cross-sections in the xz-planes, and the other in the yz-planes.

In this paper we re-visit the interpolation problem when combining two line scans which we previously addressed in [9]. In this extension of our prior work, we apply the developed methods for merging two OCT volumes. As we have a high resolution in the z-direction, we practically sample at any height and our prob-

* Corresponding author.
E-mail addresses: awli@dtu.dk (A.-S.W. Lindberg), tmjq@dtu.dk (T.M. Jørgensen), vand@dtu.dk (V.A. Dahl).

https://doi.org/10.1016/j.asoc.2018.03.031
1568-4946/

lem reduces to a 2D case. Furthermore, given high resolution along the scan lines we ignore the discrete sampling in this direction. Therefore, our problem is image interpolation from grid lines.

The problem is illustrated in Fig. 1(a). The information is available along the two sets of parallel lines, and it needs to be sampled at regularly spaced pixel positions.

To the best of our knowledge, the problem of interpolating information from grid lines while preserving boundary values has not been addressed in the context of image interpolation. In the context of mesh generation for finite element modeling a related problem is often solved using transfinite interpolation [6,7], a method for constructing a smooth function over a planar domain given the values on the boundary. Transfinite interpolation has been used for solving problems where information on boundaries should be preserved. It has been used in more recent studies e.g. [14] for solving time-dependent changes of volumetric material properties in heterogeneous volumes and in [12] for solving elliptic boundary value Poisson problems in arbitrary shaped 2D domains. In this work we employ the transfinite interpolation for image interpolation from grid lines, and we compare it against an approach based on linear upscaling. Furthermore, we propose a novel weighted interpolation which preserves the desirable properties of the transfinite and the linear method.

The three interpolation methods presented here only use the known intensity information along the grid lines. We would expect the performance to improve significantly if prior knowledge about the appearance of the images is incorporated in the method. A significant work in this line has been conducted for single-image super resolution [4] or image inpainting [1], for example using image patches [17] and sparse representation [15]. We believe that those methods might be adapted to solve the problem of interpolation from the grid lines.

Another alternative to the methods presented here involves adopting an interpolation scheme for scattered data, for example radial basis function [2]. By doing so we would not utilize the regularity of the grid lines. Furthermore, methods for interpolation from scattered points require setting a parameter which roughly corresponds to the average distance between data points. The approach is therefore sensitive to parameter tuning, when applied to regularly placed data points as in our problem.

A quality measure for merging two OCT scans should relate to the ease of distinguishing the anatomical structures present in the volume, their sharpness and precision. While sharpness may be quantified, it is difficult to assess the precision of the interpolation. Central to our problem is that we need to determine information where it is lacking. This aspect is similar to image upscaling and single-image super-resolution approaches. Therefore, when it comes to evaluating the performance of interpolation algorithms we turn to the conventional approach [18,13] which tests each method on a set of downsampled images and uses the peak signal-to-noise ratio (PSNR) metric.

During testing, we change the upsampling rates and statistically evaluate the results from the three interpolation methods. This allows us to evaluate the performance of the methods and to provide guidelines for different upsampling rates.

Based on our findings, we return to the OCT problem and develop a method for merging two OCT scans. There are a number of considerations before applying our interpolation to acquired OCT data. We need to assess the orthogonality of the two scans, ensure consistent intensity level, and correct for eye movement orthogonal to scanning plane. These adjustments are preformed as preprocessing of the OCT data. The complete method, including preprocessing steps, is presented as a case study in Section 5.

To summarize, the contribution of this paper is threefold. First, we suggest three methods for interpolation from grid lines, where we developed the novel weighted method such that it combines the desired properties from the two other methods. Second, we perform a rigorous statistical evaluation of the three methods for different data sets and upsampling rates, providing guidelines for the choice of method. Third, we apply the three interpolation methods on OCT images in a small case study.

2. Methods for interpolation from grid lines

Fig. 1(b) illustrates our interpolation problem focused on a single square region defined by two pairs of neighboring scan lines. This is a local coordinate system which we use when defining the three interpolation methods. The approach is then repeated for all squares in the image.

For a better explanation of the interpolation methods and their features, we bring an example in Fig. 2(a). The values to be interpolated are here shown as a height above a squared domain, where we know the values at the boundary.

2.1. Linear interpolation method

A naive approach of combining the two scans involves linearly upsampling each scan independently and averaging the results. Over one square domain we have

$$L_x(x, y) = (1 - y)S(x, 0) + yS(x, 1),$$
$$L_y(x, y) = (1 - x)S(0, y) + xS(1, y),$$
$$L = \frac{1}{2}(L_x + L_y),$$

where S are the known values along the boundary of the square domain, L_x and L_y are linearly upsampled boundaries in x and y direction, and L is the interpolant which we in this context denote *linear*. Construction of linear interpolation is demonstrated in Fig. 2(a)–(d).

Let us point out two properties of linear interpolation. First, every value $L(x, y)$ is a convex combination of four values from S. As a result, L does not produce undesirable overshoot. Secondly, for a point on the boundary, the underlying known data contributes only with a half of its value, the other half coming from the values at two corners. As a result, L does not agree with the known data along the boundaries of the domain. Those two properties combined lead to smeared-out appearance when linear interpolation is used on images.

2.2. Transfinite interpolation method

Transfinite interpolation is used for functions given on the boundary of a domain which can be parameterized as a square. For our purposes this reduces to

$$T = L_x + L_y - L_{xy},$$

where

$$L_{xy}(x, y) = (1 - x)(1 - y)S(0, 0) + (1 - x)yS(0, 1)$$
$$+x(1 - y)S(1, 0) + xyS(1, 1).$$

Here L_{xy} is the bilinear interpolant from the values at the corners of the domain, and T is the final transfinite interpolant. Those are shown in Fig. 2(e) and (f).

The most important property of the transfinite interpolation is that it preserves the known values at the boundary of the domain. To perceive how this property is achieved by the construction of T, note in Fig. 2 that at the boundary of the domain, L_{xy} differs from the known values exactly twice as much as L does.

Second important property is that T may overshoot. This is due to the negative term in the expression. All inside points receive eight

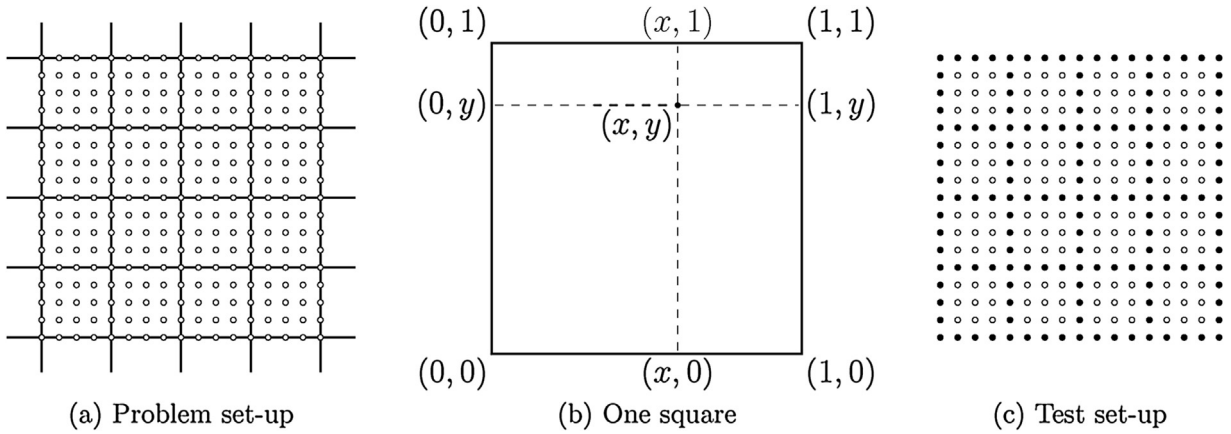

Fig. 1. Interpolation from the grid lines. (a) Two sets of scan lines with known intensities are shown in black, this needs to be sampled at regularly spaced pixel positions illustrated as white dots. (b) One square region defined by four scan lines and its local coordinate system. (c) Test set-up, black are the known and white are the unknown pixels, here shown with an upsampling rate of 4.

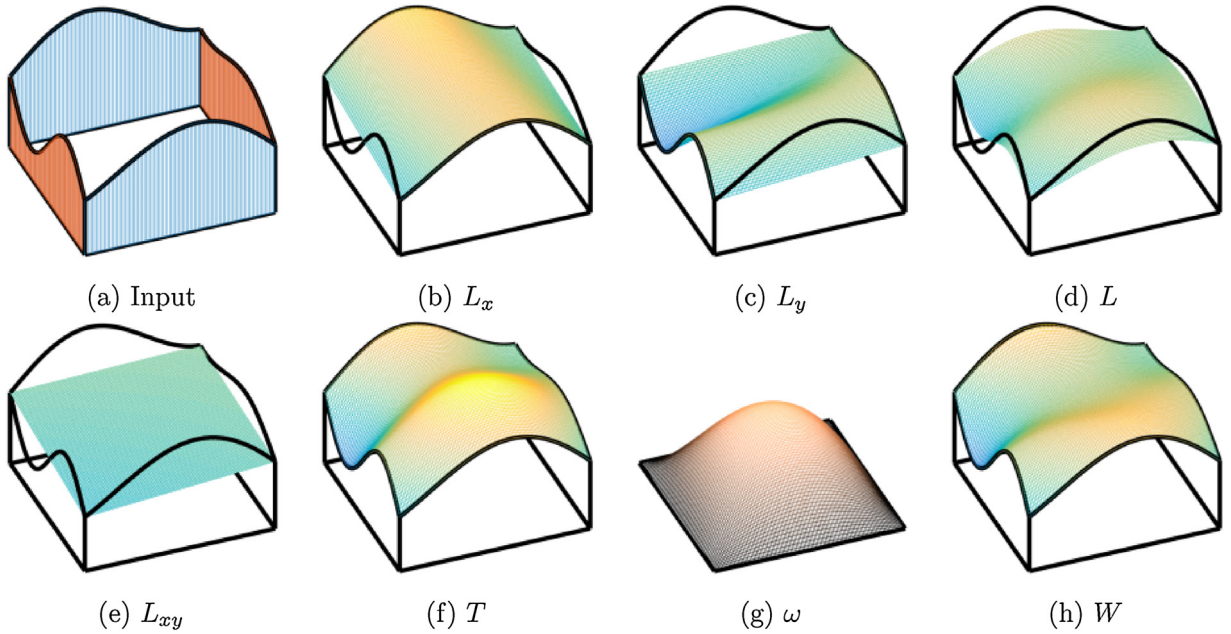

Fig. 2. Interpolation over one squared domain. (a) Known values from one direction in red and from the other direction in blue, (b) linear interpolation from one pair (blue) of rectangle sides, (c) linear interpolation from other pair (red) of sides, (d) mean of two linear contributions, (e) bilinear interpolation from corners, (f) transfinite interpolation, (g) weighting scheme (h) weighted interpolation. (For interpretation of the references to color in this figure legend, the reader is referred to the web version of the article.)

weighted contributions, and especially points close to the middle of the domain are prone to interpolation overshoot, also visible in Fig. 2(f).

2.3. Weighted interpolation method

Transfinite interpolation has the desired properties (preservation of the known data) at the boundary of the square domain while the undesired properties (overshoot) are inside the domain. Linear interpolation does not overshoot, but has issues at the boundary. To combine the good properties of both methods we propose smoothly blending the linear and the transfinite interpolation. We construct a blending function which is 0 at the boundary of the square domain

$$\omega(x, y) = 16x(1 - x)y(1 - y).$$

The constant 16 is chosen such that $\omega(0.5, 0.5) = 1$.

We define our novel interpolation, which we denote *weighted*, as

$$W = \omega L + (1 - \omega)T, .$$

This also evaluates to

$$W = (2 - \omega)L - (1 - \omega)L_{xy}.$$

The blending function and the weighted interpolation are shown in Fig. 2(g) and (h). The illustrated example confirms desirable properties of the weighted interpolation. Like transfinite, the weighted interpolant matches the exact values at the boundaries of the domain. However, thanks to blending with the linear interpolant, the overshoot from inside of the domain is reduced. Finally, the smooth blending function maintains a smooth appearance of the interpolant.

Fig. 3. Three images from the fundoscopy data set. Images depict anatomical structures at the fundus of the eye.

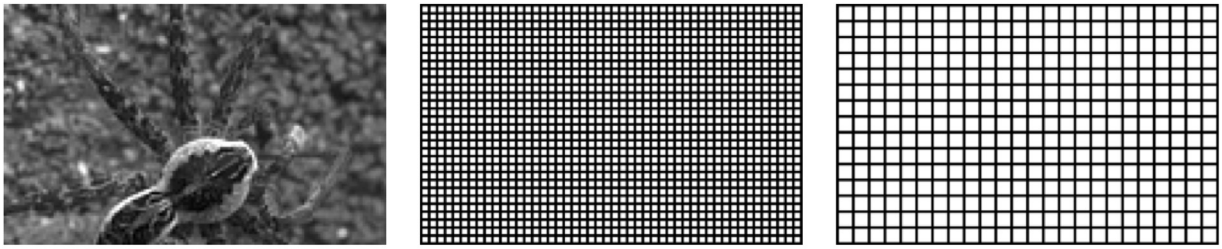

Fig. 4. Testing example. (a) Zoom on a detail in one of the images from the Berkley data set. (b) and (c) Grid lines with an upsampling rate of 3 and 6.

3. Quantitative measures used for evaluation of interpolation methods

Both objective and subjective tests are used [5] for evaluating the interpolation methods. Subjective tests measure a perceived image quality, while objective tests use a defined metrics for quantifying image quality or interpolation error. The choice of the tests and the quality measures depend on the intended use.

When used on OCT images, interpolation from grid lines is a step towards merging two OCT line scans. We plan to use the merged volume for automatic detection of anatomical structures and quantification of abnormalities in the eye. In this setting, the three interpolation methods will be evaluated in terms of the quality of the detection and quantification results.

In the work presented here, we bring a more meticulous and general evaluation of the interpolation methods based on measuring interpolation error for a specific upsampling rates. The ground truth is constructed by downsampling an image, which is then upsampled using the three methods, and the results are compared against the original image. For downsampling, we keep image columns and rows at a certain distance, which corresponds to an upsampling rate s. See Fig. 1(c) for our test set-up.

For a certain upsampling rate, the fraction of the unknown pixel is

$$u = \frac{(s-1)^2}{s^2}$$

For example, when $s = 2$ we keep every second row and every second column, and the fraction of unknown pixels is only 0.25.

To demonstrate the properties of the interpolation methods, we conduct tests for upsampling rates from 2 to 30. However, the high upsampling rates (above 10) are of limited practical value due to a high degeneration of image quality.

3.1. Data sets used for quantification of interpolation methods

We evaluate the three interpolation methods on two data sets. The first contains 200 images from the Berkley Segmentation data set [11], which is widely used for evaluations of image upscaling and super-resolution algorithms [3]. The images depict scenes from nature such as landscapes, people and animals, covering a wide range of image patterns at all scales. We converted rgb Berkley data set images into grayscale prior to processing. The second data set is ophthalmologic data in the form of 72 funduscopies. Fundoscopy is an imaging technique for examination of fundus obtained using a light source and an ophthalmoscope. This was chosen because the image content is similar to OCT scans, and will allow us to assess the performance of the interpolation methods in a setting which resembles to our application. Fig. 3 shows some examples of the funduscopies.

3.2. Performance measurement used for method assessment

The interpolation quality is assessed by the pixelwise difference between the ground truth image and the interpolated image. The interpolation error can be evaluated as the root mean square error (RMSE) which is defined as

$$\mathrm{RMSE} = \sqrt{\frac{1}{N}\sum_{i=1}^{N}\left(\hat{I}(i) - I(i)\right)^2},$$

where summation runs over all pixels i from the original image I and the interpolated image $\hat{I}$ [10].

As a measure of interpolation quality, a closely related peak signal-to-noise ratio (PSNR) is most often used [18]. The PSNR is measured in dB and is defined as [16]

$$\mathrm{PSNR} = 20\log_{10}\left(\frac{I_{\max}}{\mathrm{RMSE}}\right),$$

where I_{max} is the maximum pixel intensity value, in our case 1.

4. Results of quantitative evaluation

First, we visually evaluate the results from the interpolations for upsampling rate 3 and 6 on a few images. Second, we compute the mean performance of each interpolation method for upsampling rates varying between 2 and 30. Last, we present the results from a statistical analysis based on the measured performance of the three methods.

4.1. Interpolated results

The differences in performance of the three interpolation methods are subtle, and to visualize the results we bring a small detail of an image from the Berkley segmentation data set in Fig. 4(a), and we also show the grid lines for upsampling rate 3 and 6 in Fig. 4(b) and (c). The interpolated results for this image, the two sets of grid lines and the three interpolation methods are shown in Fig. 5. We also bring the pixelwise error between the interpolated images and the original image. It can be seen that the error is zero along the grid lines for the transfinite and the weighted interpolation, while this is not the case for the linear interpolation. Furthermore, for all methods, the interpolation quality in the form of the PSNR decreases when the upsampling rate is increased. For this example, the weighted interpolation outperforms the transfinite when using upsampling rate 6.

4.2. Performance analysis

Fig. 6 shows the PSNR values for the three interpolation methods for 10 images from the Berkley segmentation data set, interpolated with upsampling rate 6. The images were chosen randomly using pseudorandom integers generated in our testing script. We see a big variance in performance across the images, compared to relatively small variance between the three interpolation methods. However, weighted interpolation obtains the best performance for 8 out of 10 images, while the transfinite method is best for the other two images. The linear method is not the best for any of the images, but is still superior to transfinite in 5 out of 10 images.

To evaluate an overall performance of the interpolation methods, we computed the mean PSNR for the whole Berkley segmentation data set, for each interpolation method and for a range of upsampling rates. We conducted a similar experiment for the fundoscopy data set. Fig. 7 shows a plot of the obtained values with upsampling rates varying between 2 and 19. We notice the same performance pattern for both data sets. The transfinite method has the largest mean PSNR for smallest upsampling rates, while the linear method has the largest mean PSNR for highest upsampling rates. In the interval around the point where the transfinite and the linear method cross, the weighted method achieves the highest mean PSNR.

We conducted experiments for upsampling rate up to 30, and we confirm that the linear method achieves best mean PSNR for high upsampling rates. We find this being of limited practical value, as for upsampling rates higher than 18 we interpolate over 89% of the pixels in the image.

As already shown in Fig. 6, the variance of performances is large between the images and small between the methods. To confirm our findings presented in Fig. 7, we performed a statistical test of the interpolation performance measured by the PSNR value. We set up a regression model to investigate the correlation between the PSNR value and the categorical variables for image and for method, for each sampling rate. *F*-values indicate that the method is the main descriptor. Moreover, we found that a significant difference between the three methods exists. Therefore, we tested the methods pairwise to check for difference between them at each upsampling rate and moreover, to find out which method performs best. The results are listed in Table 1(a) for the Berkley data set and in Table 1(b) for the fundoscopy data set. The results show the same trend, and we use notation *a*/*b* when referring to the two data sets. It is seen that the transfinite interpolation performs best for upsampling rates below 3/4 and the weighted interpolation performs best for sampling rates above 4/5 and below 15/20. The linear method performs best for upsampling rates above 20/22.

Table 1
Results from statistical analysis of interpolation performance for three methods at different upsampling rates, for the Berkley data set (a) and the fundoscopy data set (b). The methods are linear (L), weighted (W) and transfinite (T), and upsampling rates are shown in intervals between 2 and 30. Number 1 indicates the method that performs best for a given upsampling rate, while 3 indicates the method that performs worst.

	2	3	4–5	6	7–14	15–20	21–30
(a) Berkley data set							
L	3	3	3	2*	2	**1***	**1**
W	2	**1***	**1**	**1**	**1**	**1***	2
T	**1**	**1***	2	2*	3	3	3

	2–3	4	5–6	7–8	9–19	20–22	23–30
(b) Fundoscopy data set							
L	3	3	3	2*	2	**1***	**1**
W	2	**1***	**1**	**1**	**1**	**1***	2
T	**1**	**1***	2	2*	3	3	3

* No significant difference was found between the two methods for the given upsampling rate.

5. Case study: Optical coherence tomography of the optic nerve head

Our investigation in methods for interpolation from grid lines was motivated by optical coherence tomography (OCT) images of the eye retina. We wanted to produce an *en face* image of the optic nerve head (ONH), the point in the eye where the optic nerve fibers leave the retina.

Based on the interpolation methods, we developed a general approach for creating *en face* images from two OCT scans through volume merging. In this section we present our approach with focus on ONH images as a case study. Note that the method can be applied to retinal OCT images in general.

5.1. Data acquisition

When using OCT, the retina of the eye is scanned in depth and along a set of lines. Two sets of line scans are acquired. During acquisition, the operator manually initiates the scanning so that the ONH is approximately at the center of the scan. The first scan is acquired along the lines running from left to right, so each line gives a cross-section image of the ONH in the anatomical transverse plane. The second scan is acquired along the lines orthogonal to the first one, i.e. running from the top to the bottom, so acquired images are in the anatomical sagittal plane. In our notation, the first scan is acquired along the lines parallel with the *x*-axis, and results in a set of images in *xz*-plane. We will call this a *x*-direction scan. Similarly, the second scan, resulting in a set of *yz* cross-section images, is denoted a *y*-direction scan.

For our main example, each set of the data consists of 97 line scans (so-called B-scans) and each line scan contains 768 depth-measurements (so-called A-scans). This means that the *x*-direction scan represents a volume containing ONH by $768 \times 97 \times 496$ voxels, while the *y*-direction scan represents the same volume by $97 \times 768 \times 496$ voxels. Likewise, the voxel size for the *x*-direction

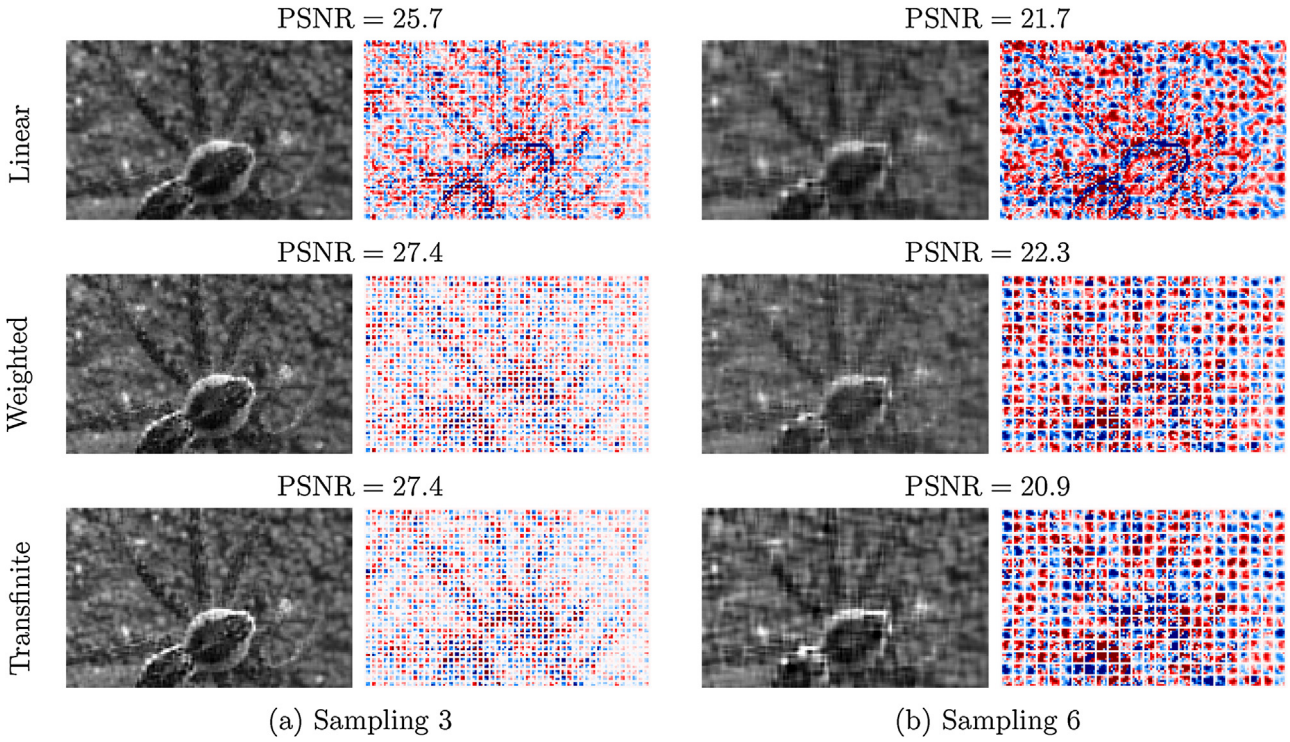

Fig. 5. The interpolated results for the detail and the grid lines shown in Fig. 4. The interpolation methods are presented with linear on top, weighted in the middle and transfinite in the bottom row. Columns (a) and (b) bring the results for an upsampling rate of 3 and 6. The PSNR value for each interpolated image is listed above it. Next to each interpolated image is the pixelwise difference between the interpolated image and the original image, with red and blue color indicating positive and negative difference respectively, and white indicating zero difference. (For interpretation of the references to color in this figure legend, the reader is referred to the web version of the article.)

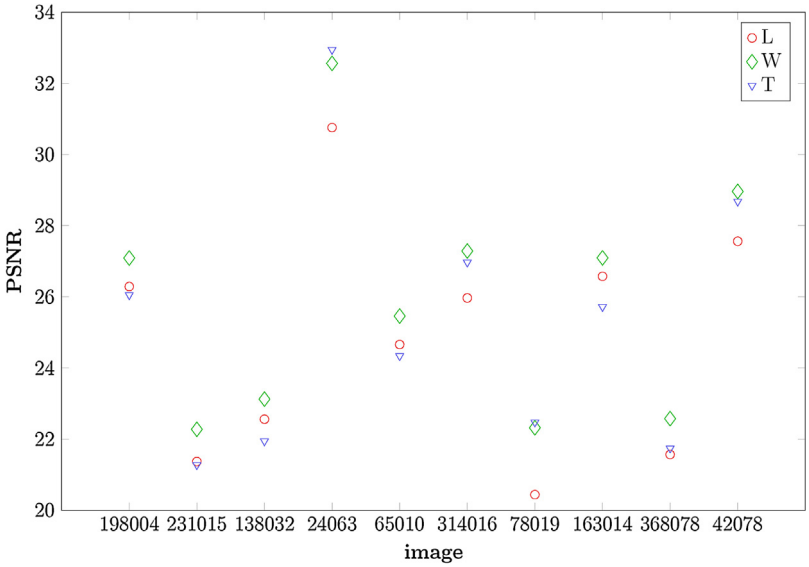

Fig. 6. A set of 10 randomly chosen images from the Berkley segmentation data set, and the resulting PSNR for three interpolation methods, linear (L), transfinite (T) and weighted (W). Upsampling rate is 6.

scan is 5.7 μm × 30 μm × 3.9 μm and for the *y*-direction scan the voxel size is 30 μm × 5.7 μm × 3.9 μm.

5.2. Preprocessing

As mentioned earlier, interpolation from the grid lines is only one step in the OCT volume-merging approach. To be brought in a format appropriate for interpolation, OCT volumes need to undergo three preprocessing steps. While this is not a main focus of this paper, in order to make the case study self-contained, we briefly cover the preprocessing steps.

The first preprocessing step is an alignment of the two volumes in the *xy*-plane. While scanning, the operator will attempt to cover the same region of the ONH within the two scans. However, since this is done manually, there might be a slight misalignment between the scans. To obtain an exact alignment of the volumes in the *xy*-plane, we generate 2D images by summing all voxels in the *z*-direction, and resample the images so that pixels are square. To these images we apply an intensity-based image registration with

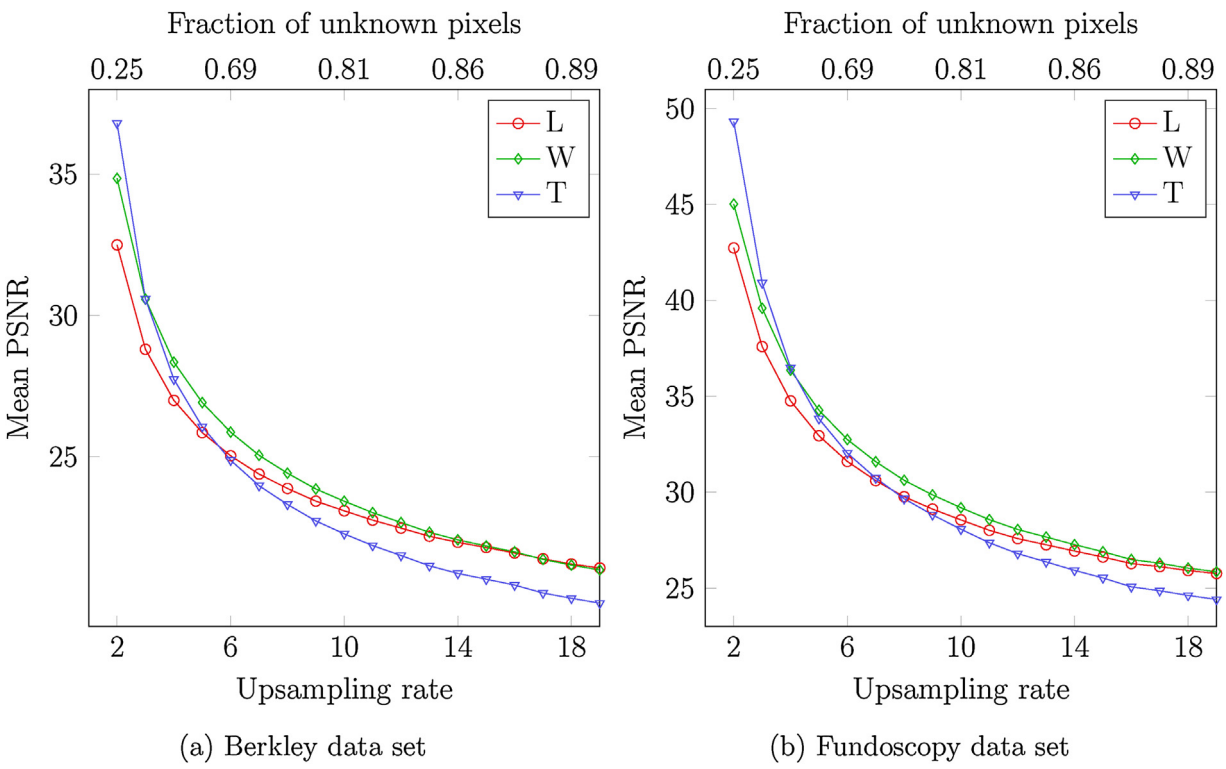

Fig. 7. Comparison of the linear (L), transfinite (T) and weighted (W) interpolation. The mean PSNR value for (a) Berkley and (b) fundoscopy data set at different upsampling rate. The horizontal axis above the graphs indicates the fraction of unknown pixels.

the mean square difference as similarity measure. The result is a *xy*-plane translation of one image with respect to the other, giving us a corrected relative placement of the *x*-direction and the *y*-direction scan. Note that the registration also reveals a rotation between the *x*-direction and *y*-direction scan, which is important to check for, since our approach assumes orthogonality.

The second preprocessing step involves defining a grid for interpolation. After alignment, we know the exact placement of the two sets of line scans in the *xy*-plane. While the sampling resolution along the scan lines is high, it is still finite, and we need to resample the images into a format suitable for interpolation. This is illustrated in Fig. 8. We first identify the crossing points between line scans. This defines a coarse square grid, with the outermost points outlining the region of interest. Given a certain upsampling rate, we subdivide the coarse grid into a fine grid. The two scan volumes are then resampled according to the points in the fine grid. Here we use linear interpolation. Thanks to the high resolution along the scan lines, we can resample the images with only a slight loss of information.

The number of crossing points varies depending on the overlap between the scans. For the data used in this case study, all line scans overlap and the coarse grid is of size 97×97. The size of the fine grid depends on the upsampling rate. For the examples shown in the case study we use upsampling rate of 5, so the fine grid has $5(97-1)+1 = 481$ points in each direction.

The third preprocessing step corrects for eye movement in the *z*-direction. During a single scan, OCT scanner will track eye features and correct for eye movement in *xy*-plane. However, eye movement in the *z*-direction is not corrected for, and it can be quite large, especially between two scans. We estimate the displacement between two A-scans (depth-measured signal in the *z*-direction) using cross-correlation. This is done only in the coarse grid (crossing points), while displacement for the fine grid is obtained by interpolation. The columns of the scans are then re-sampled and cropped if needed.

Finally, for our method to work, overall intensity levels need to be consistent across scans. We assessed that the data used in this study required no additional adjustment of intensities.

5.3. Interpolation

The preprocessing provides two aligned volumes covering exactly the same part of the ONH. The first volume, obtained from the *x*-direction scan, has $481 \times 97 \times 496$ voxels, while the second volume, obtained from the *y*-direction scan, has $97 \times 481 \times 496$ voxels. We now merge the volumes by processing one *z*-slice (i.e. *xy*-plane for a given *z*) at a time. Our prototype implementation of volume merging produces results for all three interpolation methods, so we can visually compare the outputs.

5.4. Case study results

We present the results of merging two OCT volumes on one *xy*-cross section image, *en face* image, in Fig. 9. We show the *x*-direction scan, the *y*-direction scan and the interpolated results for the three methods: linear, transfinite and weighted.

In both the *x*-direction and *y*-direction scan the anatomical structures parallel to scan lines are less pronounced. Furthermore, one can notice stripes in the scan direction, which might potentially influence the interpretation of the images. The results for all three interpolation methods show the benefit of combining two orthogonal set of line scans into a higher resolution *en face* image with squared pixels. Anatomical structures such as blood vessels become more distinct when two scans are combined. Furthermore, on the merged images in Fig. 9 we notice the reduction of horizontal and vertical stripes.

Given our results from the performance analysis of the three interpolation methods, we saw that the weighted method performed best for upsampling rate 5 used for our case study. Therefore, we show in Fig. 10 the results for *en face* images from

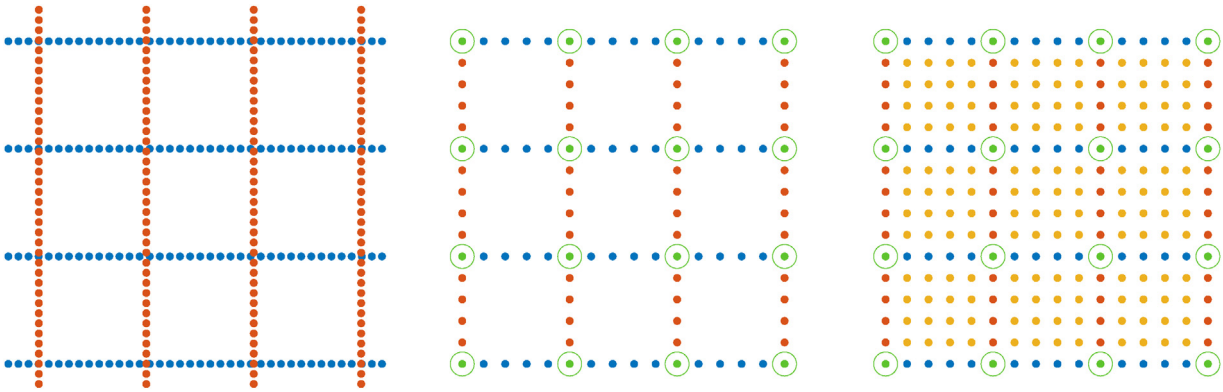

Fig. 8. Defining an interpolation grid. (a) Original sampling, blue indicating *x*-direction scan and red indicating *y*-direction scan. (b) Crossing points defining the coarse square grid are green, and points for resampling along the *x*-direction and the *y*-direction scan lines are blue and red respectively. (c) Orange points are added, such that green, blue, red and orange points together yield the fine grid used for interpolation. (For interpretation of the references to color in this figure legend, the reader is referred to the web version of the article.)

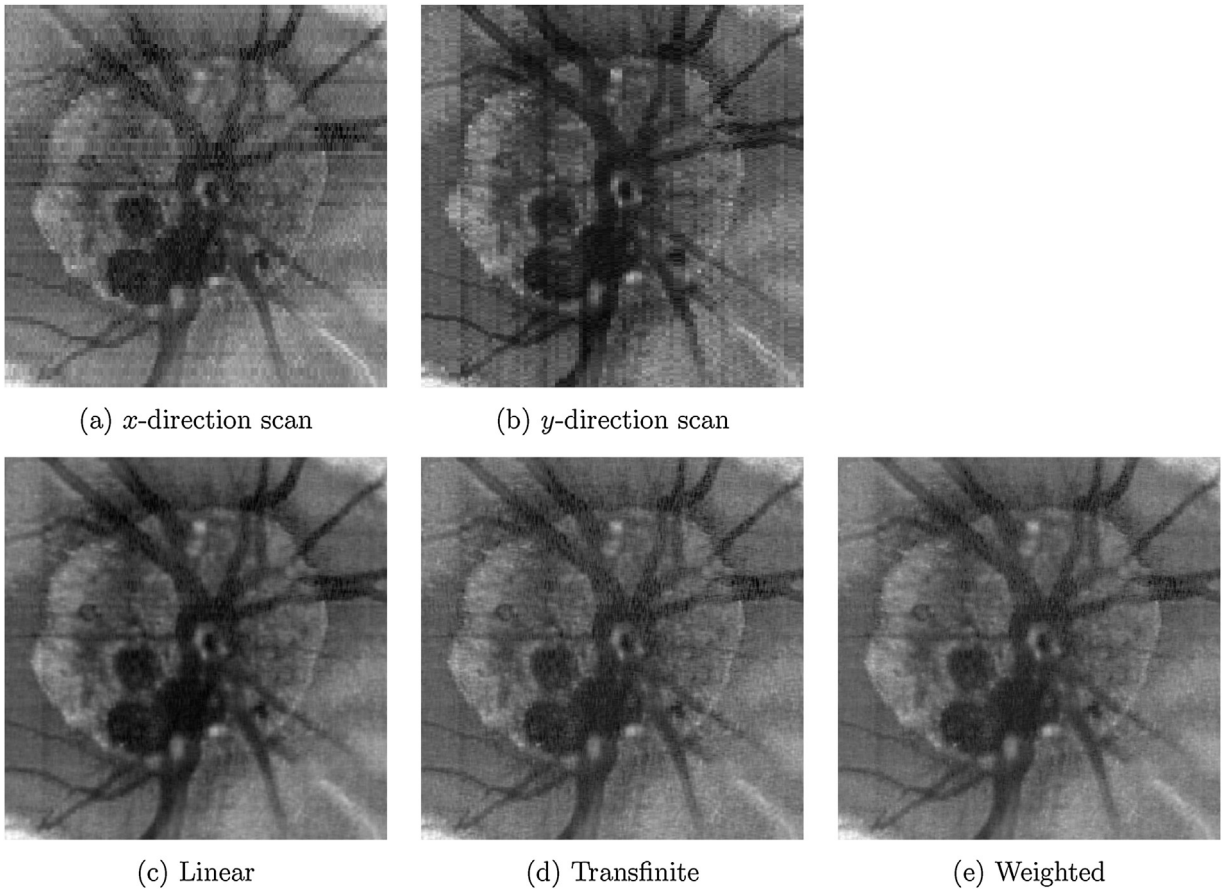

Fig. 9. Results of merging two OCT scans of ONH, shown on one *en face* image: (a) *x*-direction scan, (b) *y*-direction scan, (c) result produced using linear interpolation, (d) result of transfinite interpolation and (e) result of weighted interpolation.

three different patients obtained with the weighted interpolation method.

6. Discussion

Our experiments and the statistical evaluation of the three interpolation methods are in alignment with the previously demonstrated properties of the methods. Prior to experiments, we knew that the transfinite methods perform best close to the grid lines containing known information, while the linear method performs best in areas further away from the grid lines. Therefore, we expected the transfinite method to achieve superior results for small upsampling rates where grid lines cover a large fraction of the image. Our results confirm this hypothesis. Likewise, we show that linear method is superior at high upsampling rates.

We designed the weighted method to combine the good properties of the linear and transfinite method. Our results confirm that weighted method has superior performance for a large interval of

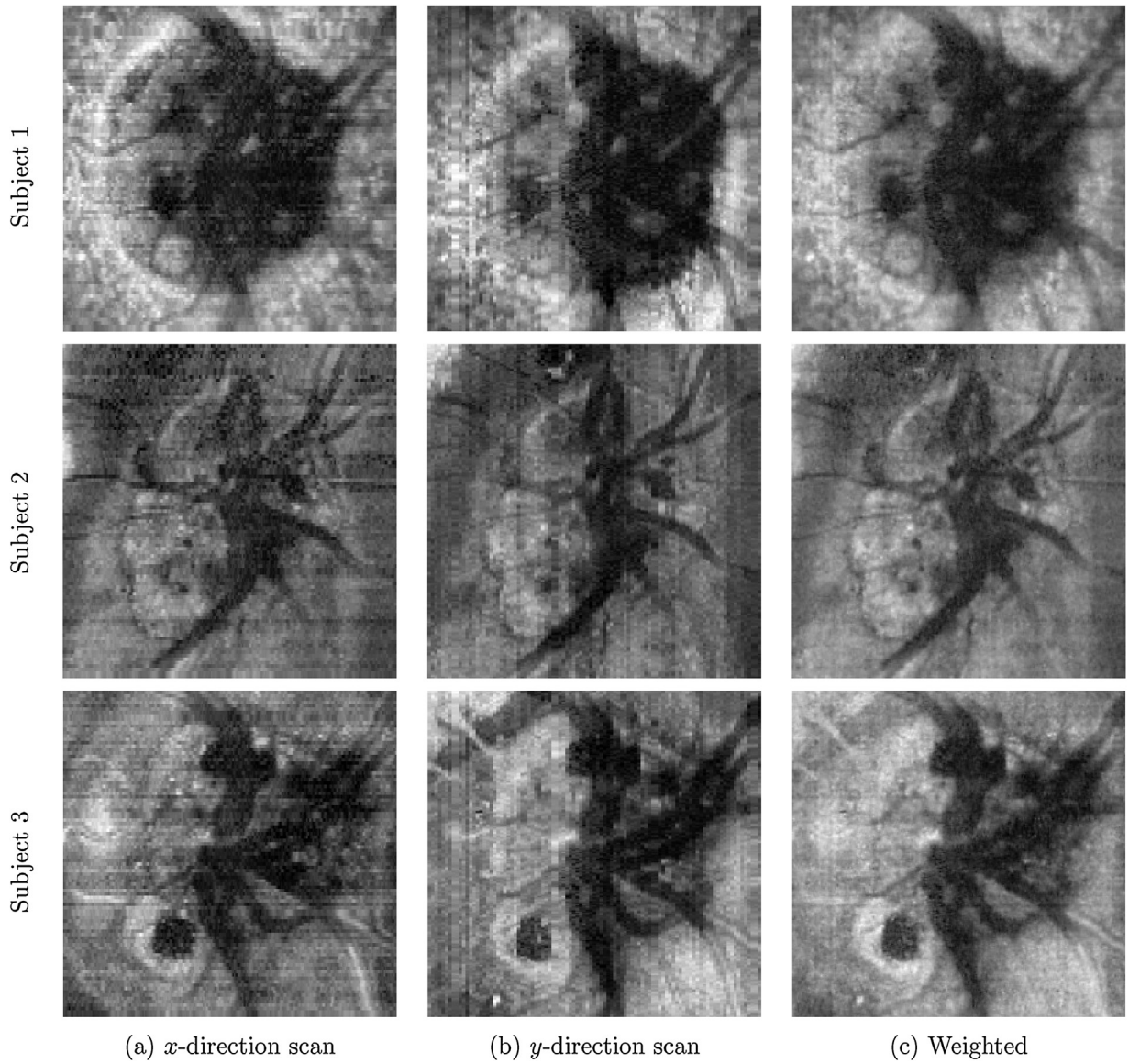

Fig. 10. Three different *en face* OCT images of ONH produced using weighted method for interpolation from the grid lines. The upsampling rate is 5. Images in column (a) are from x-direction scans, column (b) are from y-direction scans and column (c) are the interpolated results.

upsampling rates, and especially where the transfinite and linear method performs equally badly. This happens around upsampling rate of 7 and the interval where weighted method is superior extends from 4 to more than 15. The upsampling rate for our case study application of merging OCT images is 5, and we expect the suggested weighted interpolation method to be superior.

We measured image peak signal-to-noise ratio (PSNR) to quantify the interpolation quality. It is important to note that PSNR is only one indicator of the quality of interpolation. Further investigation that measures image quality in terms of sharpness should be performed for finding the most suitable method. Likewise, if the images are to be used for visual inspection, a perceived quality of the images should be measured.

Visually observed quality of the images is central in our case study, where we applied the three interpolation methods on optical coherence tomography (OCT) images of the optic nerve head (ONH). All three interpolation methods successfully reduce the disturbing stripe artifacts present in the row images, and improve visualization of anatomic structures e.g. blood vessels. The difference in the performance of the three interpolation methods is subtle, but based on our previous results we conclude that the weighted interpolation should be used for OCT images.

In our approach of merging OCT scans the interpolation step relies on the assumption that the scan lines are orthogonal, and the intensities of the two scans are consistent. Bringing the input data into a format suitable for interpolation, and assessing the validity of assumptions is therefore crucial for the performance of the method. For this reason it is difficult to asses the quality of interpolation step on the acquired data, as it is highly dependent on the preprocessing.

The true value of our interpolation will be evident when we include it in a targeted application. We plan on developing a method for quantifying the volume of optic disc drusen, which will be tested within a larger clinical study. We hope that our interpolation method will improve the results of an automatic detection algorithm.

7. Conclusion

Our work on interpolation from grid lines has three main contributions. First, we introduce the problem of interpolation from grid

lines and suggest three possible solutions: a linear, a transfinite and a weighed interpolation. Second, we systematically test the three methods and conclude that the transfinite method is superior for very small upsampling rates, while the weighted method should be chosen for a broad range of upsampling rates. Lastly, through a case study, we demonstrate the use of the proposed interpolation methods and the benefits of merging two line scans.

References

[1] M. Bertalmio, G. Sapiro, V. Caselles, C. Ballester, Image inpainting, in: Proceedings of the 27th Annual Conference on Computer Graphics and Interactive Techniques, ACM Press/Addison-Wesley Publishing Co, 2000, pp. 417–424.

[2] M.D. Buhmann, Radial Basis Functions: Theory and Implementations, 2003.

[3] W. Dong, L. Zhang, G. Shi, X. Wu, Image deblurring and super-resolution by adaptive sparse domain selection and adaptive regularization, IEEE Trans. Image Process. 20 (7) (2011) 1838–1857.

[4] M. Elad, A. Feuer, Restoration of a single superresolution image from several blurred, noisy, and undersampled measured images, IEEE Trans. Image Process. 6 (12) (1997) 1646–1658.

[5] A. Giachetti, N. Asuni, Real-time artifact-free image upscaling, IEEE Trans. Image Process. 20 (10) (2011) 2760–2768.

[6] W.J. Gordon, C.A. Hall, Construction of curvilinear co-ordinate systems and applications to mesh generation, Int. J. Numer. Methods Eng. 7 (4) (1973).

[7] W.J. Gordon, C.A. Hall, Transfinite element methods: blending-function interpolation over arbitrary curved element domains, Numer. Math. 21 (2) (1973) 109–129.

[8] D. Huang, E.A. Swanson, C.P. Lin, J.S. Schuman, W.G. Stinson, W. Chang, M.R. Hee, T. Flotte, K. Gregory, C.A. Puliafito, J.G. Fujimoto, Optical coherence tomography, Science 254 (5035) (1991).

[9] A.S.W. Lindberg, T.M. Jørgensen, V.A. Dahl, Interpolation from grid lines: linear, transfinite and weighted method, in: Scandinavian Conference on Image Analysis, Springer, 2017, pp. 338–349.

[10] V. Loia, S. Sessa, Fuzzy relation equations for coding/decoding processes of images and videos, Inf. Sci. 171 (1–3) (2005).

[11] D. Martin, C. Fowlkes, D. Tal, J. Malik, A database of human segmented natural images and its application to evaluating segmentation algorithms and measuring ecological statistics., Proceedings of the 8th International Conference in Computer Vision, vol. 2 (2001, July) 416–423.

[12] C.G. Provatidis, Solution of two-dimensional Poisson problems in quadrilateral domains using transfinite coons interpolation, Commun. Numer. Methods Eng. 20 (7) (2004).

[13] Y. Romano, M. Protter, M. Elad, Single image interpolation via adaptive nonlocal sparsity-based modeling, IEEE Trans. Image Process. 23 (7) (2014) 3085–3098.

[14] M. Sanchez, O. Fryazinov, V. Adzhiev, P. Comninos, A. Pasko, Space-time transfinite interpolation of volumetric material properties, Trans. Vis. Comput. Graph. 21 (2) (2015).

[15] B. Shen, W. Hu, Y. Zhang, Y.J. Zhang, Image inpainting via sparse representation., Proceedings of the IEEE International Conference on Acoustics, Speech, and Signal Processing (2009, April) 697–700.

[16] M.M. Sung, H.J. Kim, E.K. Kim, J.Y. Kwak, J.K. Yoo, H.S. Yoo, Clinical evaluation of JPEG2000 compression for digital mammography, Nucl. Sci. 49 (3) (2002).

[17] Z. Xu, J. Sun, Image inpainting by patch propagation using patch sparsity, Trans. Image Process. 19 (5) (2010).

[18] C.Y. Yang, C. Ma, M.H. Yang, Single-image super-resolution: a benchmark, in: European Conference on Computer Vision, Springer, 2014, pp. 372–386.

APPENDIX C

Paper C

Title

Determination of peripapillary vessel density in optic disc drusen using EDI-OCT and OCT angiography

Authors

Anne-Sofie Wessel Lindberg, Vedrana Andersen Dahl, Isabelle Karlesand, Lea Lybek Rueløkke, Lasse Malmqvist and Steffen Hamann.

Year

2020

Proceedings

Experimental Eye Research Vol 197, 2020.

Publication history

Submitted January 30, 2020. Accepted June 15, 2020.

Experimental Eye Research 197 (2020) 108123

Contents lists available at ScienceDirect

Experimental Eye Research

journal homepage: www.elsevier.com/locate/yexer

Research article

Determination of peripapillary vessel density in optic disc drusen using EDI-OCT and OCT angiography

Anne-Sofie Wessel Lindberg [a,*], Vedrana Andersen Dahl [a], Isabelle Karlesand [b], Lea Lybek Rueløkke [b], Lasse Malmqvist [b], Steffen Hamann [b]

[a] Department of Applied Mathematics and Computer Science, Technical University of Denmark, Richard Petersens Plads, Building 324, 2800 Kgs. Lyngby, Denmark
[b] Department of Ophthalmology, Rigshospitalet, University of Copenhagen, Glostrup, Denmark

ARTICLE INFO

Keywords:
Optic disc drusen
Vessel density
Optical coherence tomography
Optical coherence tomography angiography
Clinical applications
Image analysis

ABSTRACT

Optical coherence tomography angiography (OCTA) is a rapidly developing technique which generates angiographic images non-invasively. This study proposes a method to determine the vessel density in OCTA scans in general and especially the local peripapillary vessel density. The method produces vessel density heatmaps that contain information about the local vessel density. We apply the method in a small study to demonstrate its applicability and its potential to investigate the influence of local conditions on the vessel density. In the study, we combine information from enhanced depth imaging optical coherence tomography (EDI-OCT) about the location of optic disc drusen (ODD) with information from OCTA about the vessel density. We see a reduction in local peripapillary vessel density in peripapillary sections with a large volume of ODD.

1. Introduction

Optical coherence tomography angiography (OCTA) is an increasingly used non-invasive imaging modality that provides in-vivo information on retinal and choroidal vasculature. The technique works as an extension of optical coherence tomography (OCT) using repeated B-scans to detect motion in the retinal layers. With the continuous improvement of OCT scanning speed, OCTA uses the decorrelation between repeated scans to separate static tissue from moving red blood cells, creating enface angiograms.

OCTA is today mainly used clinically in the diagnosis of choroidal neovascularization (CNV) (Moussa et al., 2017) but its use has also been investigated in a variety of other retinal and choroidal conditions as well as in optic nerve diseases (Chalam and Sambhav, 2016; Wang et al., 2018; Hata et al., 2017).

OCTA device manufacturers such as Heidelberg, Topcon, Zeiss etc. use different algorithms for motion detection and image processing (Hagag et al., 2017). This is unavoidable due to limitations and strengths in the setup of each device. There are also several OCTA quantification methods that provide continuous variables such as flow index and vessel density, and often these variables are calculated automatically in the software of the manufacturer making it difficult to understand the properties of the methods behind the calculations. Hence, the use of the OCTA technique is limited due to lack of consensus in the quantification of flow index and vessel density.

OCTA quantification of optic nerve head (ONH) blood flow has been particularly sparsely described in the literature. However, as it might provide insight into the pathophysiological mechanisms underlying optic neuropathies, there is growing interest.

In this work, we suggest a method for measuring the local peripapillary vessel density in the ONH. Our method produces vessel density heatmaps which can be used to investigate the influence of local conditions on the vessel density. We show how the influence of optic disc drusen (ODD) can be investigated by analysing OCTA images of a small group of ODD patients and healthy controls. By describing a reproducible method to quantify OCTA in the ONH and peripapillary, it is our hope that future studies of OCTA in various optic neuropathies will be more comparable.

2. Related work

In many studies relating to our method, the vessel density is determined using build-in functions e.g. as in Yarmohammadi et al. (2017), Zhang et al. (2019) and Yarmohammadi et al. (2016) with the software AngioVue. AngioVue expresses the vessel density as the percentage of segmented vessel pixels, but information about the steps in-between is lacking e.g. which segmentation is used.

Some studies calculate the vessel density using image processing software like GIMP, Photoshop and ImageJ. In a study by Iafe et al.

* Corresponding author.
E-mail address: awli@dtu.dk (A.-S.W. Lindberg).

https://doi.org/10.1016/j.exer.2020.108123
Received 30 January 2020; Received in revised form 27 May 2020; Accepted 15 June 2020
Available online 30 June 2020
0014-4835/

the vessels in the foveal avascular zone (FAZ) are binarized and skeletonized using ImageJ, and the vessel density is calculated as the percentage of vessel pixels using GIMP (Iafe et al., 2016).

To the best of our knowledge, there are no previously published studies that evaluate or suggest a method for calculating peripapillary vessel density using OCTA for local conditions such as ODD. A small study by Cennamo et al. (2017) reports significantly lower vessel density for ODD patients using built-in software, and another study by Gaier et al. (2017) shows a single case with decrease in local vessel density corresponding to an ODD. A recent study by Engelke et al. (2019) shows a reduction in the peripapillary vessel density for ODD patients compared to healthy controls using the software AngioVue.

Most studies investigating the peripapillary vessel density are based on glaucoma patients (Akil et al., 2017; Venugopal et al., 2018; Liu et al., 2015) and common for these studies is that the vessel density in the peripapillary region is expressed as the percentage of the vessel area.

3. Methods

We propose a method for quantification and visualization of the peripapillary vessel density within the ONH. We describe each step of our method, including the generation of the en face angiogram, segmentation of vessels, calculation of a vessel density heatmap, segmentation of the optic disc and addition of the Garway-Heath map. Furthermore, we show how this information can be combined with information obtained from OCT scans of the same patient by registering the OCTA scan to the OCT scan.

To evaluate its applicability, we apply the method to a small group of ten participants. It is important to note that the main purpose of the study was to develop a suitable method to determine the peripapillary vessel density. To keep the focus on the method, we refrain from carrying out a large clinical study of the influence of ODD on the peripapillary vessel density.

The study was a prospective observational method study approved by the Scientific Ethics Committee of the Capital Region, Denmark (H-4-2013-040). Informed consent was obtained from the subjects after explanation of the nature and possible consequences of the study. All procedures adhered to the tenets of the Declaration of Helsinki.

3.1. Data

All patients and healthy control subjects were examined at the Department of Ophthalmology at Rigshospitalet Glostrup, Denmark. Participants were inquired about their ophthalmic and medical history. Best corrected visual acuity was determined using Snellen visual acuity chart or ETDRS charts (4-meter original series, Precision-Vision, La Salle, IL, USA). Participants were examined using slit lamp biomicroscopy and intraocular pressure was measured by applanation tonometry.

The study includes five ODD patients and five healthy controls. OCTA scans were acquired for all ten participants, and EDI-OCT scans for the five ODD patients. For the ODD patients, the two scans were acquired on the same day.

Spectral domain enhanced depth imaging optical coherence tomography (EDI-OCT) volumes were acquired using a Spectralis HRA+OCT (Heidelberg Engineering, Heidelberg, Germany). Each volume has a voxel size of 5.7 μm × 30 μm × 3.9 μm and contains 768 × 97 × 496 voxels. This means that 97 B-scans are acquired with a distance of 30 μm and each B-scan is of dimension 768 × 496 pixels.

Optical coherence tomography angiography (OCTA) volumes were acquired using swept source angiography (Topcon DRI OCT Triton swept source OCT, Topcon, Japan). The OCTA volume contains 320 × 320 × 992 voxels and is a 6 × 6 mm scan. All OCTA scans had a signal strength index (SSI) above 50.

3.2. Vessel density from OCTA

To segment vessels and later express the vessel density, we first generate the en face angiogram from the OCTA volume. For each OCTA volume we have a structural OCT volume, which is the set of OCT B-scans that the OCTA is generated from.

3.2.1. Definition of slab and en face angiogram

The standard procedure for generating an en face angiogram is to define a slab at the structural B-scans. The slab is a layer in depth, that contains the angiography data that forms the en face angiogram. The slab should follow the retinal layers and therefore it needs to be determined from each scan. We chose our slab to range from the inner limiting membrane (ILM) and 150 μm in depth as in the study by Aghdam et al. (2018). We detect the ILM using a graph-based layer detection which is often used in OCT scans (Garvin et al., 2009). To minimize computation time, we downscale the structural B-scan volume by a factor of 2 in both directions of the anatomical frontal plane, while the resolution in depth is kept. Afterwards, the detected ILM is upscaled to fit the original scan resolution. The en face angiogram is calculated by averaging each column in the OCTA volume in depth defined by the slab.

3.2.2. Vessel segmentation

The vessels within the en face angiogram are segmented using an adaptive threshold algorithm (Bradley and Roth, 2007). The method is guided by one parameter, the sensitivity, that ranges from 0 to 1. Setting sensitivity higher than 0.5 leads to a higher proportion of pixels being thresholded as foreground, while setting sensitivity below 0.5 leads to a lower proportion of pixels being thresholded as foreground. In our desired segmentation, the proportion of foreground is lower than the proportion of background, so we need to choose a lower sensitivity. Experimenting with different values, we determined that sensitivity of 0.3 leads to a good separation of foreground and background.

The vessel density of a certain area can either be computed from the number of vessel pixels or from the length of the vessels. The thickness of the vessels within the ONH varies greatly, and the vessel structures in the peripapillary area consist mostly of small vessels with a few larger vessels. To express the vessels disregarding their thickness, we perform a skeletonization of the image with segmented vessels. The result is an image with lines, each representing a vessel.

3.3. Vessel density heatmap

To visualize the information about vessel density within different areas, we compute a heatmap image. The heatmap is built on the basis of the segmented vessels, each represented by a single line from the skeletonization. The heatmap is calculated as previously described in Lindberg et al. (2017). We use a Gaussian weighted circular sliding window. The size of the window is 300 μm, and the standard deviation of the Gaussian is 150 μm. The reason for using Gaussian weighting is to ensure that vessels close to the center of the sliding window are weighted higher than vessels far away from the center in the calculation of the vessel density. The vessel density score inside the sliding window is calculated as the weighted sum of the vessels, and the score is assigned to the pixel positioned at the center of the sliding window. We chose the size of the sliding window based on the distance between B-scans. The distance for OCT B-scans is 30 μm and approximately 19 μm for the structural B-scans from the OCTA scan. Our sliding window covers 10 to 16 B-scans for the two OCT volumes.

3.4. Segmentation of the optic disc and garway-heath map

To describe the vessel density in the peripapillary region, we first define the peripapillary region by segmenting the optic disc. The peripapillary region is afterwards divided into six sections known as a Garway-Heath map (Garway-Heath et al., 2000).

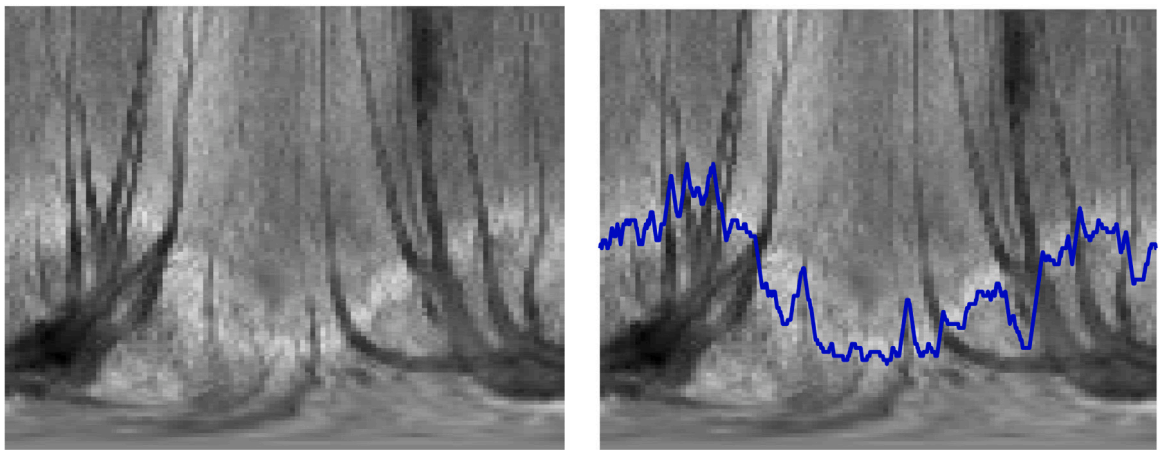

Fig. 1. Optic disc segmentation. Radially sampled image (a). Same as (a) with the detected layer representing the boundary of the optic disc (b).

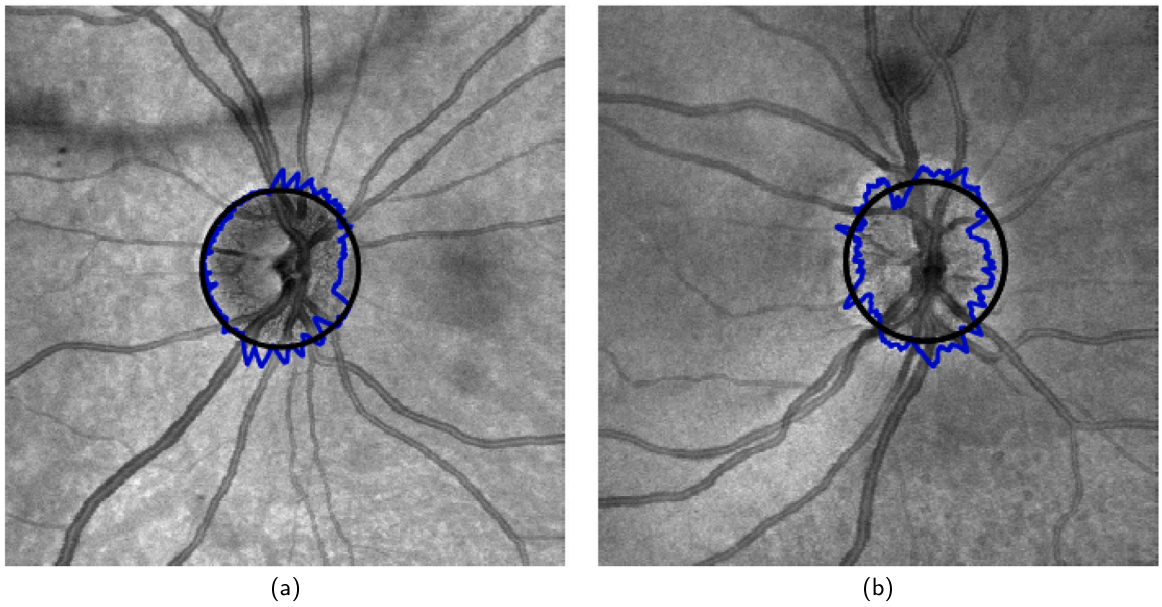

Fig. 2. En face images from structural B-scans from OCTA scan with optic disc segmentation (blue) and fitted circle (black) for (a) a healthy control and (b) an ODD patient. (For interpretation of the references to colour in this figure legend, the reader is referred to the web version of this article.)

3.4.1. Segmentation of the optic disc

For the segmentation of the optic disc, we use the structural B-scans from the OCTA scan. First, we create an en face image simply by summing up each column in depth. Second, we perform a manual selection of a center of the optic disc and do a radial sampling of the image (Fig. 1). Third, we detect the outer border of the optic disc in the radial sampled en face image using the same graph-based layer segmentation as for the segmentation of the ILM. We fit a circle to the detected border (Fig. 2). Even though most optic discs are slightly ellipsoidal, we chose to use a circle for simplicity and because the Garway-Heath map is circular.

3.4.2. Garway-heath map

The Garway-Heath map (Garway-Heath et al., 2000) is a well-known tool for relating the visual field areas to the regions of the optic disc. The map consists of two circles; an inner circle placed at the border of the optic disc, and an outer circle with a diameter of 3.46 mm. The map is the area between the inner and outer circle and is subdivided into six sections; temporal (T), temporal superior (TS), nasal superior (NS), nasal (N), nasal inferior (NI) and temporal inferior (I). We use the circle fitted to the segmented boundary of the optic disc as the inner circle, and we use its center to place the outer circle. We subdivide the area between the circles into the six sections as defined in Garway-Heath et al. (2000). The area of each section depends on the size of the optic disc and we account for this in the calculation of the vessel density in each section.

3.5. Combining information from OCTA and EDI-OCT

We want to combine the information about the vessel density from OCTA with information about the ODD from an EDI-OCT scan. The ODD is manually segmented by a medical doctor using the medical imaging segmentation tool ITK-SNAP (Yushkevich et al., 2006). Fig. 3 shows an EDI-OCT B-scan with and without the segmented ODD (green).

To combine the information between the two scans, we align the two scans by image registration using en face images created by summing the OCT volume and the OCTA structural B-scan volume in depth. The two scans are acquired on different machines and on different grids with different resolutions. We therefore resample both en face images

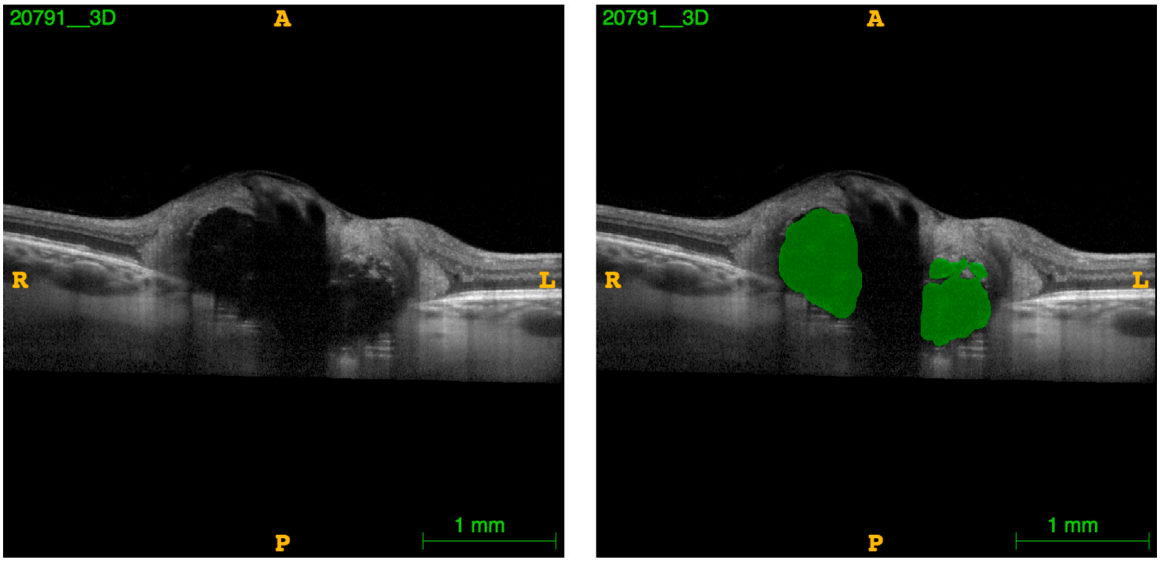

Fig. 3. Segmentation of ODD using the medical imaging segmentation tool ITK-SNAP, (a) EDI-OCT B-scan from an ONH scan of an ODD patient and (b) the same B-scan with the segmented ODD shown in green. (For interpretation of the references to colour in this figure legend, the reader is referred to the web version of this article.)

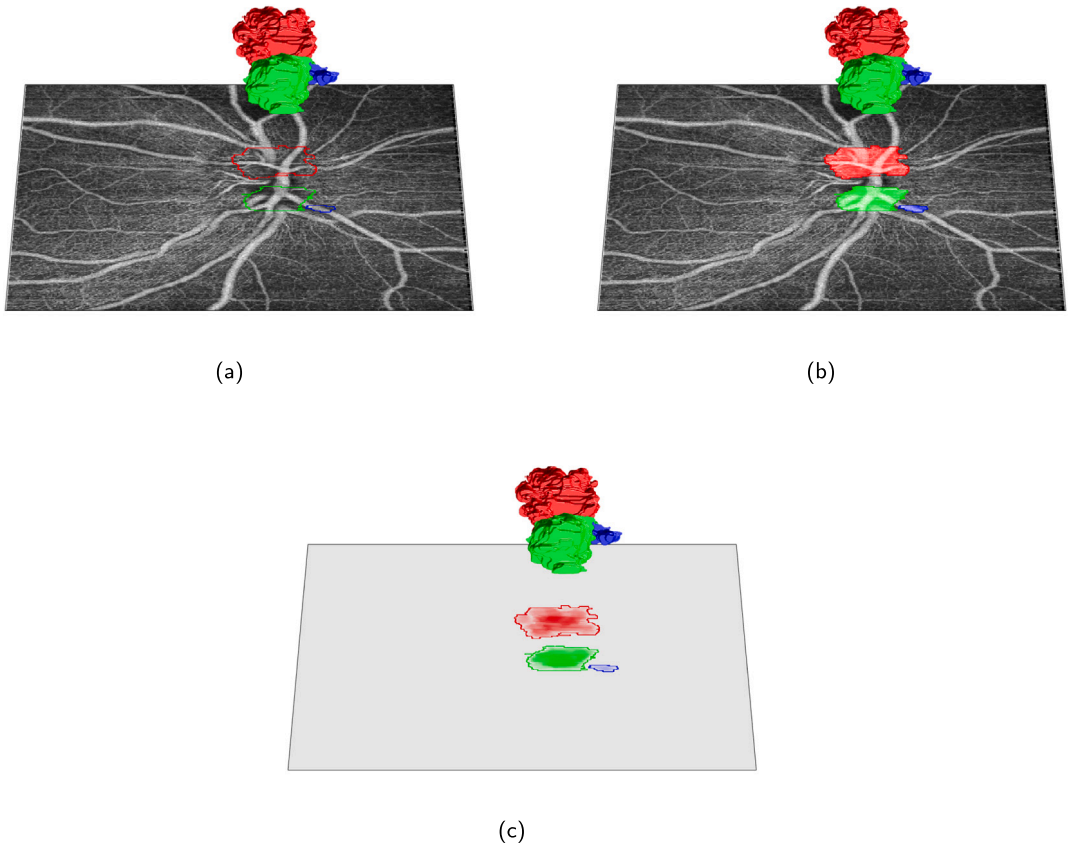

Fig. 4. 3D ODD information in the 2D plane of the en face angiogram. ODD location (a) expressed by the outer boundary of ODD in the 2D plane of the en face angiogram. ODD area (b) expressed as area inside boundary of each ODD and ODD volume (c) expressed as 2D height map calculated by summation of ODD voxels in depth.

such that they occupy the same regular grid, while maintaining the resolution as high as possible.

As an initialization step to the registration between OCTA and EDI-OCT images, we perform a translation between the two en face images based on three manually placed anatomical landmarks. Afterwards, we perform an automatic registration, including translation, rotation and scaling. Even though we assumed the rotation to be small between the two scans, we experienced that a slight rotation exists, presumably because of tilting of the head between acquisitions. The scaling is minimal and is only included to obtain the best fit. The registration maps the location of ODD into the OCTA volume to enable investigation

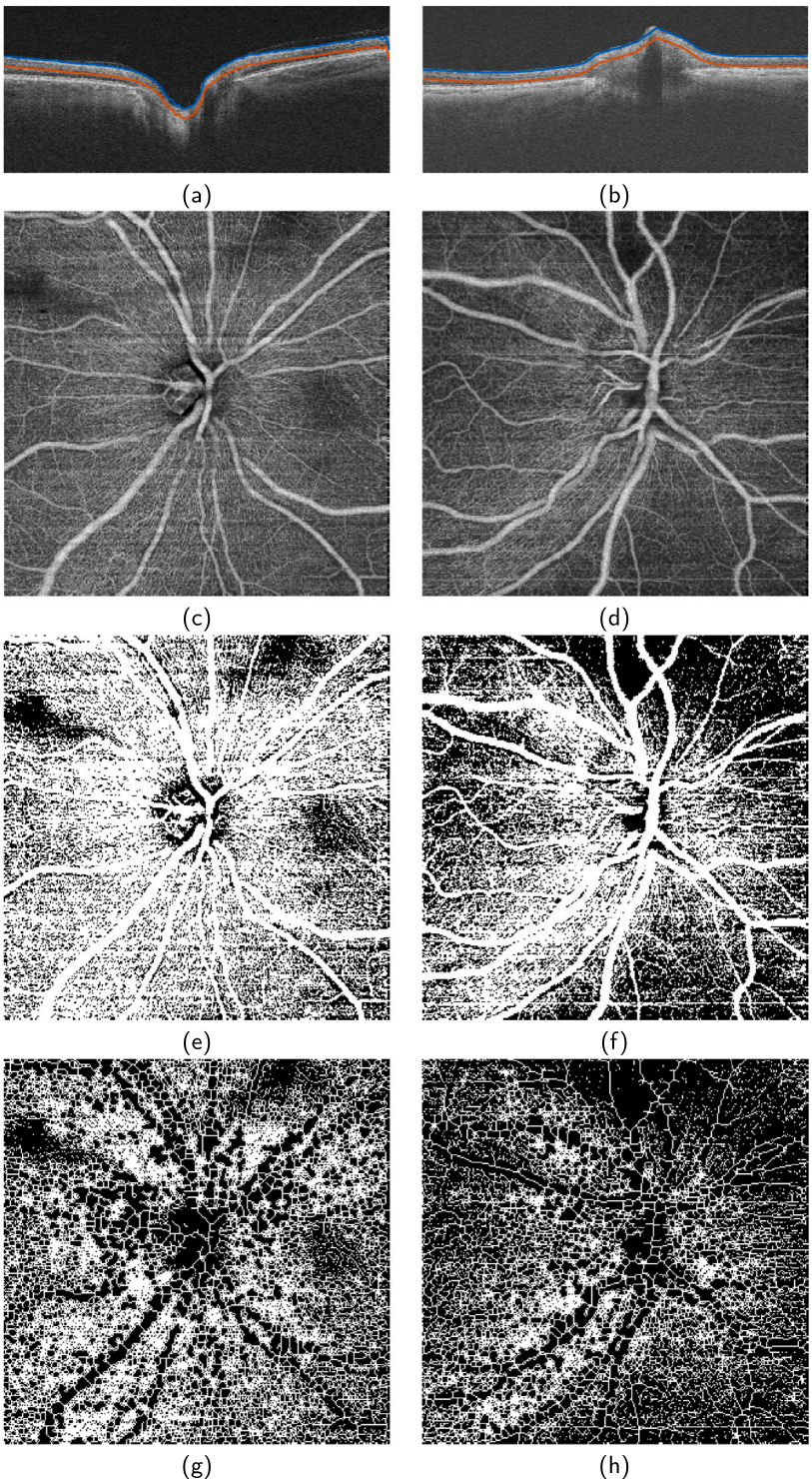

Fig. 5. Generation of en face angiogram for a healthy person (left column) and an ODD patient (right column). First row (a) and (b) shows that the slab in which the vessels are found is limited by the inner limiting membrane (ILM) (blue line) anteriorly. The posterior limit of the slab is set at a level of 150 μm in depth from the ILM (red line). Second row (c) and (d) shows the en face angiogram within the slab. Third row (e) and (f) shows the binary images of segmented vessel structures using an adaptive threshold segmentation algorithm. Last row (g) and (h) shows the skeletonization of vessel structures. (For interpretation of the references to colour in this figure legend, the reader is referred to the web version of this article.)

of the influence of ODD size and location on the peripapillary vessel density.

3.5.1. ODD Location, area and volume

We determine the size and location of the manually segmented ODD as described in Malmqvist et al. (2017). The peripapillary vessel density is expressed in the 2D plane in the sections of the Garway-Heath map on the heatmap generated from the en face angiogram. To combine this information with the ODD location, area and volume, we express these three parameters in the same 2D plane. Fig. 4 shows how the ODD information is transmitted from the 3D-space, where it was segmented, into the 2D plane. The location of the ODD is represented

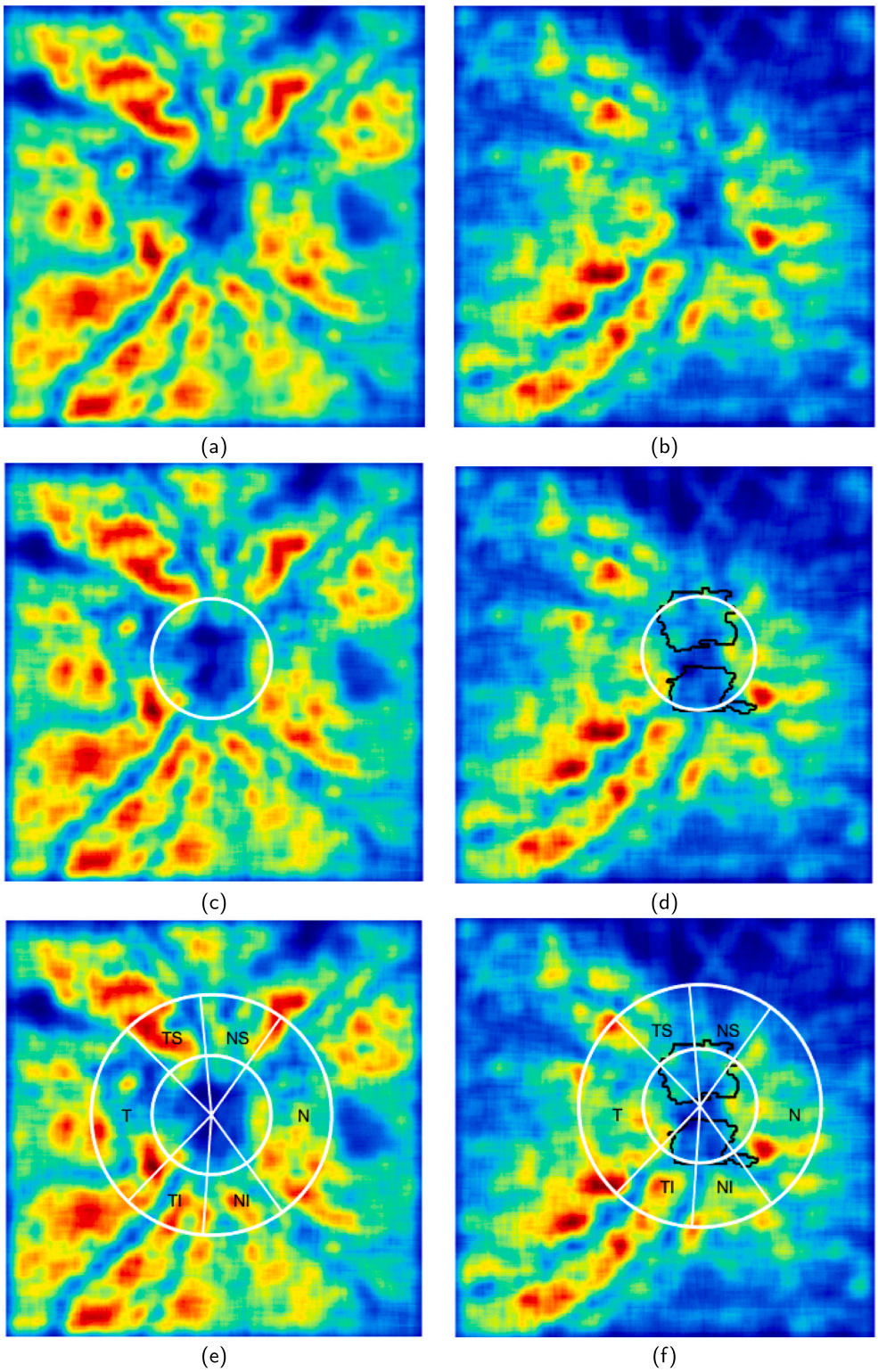

Fig. 6. Vessel density heatmaps for a healthy person (left column) and an ODD patient (right column). First row (a) and (b) shows the vessel density heatmaps computed from the segmented vessel images. Second row (c) and (d) shows the same heatmaps as (a) and (b) with the circle fitted to the optic disc and the ODD outline for the ODD patient. Last row (e) and (f) shows the heatmaps with the Garway-Heath map on and labels for the six sections.

by the outer boundary of each ODD as shown in Fig. 4a, the ODD area is the area inside the boundary as shown in Fig. 4b and the ODD volume is expressed as a 2D height map by summing up ODD voxels in depth as illustrated in Fig. 4c.

The ODD are located in the ONH, and since we want to describe the impact of their location on the peripapillary vessel density in each section of the Garway-Heath map, we expand the section from the Garway-Heath map into the inner circle of the map; the ONH. We

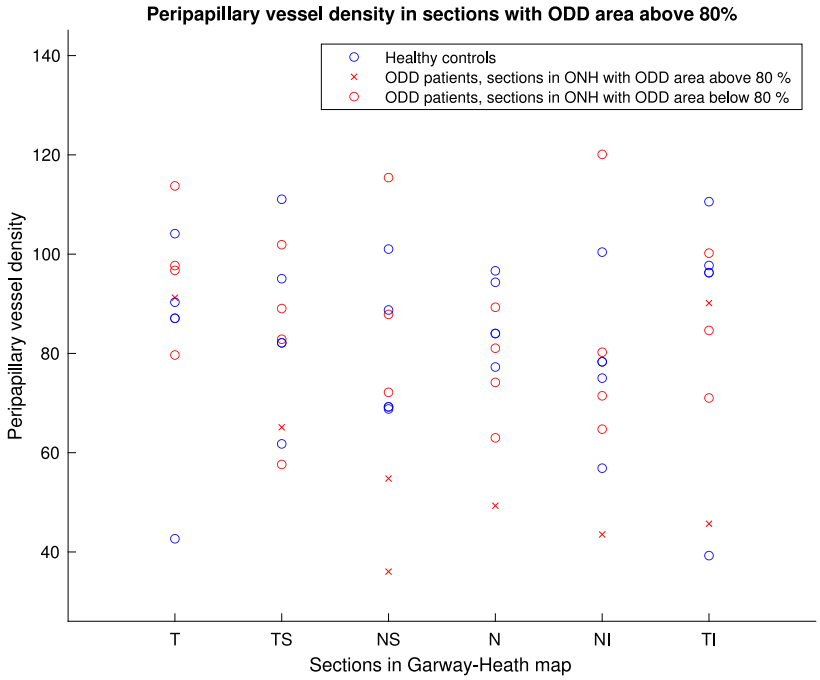

Fig. 7. The peripapillary vessel density within the six sections of the Garway-Heath map. For healthy controls the peripapillary vessel densities for all sections are marked with blue circles. For ODD patients the peripapillary vessel densities in sections with ODD area above 80% in the corresponding section in ONH are marked with red crosses, while peripapillary vessel densities in sections with ODD area below 80% in the corresponding section in ONH are marked with red circles. (For interpretation of the references to colour in this figure legend, the reader is referred to the web version of this article.)

calculate how much of the total area each ODD covers in each section as a percentage and the total ODD volume in each section.

3.5.2. Peripapillary vessel density within sections

We compute the peripapillary vessel density within the six sections of the Garway-Heath map by summing the pixels in each section in the vessel density heatmap and dividing by the area of the section. The area of the section is determined by the diameter of the inner circle and varies with the size of the optic disc, while the diameter of the outer circle of the Garway-Heath map is fixed to 3.46 mm by definition.

4. Results

First, we present illustrations of the method applied for a healthy control and an ODD patient to show the applicability of the method for different data types and moreover to illustrate the differences between the two groups. Second, we present the peripapillary vessel densities calculated for a small data set as a quantification of the method.

4.1. En face angiogram and segmented vessels

The en face angiogram is generated from the angiographic data in the slab. Fig. 5 shows the steps from detection of the slab to the segmented skeletonized vessels. The left column contains the results for a healthy control and the right column for an ODD patient. In Fig. 5a and b, the detected slabs are shown on a randomly chosen structural B-scan. The detected ILM is marked with blue and the 150 μm layer under is marked with red. The en face angiograms are shown in Fig. 5c and d and the binary image containing the segmented vessels are shown in Fig. 5e and f. The skeletonized vessels are shown in Fig. 5g and h.

4.2. Vessel density heatmaps

The vessel density heatmap illustrates the vessel density in colours; red colour indicating high vessel density and blue colour indicating low vessel density. In Fig. 6a and b we present vessel density heatmaps for the same healthy person (left column) and the same ODD patient (right column) as used in Fig. 5. For illustration of the optic disc and its size, we present the same heatmaps in Fig. 6c and d with the circle (white) fitted to the optic disc. Moreover, for the ODD patient, the outline of the segmented ODDs is marked with black. Finally, in Fig. 5e and f, we present the vessel density heatmap with the Garway-Heath map on top showing the six sections (white) and for the ODD patient the outline of the ODD (black).

4.3. Peripapillary vessel density and other quantitative data

In Table 1 we present the peripapillary vessel density within each section of the Garway-Heath map for the five ODD patients and the five healthy controls. Furthermore, we present the amount of ODD area (%) and the ODD volume inside the ONH in each of the six sections.

We investigate the influence of the ODD area and volume on the peripapillary vessel density. We want to look at sections where the ODD area is large to see if it has an impact on the peripapillary vessel density. We choose a cut-off value to divide the ODD patients into two groups, one with none or small ODD area and one with large ODD area. The cut-off value is chosen to be ODD area that covers more than 80% of the section area, dividing the ODD patients into two groups, one with ODD area below 80% and one with ODD area above 80% of the section area. Fig. 7 shows the peripapillary vessel density for healthy controls and ODD patients within the six sections of the Garway-Heath map.

On Fig. 8 the correlation between the peripapillary vessel density and the ODD area or volume is shown. Fig. 8a shows the correlation between the ODD area and the peripapillary vessel density in the six sections for the five ODD patients. Fig. 8b shows the correlation between the ODD volume and the peripapillary vessel density in the same way as Fig. 8a.

5. Discussion and conclusion

We presented a method for determining the peripapillary vessel density in the six sections of the Garway-Heath map. The method is

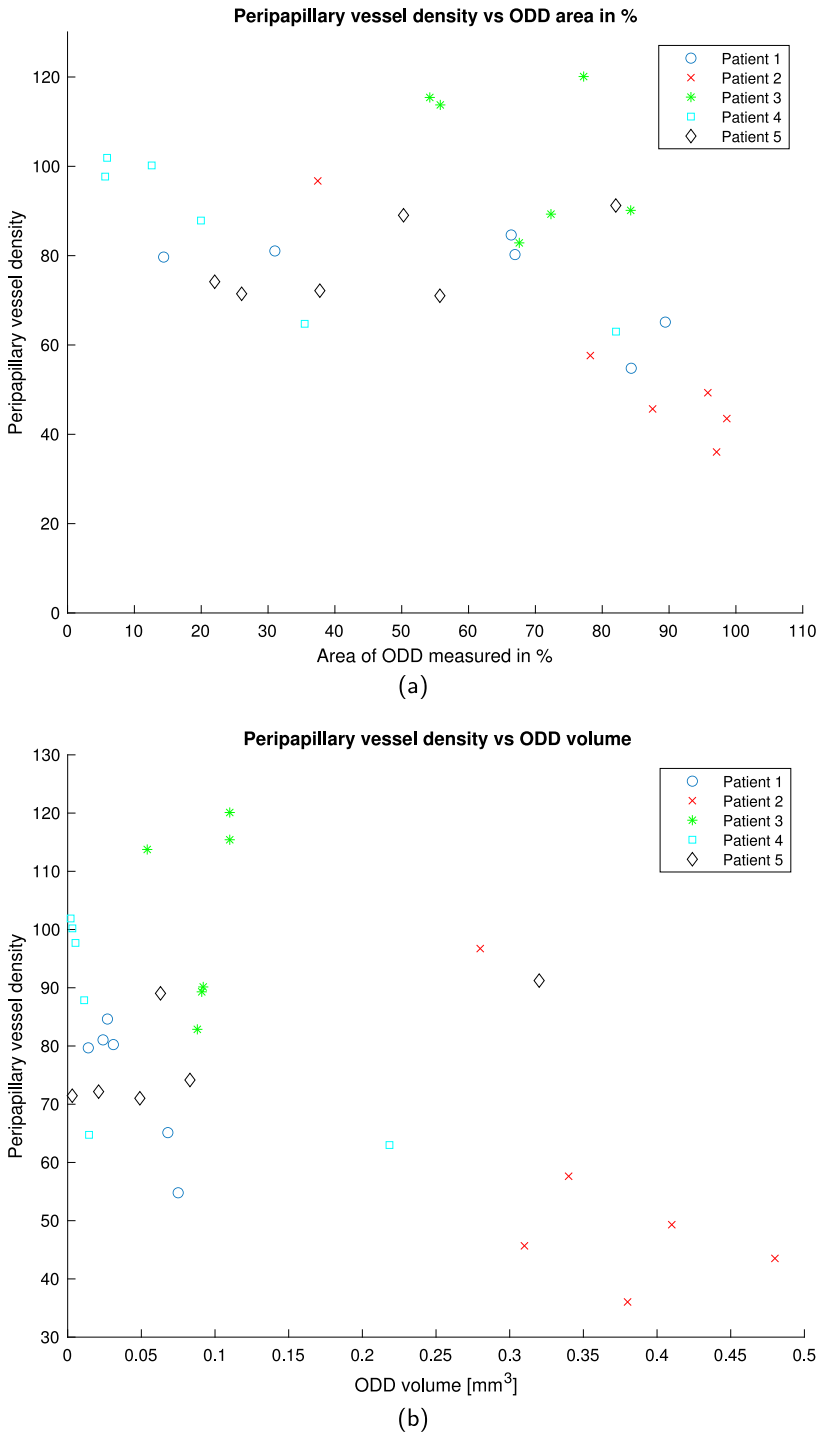

Fig. 8. Correlation between peripapillary vessel density and (a) ODD area or (b) ODD volume. Each of the five ODD patients has six data points, one for each section in the Garway-Heath map.

applicable to different data, here applied on OCTA from healthy controls and ODD patients. We wanted to develop a method that produces comparable results. Furthermore, compared to built-in software, our method describes each step in the determination of peripapillary vessel density, and each step can easily be adjusted or improved to help determine vessel density in general.

We chose to express the peripapillary vessel density using skeletonization to disregard the thickness of vessels. This results in equal weighting of the large radial peripapillary vessels and the smaller capillaries in the vessel density map. Most built-in software seems to express the vessel density in terms of the vessel area (Zhang et al., 2019). We believe that the vessel density map is most illustrative and usable when using the skeletonization. If skeletonization is not used, the large variations in vessel thickness result in a heatmap with many high density areas (hot spots) at locations where a thick vessel is located.

Quantification of the method in a small study with sample size of ten participants showed a clear tendency for lower vessel density in sections with a large ODD area or volume. The peripapillary vessel density for sections with ODD area covering more than 80% of the section area in the ONH was in general lower than the peripapillary vessel density for sections with ODD area below 80% of section area in ONH. The sample size of the study is of course notable and results

Table 1
Peripapillary vessel density for five ODD patients and five healthy controls within the six sections of the Garway-Heath map. The ODD area is measured as a percentage of the total area in the corresponding ONH section. The ODD volume is also measured in the corresponding ONH section.

	T	TS	NS	N	NI	TI
Patient 1						
Peripapillary vessel density	79.68	65.12	54.79	81.05	80.24	84.63
ODD area	14.38	89.44	84.34	31.02	66.95	66.38
ODD volume [mm^3]	0.014	0.068	0.075	0.024	0.031	0.027
Patient 2						
Peripapillary vessel density	96.73	57.63	36.04	49.31	43.52	45.68
ODD area	37.44	78.22	97.11	95.80	98.64	87.54
ODD volume [mm^3]	0.28	0.34	0.38	0.41	0.48	0.31
Patient 3						
Peripapillary vessel density	113.75	82.86	115.42	89.30	120.10	90.14
ODD area	55.77	67.59	54.20	72.33	77.22	84.26
ODD volume [mm^3]	0.054	0.088	0.11	0.091	0.11	0.092
Patient 4						
Peripapillary vessel density	97.7	101.9	87.86	62.99	64.74	100.2
ODD area	5.63	5.92	19.96	82.06	35.48	12.59
ODD volume [mm^3]	0.0053	0.0020	0.0112	0.2184	0.0145	0.0032
Patient 5						
Peripapillary vessel density	91.23	89.04	72.16	74.16	71.46	71.02
ODD area	82.03	50.27	37.75	22.02	26.05	55.71
ODD volume [mm^3]	0.32	0.063	0.021	0.083	0.0031	0.049
Healthy control 1						
Peripapillary vessel density	42.66	61.77	68.81	77.26	56.88	39.26
Healthy control 2						
Peripapillary vessel density	87.08	82.13	69.23	84.01	78.31	96.27
Healthy control 3						
Peripapillary vessel density	90.32	111.06	88.75	96.64	100.41	110.57
Healthy control 4						
Peripapillary vessel density	104.13	95.05	101.02	94.33	75.02	97.71
Healthy control 5						
Peripapillary vessel density	87.08	82.13	69.23	84.01	78.31	96.27

should be treated with care. A larger study for quantification of statistically significant differences between the groups needs to be carried out before any conclusions can be made.

Besides the applicability of the method, the study also shows that results obtained from OCTA can be combined with information from OCT. Combining information from the two scan types could be helpful in the investigation of different diseases when there is a requirement to combine the vessel density with any information visible on OCT. The recent study by Engelke et al. (2019) investigates the peripapillary vessel density in nasal, inferior and superior sections, where most ODD occur, but combining the vessel density with the actual location of the ODD from OCT would have revealed even more insight into the impact of ODD on the vessel density.

Studies by Venugopal et al. (2018) and Al-Sheikh et al. (2017) address the problem about repeatability of the vessel density and influence of Signal Strength Index (SSI) on the vessel density. The SSI might affect the en face angiogram and the appearance of the vessels and noise. This should be further investigated and since the quality of OCTA improves rapidly, high density scans could help investigate this issue. To address the issue, we only included OCTA scans with SSI above 50.

It is our hope and believe that the method will contribute to the quantification of OCTA data and in the research of the influence of local anatomic ONH conditions such as ODD on the peripapillary vessel density.

Fundings and conflict of interest

This research did not receive any specific grant from funding agencies in the public, commercial, or not-for-profit sectors. None of the authors has any conflict of interest to declare.

References

Aghdam, K.A., Khorasani, M.A., Sanjari, M.S., Habibi, A., Shenazandi, H., Kazemi, P., Falavarjani, K.G., 2018. Optical coherence tomography angiography features of optic nerve head drusen and nonarteritic anterior ischemic optic neuropathy. Canad. Ophthalmol. Soc. 54 (4).

Akil, H., Huang, A.S., Francis, B.A., Sadda, S.R., Chopra, V., 2017. Retinal vessel density from optical coherence tomography angiography to differentiate early glaucoma, pre-perimetric glaucoma and normal eyes. PLoS One.

Al-Sheikh, M., Tepelus, T.C., Nazikyan, T., Sadda, S.R., 2017. Repeatability of automated vessel density measurements using optical coherence tomography angiography. Br. J. Ophthalmol.

Bradley, D., Roth, G., 2007. Adaptive thresholding using the integral image. J. Graph. Tools.

Cennamo, G., Tebaldi, S., Amoroso, F., Arvanitis, D., Breve, M., Cennamo, G., 2017. Optical coherence tomography angiography in optic nerve drusen. Ophthalmic Res.

Chalam, K., Sambhav, K., 2016. Optical coherence tomography angiography in retinal diseases. J. Ophthalmic Vis. Res.

Engelke, H., Shajari, M., Riedel, J., Mohr, N., Priglinger, S.G., Mackert, M.J., 2019. OCT angiography in optic disc drusen: comparison with structural and functional parameters. Br. J. Ophthalmol.

Gaier, E.D., III, J.F.R., Miller, J.B., Cestari, D.M., 2017. Focal capillary dropout associated with optic disc drusen using optical coherence tomographic angiography. Neuro Ophthalmol.

Garvin, M.K., Abramoff, M.D., Wu, X., Russell, S.R., Burns, T.L., Sonka, M., 2009. Automated 3-d intraretinal layer segmentation of macular spectral-domain optical coherence tomography images. Trans. Med. Imaging.

Garway-Heath, D.F., Poinoosawmy, D., Fitzke, F.W., Hitchings, R.A., 2000. Mapping the visual field to the optic disc in normal tension glaucoma eyes. Ophthalmology 107 (10).

Hagag, A.M., Gao, S.S., Yali, J., Huang, D., 2017. Optical coherence tomography angiography: Technical principles and clinical applications in ophthalmology. Taiwan J. Ophthalmol.

Hata, M., Oishi, A., Muraoka, Y., Miyamoto, K., Kawai, K., Yokota, S., Fujimoto, M., Miyata, M., Yoshimura, N., 2017. Structural and functional analyses in nonarteritic anterior ischemic optic neuropathy: Optical coherence tomography angiography study. Neuro Ophthalmol.

Iafe, N.A., Phasukkijwatana, N., Chen, X., Sarraf, D., 2016. Retinal capillary density and foveal avascular zone area are age-dependent: Quantitative analysis using optical coherence tomography angiography. Invest. Ophthalmol. Vis. Sci.

Lindberg, A.-S.W., Conradsen, K., Larsen, R., Lippert, M.F., Røge, R., Vyberg, M., 2017. Quantitative tumor heterogeneity assessment on a nuclear population basis. Cytometry A.

Liu, L., Jia, Y., Takusagawa, H.L., Pechauer, A.D., Edmunds, B., Lombardi, L., Davis, E., Morrison, J.C., Huang, D., 2015. Optical coherence tomography angiography of the peripapillary retina in glaucoma. JAMA Ophthalmol.

Malmqvist, L., Lindberg, A.-S.W., Dahl, V.A., Jørgensen, T.M., Hamann, S., 2017. Quantitatively measured anatomic location and volume of optic disc drusen: An enhanced depth imaging optical coherence tomography study. Invest. Ophthalmol. Vis. Sci. 58 (5).

Moussa, M., Leila, M., Khalid, H., 2017. Imaging choroidal neovascular membrane using en face swept-source optical coherence tomography angiography. Clin. Ophthalmol.

Venugopal, J.P., Rao, H.L., Weinreb, R.N., Dasari, S., Riyazuddin, M., Pradhan, Z.S., Puttaiah, N.K., Devi, S., Mansouri, K., Webers, C.A.B., 2018. Repeatability and comparability of peripapillary vessel density measurements of high-density and non-high-density optical coherence tomography angiography scans in normal and glaucoma eyes. Br. J. Ophthalmol.

Wang, L., Murphy, O., Caldito, N.G., Calabresi, P.A., Saidha, S., 2018. Emerging applications of optical coherence tomography angiography (OCTA) in neurological research. Eye Vis.

Yarmohammadi, A., Zangwill, L.M., Diniz-Filho, A., Suh, M.H., Manalastas, P.I., Fatehee, N., Yousefi, S., Belghith, A., Saunders, L.J., Medeiros, F.A., Huang, D., Weinreb, R.N., 2017. Optical coherence tomography angiography vessel density in healthy, glaucoma suspect, and glaucoma eyes. Invest. Ophthalmol. Vis. Sci. 57 (9).

Yarmohammadi, A., Zangwill, L.M., Diniz-Filho, A., Suh, M.H., Yousefi, S., Saunders, L.J., Belghith, A., Manalastas, P.I., Medeiros, F.A., Weinreb, R.N., 2016. Relationship between optical coherence tomography angiography vessel density and severity of visual field loss in glaucoma. Ophthalmology.

Yushkevich, P.A., Piven, J., Cody Hazlett, H., Gimpel Smith, R., Ho, S., Gee, J.C., Gerig, G., 2006. User-guided 3D active contour segmentation of anatomical structures: Significantly improved efficiency and reliability. Neuroimage 31 (3), 1116–1128.

Zhang, T., Xiao, W., Ye, H., Chen, R., Mao, Y., Yang, H., 2019. Peripapillary and macular vessel density in dysthyroid optic neuropathy: An optical coherence tomography angiography study. Invest. Ophthalmol. Vis. Sci.

Bibliography

[1] R. R. Seeley, T. D. Stephens, and P. Tate, *Anatomy Physiology*. McGraw-Hill, 8 ed., 2008.

[2] F. Willermain, S. Libert, E. Motulsky, D. Salik, L. Caspers, J. Perret, and C. Delporte, "Origins and consequences of hyperosmolar stress in retinal pigmented epithelial cells," *Frontiers in Physiology*, 2014.

[3] R. S. Ramrattan, R. C. W. Wolfs, J. B. Jonas, A. Hofman, and P. T. V. M. de Jong, "Determinants of optic disc characteristics in a general population - the rotterdam study," *Ophthalmology*, vol. 106, no. 8, pp. 1588–1596, 1999.

[4] H. Müller, "Anatomische beitrage zur ophthalmologie," *Albrecht von Graefes Arch Klin Ophthalmologie*, vol. 4, pp. 1–40, 1858.

[5] S. Lorentzen, *Drusen of the optic disk. A clinical and generit study*, vol. 90. Acta Ophthalmologica, 1966.

[6] A. H. Friedman, S. Gartner, and S. S. Modi, "Drusen of the optic disc. a retrospective study in cadaver eyes," *British Journal of Ophthalmology*, vol. 59, no. 8, pp. 413–421, 1975.

[7] A. G. Lee and M. B. Zimmerman, "The rate of visual field loss in optic nerve head drusen," *American journal of ophthalmology*, vol. 139, no. 6, pp. 1062–1066, 2005.

[8] H. P. Petersen, "Colloid bodies with defects in the field of vision," *Acta Ophthalmologica*, vol. 35, no. 243-272, 1957.

[9] J. M. Wilkins and H. D. Pomeranz, "Visual manifestations of visible and buried optic disc drusen," *Journal of Neuroophthalmology*, vol. 24, no. 2, pp. 125–129, 2004.

[10] A. Casado, G. Rebolleda, L. Guerrero, M. Leal, I. Contreras, N. Oblanca, and F. J. Muñoz-Negrete, "Measurement of retinal nerve fiber layer and macular ganglion cell-inner plexiform layer with spectral-domain optical coherence tomography in patients with optic nerve head drusen," *Graefes Arch Clin Exp Ophthalmology*, vol. 252, no. 10, pp. 1653–1660, 2014.

[11] A. E. Krill, B. A. Klien, and D. B. Archer, "Precursors of angioid streaks," *American journal of ophthalmology*, vol. 76, no. 6, 1973.

[12] L. Malmqvist, A. Kyhnel, and S. Hamann, "Substantial visual field loss associated with giant optic disc drusen," *Jama ophthalmology*, vol. 135, no. 12, 2017.

[13] M. A. Khan and A. R. Forman, "Legal blindness from severe optic nerve head drusen," *Jama ophthalmology*, vol. 134, no. 2, 2016.

[14] B. Tuğcu and H. Özdemir, "Imaging methods in the diagnosis of optic disc drusen," *Turkish Journal of Ophthalmology*, vol. 46, pp. 232–236, 2016.

[15] J. B. Jonas, G. C. Gusek, I. Guggenmoos-Holzmann, and G. O. H. Naumann, "Optic nerve head drusen associated with abnormally small optic discs," *International Ophthalmology*, vol. 11, pp. 79–82, 1987.

[16] S. Aumann, S. Donner, J. Fischer, and F. Müller, *High Resolution Imaging in Microscopy and Ophthalmology*, ch. 3, pp. 59–85. Springer, 2019.

[17] P. Serranho, A. M. Morgado, and R. Bernardes, *Optical Coherence Tomography - A Clinical and Technical Update*, ch. 7, pp. 139–156. Springer, 2012.

[18] R. F. Spaide, H. Koizumi, and M. C. Pozonni, "Enhanced depth imaging spectral-domain optical coherence tomography," *American journal of ophthalmology*, 2008.

[19] I. Y. Wong, "Enhanced depth imaging spectral-domain optical coherence tomography," *Ophthalmic surgery, lasers and imaging*, vol. 42, no. 4, 2011.

[20] E. V. Poorten, C. N. Riviere, and I. Iordachita, *Handbook of Robotic and Image-Guided Surgery*, ch. 36. Elsevier, 2020.

[21] A. M. Hagag, S. S. Gao, Y. Jia, and D. Huang, "Optical coherence tomography angiography: Technical principles and clinical applications in ophthalmology," *Taiwan Journal of Ophthalmology*, vol. 7, no. 3, pp. 115–129, 2017.

[22] R. F. Spaide, J. G. Fujimoto, and N. K. Waheed, "Image artifacts in optical coherence angiography," *Retina*, vol. 35, no. 11, pp. 2163–2180, 2015.

[23] R. F. Spaide, J. M. Klancnik, and M. J. Cooney, "Retinal vascular layers imaged by fluorescein angiography and optical coherence tomography angiography," *Jama ophthalmology*, vol. 133, no. 1, pp. 45–50, 2015.

[24] L. A. Pinto, E. Vandewalle, C. Marques-Neves, and I. Stalmans, "Visual field loss in optic disc drusen patients correlates with central retinal artery blood velocity patterns," *Acta Ophthalmologica*, vol. 92, pp. 286–291, 2014.

[25] K. Yi, M. Mujat, W. Sun, D. Burnes, M. A. Latina, D. T. Lin, D. G. Deschler, P. A. D. Rubin, B. H. Park, J. F. de Boer, and T. C. Chen, "Imaging of optic nerve head drusen: improvements with spectral domain optical coherence tomography," *Journal of Glaucoma*, vol. 18, no. 5, pp. 373–378, 2009.

[26] P. A. Yushkevich, J. Piven, H. C. Hazlett, R. G. Smith, S. Ho, J. C. Gee, and G. Gerig, "User-guided 3d active contour segmentation of anatomical structures: Significantly improved effiency and reliability," *Neuroimage*, vol. 31, no. 3, pp. 1116–1128, 2006.

[27] K. Y. Merchant, D. Su, S. S. Park, S. Qayum, R. Banik, J. M. Liebmann, and R. Ritch, "Enhanced depth imaging optical coherence tomography of optic nerve head drusen," *Ophthalmology*, vol. 120, no. 7, pp. 1409–1414, 2013.

[28] T. Sato, S. Mrejen, and R. F. Spaide, "Multimodal imaging of optic disc drusen," *American journal of ophthalmology*, vol. 156, no. 275-282, 2013.

[29] M. P. Ghassibi, J. L. Chien, R. K. Abumasmah, J. M. Liebmann, R. Ritch, and S. C. Park, "Optic nerve head drusen prevalence and associated factors in clinically normal subjects measured using optical coherence tomography," *Ophthalmology*, vol. 124, no. 320-325, 2017.

[30] S. Slotnick and J. Sherman, "Buried disc drusen have hypo-reflective appearance on sd-oct," *Optometry and vision science*, vol. 89, no. 5, pp. 704–708, 2012.

[31] L. Malmqvist, L. Bursztyn, F. Costello, K. Digre, J. A. Fraser, C. Fraser, B. Katz, M. Lawlor, A. Petzold, P. Sibony, J. Warner, M. Wegener, S. Wong, and S. Hamann, "The optic disc drusen studies consortium recommendations for diagnosis of optic disc drusen using optical coherence tomography," *2017*, vol. 38, no. 3, Journal of Neuro-Ophthalmology.

[32] L. Malmqvist, M. Wegener, B. Sander, and S. Hamann, "Peripapillary retinal nerve fiber layer thickness corresponds to drusen location and extent of visual field defects in superficial and burried optic disc drusen," *Journal of Neuroophthalmology*, vol. 36, no. 1, pp. 41–45, 2016.

[33] P. Freund and E. Margolin, *Pseudopapilledema*. StatsPearls, 2020.

[34] T. S. Spencer, B. Katz, S. W. Weber, and K. Digre, "Progression from anomalous optic discs to visible optic disc drusen," *Journal of Neuroophthalmology*, vol. 24, no. 4, pp. 297–298, 2004.

[35] K. M. Lee, S. J. Woo, and J.-M. Hwang, "Morphologic characteristics of optic nerve head drusen on spectral-domain optical coherence tomography," *American journal of ophthalmology*, vol. 155, no. 6, pp. 1139–1147, 2013.

[36]

[37] M. Haeker, X. Wu, M. Abrámoff, R. Kardon, and M. Sonka, "Incorporation of regional information in optimal 3-d graph search with application for intraretinal layer segmentation of optical coherence tomography images," *Information Processing in Medical Imaging*, pp. 607–618, 2007.

[38] M. K. Garvin, M. D. Abramoff, R. Kardon, S. R. Russell, X. Wu, and M. Sonka, "Intraretinal layer segmentation of macular optical coherence tomography images using optimal 3-d graph search," *Transactions on Medical Imaging*, 2008.

[39] M. K. Garvin, M. D. Abramoff, X. Wu, S. R. Russell, T. L. Burns, and M. Sonka, "Automated 3-d intraretinal layer segmentation of macular spectral-domain optical coherence tomography images," *Transactions on Medical Imaging*, 2009.

[40] X. Wu and D. Z. Chen, *Optimal Net Surface Problems with Applications*, pp. 1029–1042. Springer, 2002.

[41] M.-M. Sung, H.-J. Kim, E.-K. Kim, J.-Y. Kwak, J.-K. Yoo, and H.-S. Yoo, "Clinical evaluation of jpeg2000 compression for digital mammography," *Nuclear Science*, vol. 49, no. 3, 2002.

[42] V. Loia and S. Sessa, "Fuzzy relation equations for coding/decoding processes of images and videos," *Information Sciences*, vol. 171, no. 1-3, 2005.

[43] A. Yarmohammadi, L. M. Zangwill, A. Diniz-Filho, M. H. Suh, S. Yousefi, L. J. Saunders, A. Belghith, P. I. Manalastas, F. A. Medeiros, and R. N. Weinreb, "Relationship between optical coherence tomography angiography vessel density and severity of visual field loss in glaucoma," *Ophthalmology*, 2016.

[44] T. Zhang, W. Xiao, H. Ye, R. Chen, Y. Mao, and H. Yang, "Peripapillary and macular vessel density in dysthyroid optic neuropathy: An optical coherence tomography angiography study," *Investigative Ophthalmology & Visual Science*, 2019.

[45] A. Yarmohammadi, L. M. Zangwill, A. Diniz-Filho, M. H. Suh, P. I. Manalastas, N. Fatehee, S. Yousefi, A. Belghith, L. J. Saunders, F. A. Medeiros, D. Huang, and R. N. Weinreb, "Optical coherence tomography angiography vessel density in healthy, glaucoma suspect, and glaucoma eyes," *Investigative Ophthalmology & Visual Science*, vol. 57, no. 9, 2017.

[46] D. Bradley and G. Roth, "Adaptive thresholding using the integral image," *Journal of Graphics Tools*, 2007.

[47] N. A. Iafe, N. Phasukkijwatana, X. Chen, and D. Sarraf, "Retinal capillary density and foveal avascular zone area are age-dependent: Quantitative analysis using optical coherence tomography angiography," *Investigative Ophthalmology & Visual Science*, 2016.

[48] A.-S. W. Lindberg, K. Conradsen, and R. Larsen, "Quantitative tumor heterogeneity assessment on a nuclear population basis," *Cytometry, part A*, vol. 91, no. 6, pp. 574–584, 2016.

[49] D. F. Garway-Heath, D. Poinoosawmy, F. W. Fitzke, and R. A. Hitchings, "Mapping the visual field to the optic disc in normal tension glaucoma eyes," *Ophthalmology*, vol. 107, no. 10, 2000.